

## ABSTRACT

O'SHAUGHNESSY, CHRISTOPHER M. Development of a Precision Neutron Lifetime Measurement: Magnetic Trapping of Ultracold Neutrons. (Under the direction of Professor P. R. Huffman).

The neutron lifetime plays an important role in both nuclear astrophysics and in furthering the understanding of weak interactions in the Standard Model. It is the most important experimental parameter in theoretical predictions of the primordial abundance of  $^4\text{He}$  in Big Bang Nucleosynthesis. A precision measurement also provides a self consistency check of the unitarity of the CKM mixing matrix which relates the weak and mass eigenstates of quarks in the Standard Model. Our group has successfully demonstrated the trapping of ultracold neutrons in a conservative potential magnetic trap and demonstrated that the measured lifetime was consistent with the present world average value. This work represents a major upgrade of the apparatus assembled at the NIST Center for Neutron Research to address statistical limitations of the former measurement. Our unique approach to this measurement and the advantages it provides over other techniques will be discussed. The major systematics of the technique will be addressed. Tests of the upgrade components and details of the final stages of construction will also be presented.

Development of a Precision Neutron Lifetime Measurement:  
Magnetic Trapping of Ultracold Neutrons

by  
Christopher Martin O'Shaughnessy

A dissertation submitted to the Graduate Faculty of  
North Carolina State University  
in partial fulfillment of the  
requirements for the Degree of  
Doctor of Philosophy

Physics

Raleigh, North Carolina

2010

APPROVED BY:

---

Dr. David G. Haase

---

Dr. Gail C. McLaughlin

---

Dr. Paul R. Huffman  
Chair of Advisory Committee

---

Dr. Chris R. Gould

# Biography

Christopher M. O'Shaughnessy was born in upstate NY to two cool and loving parents somewhere between 1978 and 1985. He has one older brother who knits amazingly well. Early in life, Chris gained notoriety for [REDACTED] pink striped pajamas [REDACTED] house cat [REDACTED]. For grad school he chose to study fundamental neutron physics because he heard the field had a large women/men ratio. This bore fruit when he met and later married (weeks before graduating which is why a completely random person is writing his bio) his wife [REDACTED] [REDACTED] Dave. [REDACTED] In 2009 he was the sole recipient of the prestigious Golden Possum Award for his contributions in neutron science. It should be noted that although Chris has many noble qualities (Ex. My mom thinks that he has great hair.), he is not and will never be, as awesome as Dima.

# Acknowledgements

I would like to thank Paul Huffman for the outstanding support he has offered me when I needed it most and for the freedom he has given me in those times when his support was not necessary. My experience would not have been as valuable without the assortment of opportunities that Paul has made available to me.

Without the passion for physics from individuals such as Albert Young and Robby Pattie, I do not think my excitement for physics would have persisted as long as it has. The long hours and hard labor of a work often obscure the reasons for completing it. For reminding me so vividly of the global picture I am indebted to them.

Thank you also to my committee members, Professors Gould, Haase, and McLaughlin for sharing your time and experience with me.

I am grateful to Pieter Mumm for sharing with me both his technical experience and his friendship. Without the groundwork layed out by Liang Yang, I would have made very little progress. His hardly questionable advice, good safety record, and impressive crossword skills were a standard to live up to. For the the always witful life advice from Jeffrey Nico I am also indebted.

I must also acknowledge my NCSU officemates Adam Holley, Grant Palmquist, Robby Pattie, Peter Gilbert, Keith Heyward, and Liping Yu; without whose furniture rearrangements I wouldn't quite have the right perspective for a career in physics. I would also like to thank Karl Schelhammer, Michael Huber, Patrick Hughes, Nathan Meyer, Dmitry Lyapustin, Craig Huffer, Courtney Taylor and Daniel Marley for all of their contributions to this work.

Last, but not least, thanks to Michael Huber for the flattering biography he has written for me.

# Table of Contents

<b>List of Figures</b> . . . . .	vi
<b>List of Tables</b> . . . . .	viii
<b>Chapter 1 Introduction</b> . . . . .	1
1.1 Chronology of Nuclear Physics . . . . .	2
1.2 Weak Interactions in the Standard Model . . . . .	5
1.2.1 Yang-Mills Theory . . . . .	9
1.2.2 Glashow-Weinberg-Salam Theory of Weak Interactions . . . . .	11
1.3 Beta Decay . . . . .	17
1.4 Big Bang Nucleosynthesis . . . . .	22
1.4.1 Primordial Nucleosynthesis . . . . .	24
1.4.2 Nuclear Statistical Equilibrium . . . . .	25
1.4.3 Limiting the Standard Model . . . . .	28
1.5 Summary . . . . .	29
<b>Chapter 2 Neutron Lifetime Measurement Techniques</b> . . . . .	30
2.1 Neutron Sources . . . . .	30
2.2 Properties of Ultracold Neutrons . . . . .	32
2.3 Neutron Beta-Decay . . . . .	32
2.3.1 Beam-type Neutron Lifetime Measurements . . . . .	36
2.3.2 Bottle-type Neutron Lifetime Measurements . . . . .	38
2.3.3 Neutron Lifetime Measurements Using Magnetic Confinement . . . . .	39
2.4 Experimental Method . . . . .	43
<b>Chapter 3 Apparatus</b> . . . . .	46
3.1 Facility . . . . .	46
3.1.1 Superthermal Production of UCN . . . . .	47
3.1.2 0.89 nm Monochromatic Beam . . . . .	48

3.2	Magnetic Trap . . . . .	50
3.2.1	Quench Protection . . . . .	53
3.2.2	Magnetic Field Compensation . . . . .	56
3.3	Cryostat . . . . .	58
3.3.1	Neutron Entrance . . . . .	66
3.3.2	Experimental Cell . . . . .	67
3.3.3	Light Collection System . . . . .	74
3.4	Experimental Procedure . . . . .	93
3.5	Data Acquisition System . . . . .	95
3.5.1	Data Collection . . . . .	95
3.5.2	Control Functions . . . . .	97
3.6	Apparatus Performance . . . . .	99
3.6.1	Cryogenics . . . . .	101
3.6.2	Magnets . . . . .	102
3.6.3	Shielding . . . . .	103
3.6.4	Background Studies . . . . .	104
<b>Chapter 4 Systematic Studies . . . . .</b>		<b>108</b>
4.1	$^3\text{He}$ Contamination in the Isotopically Pure $^4\text{He}$ . . . . .	108
4.2	Above Threshold Neutrons . . . . .	111
4.2.1	Simulations of Above Threshold Neutrons . . . . .	112
4.3	Gain Stability of the Detectors . . . . .	127
<b>Chapter 5 Conclusions . . . . .</b>		<b>129</b>
<b>Bibliography . . . . .</b>		<b>132</b>
<b>Appendix . . . . .</b>		<b>142</b>
<b>A GuideIt Input . . . . .</b>		<b>143</b>

# List of Figures

Figure 1.1	An example of a symmetry breaking potential, the ‘mexican hat’ potential . . . . .	12
Figure 1.2	Feynman diagram for neutron $\beta$ -decay. . . . .	18
Figure 1.3	The $ft$ values of 20 superallowed nuclear $\beta$ -decays. . . . .	23
Figure 1.4	The time evolution of the NSE abundances of the nuclides of interest. . . . .	27
Figure 1.5	Light element abundances; BBN calculation, and observations. . . . .	28
Figure 2.1	Classification of neutron energies, and velocities. . . . .	31
Figure 2.2	A timeline of neutron lifetime measurements . . . . .	33
Figure 2.3	An exclusion plot of the couplings $g_a$ and $g_v$ . . . . .	35
Figure 2.4	Schematic of the NIST neutron lifetime beam measurement. . . . .	37
Figure 2.5	Schematic of a sextupole field and potential. . . . .	40
Figure 2.6	Permanent magnet gravitrap . . . . .	42
Figure 2.7	Neutron trapping data taken with the Mark II apparatus . . . . .	45
Figure 3.1	The dispersion curves for both the free neutron and superfluid helium. . . . .	48
Figure 3.2	Layout of the NG-6 neutron guide. . . . .	49
Figure 3.3	Spectrum of the neutrons reflected by the NG-6U monochromator . . . . .	50
Figure 3.4	A photograph of the assembled Ioffe trap. . . . .	53
Figure 3.5	Circuit diagram for the active quench protection of the quadrupole magnet. . . . .	55
Figure 3.6	Top view photograph of one field compensating solenoid magnet. . . . .	57
Figure 3.7	Schematic of the operation of a dilution refrigerator. . . . .	58
Figure 3.8	A cross sectional view of the cryostat. . . . .	61
Figure 3.9	Schematic of the Fermilab HTS current leads. . . . .	63
Figure 3.10	HTS high current leads quench detection . . . . .	65
Figure 3.11	A side view of the neutron entrance and shielding materials. . . . .	68
Figure 3.12	A cross section of the experimental cell. . . . .	72
Figure 3.13	A top view of the new light collection system. . . . .	74
Figure 3.14	Lambert’s cosine law. . . . .	75
Figure 3.15	The experimental apparatus used to benchmark a new routine for simulating diffuse reflecting surfaces. . . . .	77

Figure 3.16 The difference in pulse height peak positions for Tyvek and black paper walls. . . . .	79
Figure 3.17 A comparison of simulation and data . . . . .	81
Figure 3.18 Light Collection System from the previous apparatus. . . . .	82
Figure 3.19 Efficiency throughout the collection system as a function of source position. . . . .	83
Figure 3.20 The light collection efficiency in the Mark II apparatus after the 77 K guide. . . . .	85
Figure 3.21 Detection efficiency as a function of axial position within the cell of the new apparatus. . . . .	86
Figure 3.22 Neutron time-of-flight measurements with the reflective polymer vikuiti in the beam. . . . .	89
Figure 3.23 Neutron transmission through the Vikuiti polymer showing the characteristic $1/v$ dependence. . . . .	89
Figure 3.24 Finite element analysis of the cell optical window. . . . .	91
Figure 3.25 Photograph of the 77 K light guide element. . . . .	92
Figure 3.26 A time line of the major events during the run schedule. . . . .	93
Figure 3.27 The digitized waveform of a typical PMT pulse. . . . .	95
Figure 3.28 The DAQ interface with the SCRs to energize the magnets. . . . .	98
Figure 3.29 The relative directional dependance of the origin of background events. . . . .	104
Figure 3.30 The pulse height spectrum from PMT $\beta$ data in the MarkII apparatus. . . . .	105
Figure 4.1 Magnetic field simulations of the KEK trap. . . . .	113
Figure 4.2 Loss probability for a neutron incident on a semi-infinite plane of Tetrphenyl Butadiene. . . . .	115
Figure 4.3 A complex material potential of many steps . . . . .	116
Figure 4.4 Loss probability for a neutron incident on the multi-layered cell wall. . . . .	118
Figure 4.5 The boundary of a rough surface may be treated as a perturbation to the flat plane . . . . .	119
Figure 4.6 The loss probability for neutrons incident on a porous Gore-Tex material. . . . .	122
Figure 4.7 The surface roughness of TPB evaporated on a Gor-Tex substrate. . . . .	123
Figure 4.8 Ramping schedules used in studies of above threshold neutrons. . . . .	126
Figure 4.9 Magnetic field along the surface of the cylindrical cell wall . . . . .	126

# List of Tables

Table 1.1	Weak hypercharge of the fermion fields. . . . .	16
Table 1.2	Fermi and Gamow-Teller decay mode transitions. . . . .	21
Table 3.1	Parameters of the new Ioffe-type magnet trap. . . . .	52
Table 3.2	Activation analysis of the Vikuiti ESR material. . . . .	88
Table 3.3	Status of the magnets at initiation of each of the quenches. . . . .	102
Table 4.1	Properties of the materials in the experimental cell. . . . .	123
Table 4.2	Surface character of the detector insert materials. . . . .	124
Table 5.1	Parameters of the former and current traps used for scaling the signal and background. . . . .	130
Table 5.2	Scaling of signals and backgrounds for statistical uncertainty estimates.	131

# Chapter 1

## Introduction

This thesis describes advancements made in a technique for measuring the neutron lifetime using magnetically trapped ultracold neutrons. The neutron lifetime plays an important role in both nuclear astrophysics and in the standard model of particle physics. Chapter 1 describes the theory of  $\beta$ -decay in detail, and explains the motivations in both of these topics. A discussion of the common techniques used for measuring the neutron lifetime and an analysis of their results can be found in Chapter 2. To address the shortcomings of these techniques a new method that employs magnetic trapping of UCN has been developed.

The knowledge gained from two apparatuses built and operated before this thesis work was used in the design of a new apparatus that is now ready to make a precision measurement of the neutron lifetime. While the previous traps have demonstrated the feasibility of the measurement technique, they were statistically limited from making a precise measurement of the neutron lifetime. The key improvement in the new apparatus is a larger and deeper magnetic trap that utilizes a high-current superconducting quadrupole magnet in an Ioffe configuration. The resulting gain is in the number of neutrons trapped in each run. Details of the design, construction, and commissioning of a new cryostat to support this trap can be found in Chapter 3. Optimizations of the signal collection and background shielding of this apparatus are also discussed here.

In precision measurements a complete understanding of the systematic effects inherent in the measurement technique are just as important as the statistics if one is to make an accurate measurement. Three of the largest contributions of systematic effects to this technique are described in Chapter 4. The isotopic purity of  $^4\text{He}$  used in the production

of ultracold neutrons is one of the largest systematic uncertainties in the experiment. To reduce the uncertainty associated with this, a direct measurement of the isotopic purity of the helium using accelerator mass spectroscopy will be described. The second largest effect comes from neutrons that escape the trap. Also discussed are the neutron interactions with the materials of the experimental cell walls that play an important role in this effect. The third contribution discussed here is the plan for removing systematic effects associated with detector gain drifts.

## 1.1 Chronology of Nuclear Physics

The basis of modern nuclear physics stands on several key discoveries made around the turn of the 20th century. In 1896, Henri Becquerel discovered that uranium salts emit radiation. He showed that photographic plates shielded from sunlight by a dark cloth could be exposed in the presence of uranium[1]. He also found that the exposure was the same if performed in the sunlight on a windowsill, or in the darkness of a drawer. Marie Skłodowska-Curie soon found that the “radioactivity,” a term she and her husband Pierre coined[2], is an atomic property and depends only on the quantity of uranium and not on its chemical composition nor any external conditions.

The discovery of the electron was made in 1897 during a series of three experiments on “cathode rays” performed by J.J. Thomson[3]. In the first experiment, a magnetic field was used to guide a beam through a series of slits in two cylinders. On the inner surface of the second cylinder, Thomson collected the charge, concluding that he was unable to separate the charge from the particles. The second experiment was an attempt to deflect the beam using electric fields. While previous attempts to do this failed as a result of excess gas in the tube that acted to shield the field, an improved vacuum allowed Thomson to succeed. In his third experiment, Thomson measured the charge to mass ratio of the electron by measuring the radius of curvature in a magnetic field. Based on the evidence from these experiments, Thompson made the conclusion that the cathode rays were in fact pieces of atoms he called “corpuscles.”

In 1899 Ernest Rutherford named the two known types of radiation[4], “alpha” and “beta”, and in 1900 when it was discovered by Paul Villard, Rutherford also named “gamma” radiation. These different types of radiation were then distinguished by their penetration through different materials, however they are now identified with particles. An

alpha particle is the nucleus of a helium atom, a beta particle is an electron, and a gamma is a photon.

Between 1909 and 1911, Rutherford, along with his students Geiger and Marsden, conducted an experiment where they scattered alpha particles emitted from a  $^{214}\text{Po}$  source off a thin gold foil[5, 6]. The purpose was to verify or refute the “plum pudding model” of Thompson in which he postulated that the electric charge he had discovered was contained in a positive shell. In this model the positively charged alpha particles would weakly scatter in the forward direction. His findings however, were that a large fraction of the alpha particles in the beam were unaffected, while the remainder were scattered at high angles. This led to his “planetary model” in which the electrons orbited a small positive core. Later in his work of 1919, Rutherford bombarded stable  $^{14}\text{N}$  with alpha particles and found both that positively charged protons were ejected from the nucleus and that the  $^{14}\text{N}$  had transmuted into  $^{17}\text{O}$ [7]. It became clear that the proton was not the complete story of the nucleus, as the mass of the nucleus was found to be much greater than the appropriate number of protons required to conserve charge.

Attempts had begun already in 1921 to understand the continuous spectrum of electrons emitted from nuclei[8]. It was expected that, as in alpha-decay, there was a primary monoenergetic electron emitted from the nucleus. The rest of the spectra of electrons were expected to be secondary, originating from an internal photoelectric effect from gammas leaving the nuclei. These would ionize orbital electrons that contributed to the continuous spectra. Two individuals led competing investigations of this phenomena. Lise Meitner searched for energy conservation of the secondary beta particles with the gamma spectra. From this she hoped to identify the primary beta-decay lines for various beta-emitters. On the contrary, Charles Ellis believed that nuclear gamma radiation preceded the beta-decay. He considered the continuous beta spectrum to be entirely primary electrons and struggled with an explanation that did not violate the conservation of energy. It was not until 1930 that Pauli provided an explanation that would conserve energy. He proposed the neutrino – which he then called the ‘neutron’ – a light neutral particle that is not detected but takes away additional energy from the decay.

In 1932, Irène Joliot-Curie and her husband Frédéric Joliot-Curie irradiated beryllium with alphas from a polonium source. In doing so, they saw recoil protons from a paraffin (hydrogen) target that they attributed to a Compton-like effect from the reaction gammas. However the proton is much heavier than an electron, so it was questionable

that a photon would be able to transfer enough energy to eject a proton from the nucleus. James Chadwick saw this as evidence of a neutral particle that had been postulated by his former mentor Rutherford from the outcome of his proton discovery. Chadwick repeated the experiments of the Joliot-Curies' with paraffin and the additional targets helium and nitrogen. From these indirect measurements, Chadwick was able to deduce that there was an additional neutral particle ejected from the beryllium nuclei that had a mass similar to the proton mass. He called this particle the neutron[9].

Starting with the assumption that the neutrino is needed for conservation of energy in beta decay, Fermi created a theoretical framework for beta decay in 1934[10]. In this theory, modeled after the emission of photons from excited atoms, a neutron decays into a proton with the emission of an electron and a neutrino. The theory has three basic assumptions: 1) the number of electrons and neutrinos are not necessarily constant, they may be created and annihilated, 2) the neutron and proton may be modeled as two internal quantum states of the same particle<sup>1</sup>, and 3) an expression of the conservation of charge is that the Hamiltonian for the process must be reversible. Given these three, the coupling

$$\sum_i (\bar{\psi}_n \mathcal{O}_i \psi_p) (\bar{\psi}_\nu \mathcal{O}_i \psi_e) \quad (1.1)$$

is defined that represents a summation over initial and final states;  $\bar{\psi}_n$  the neutron,  $\psi_p$  the proton,  $\bar{\psi}_\nu$  the anti-neutrino, and  $\psi_e$  the electron. Fermi did not know the mathematical form of  $\mathcal{O}_i$ , and therefore considered all five forms allowed by special relativity; vector, axial vector, scalar, pseudoscalar and tensor. In addition to creating a model of the weak interaction that has changed little from the form in which Fermi originally proposed, this theory also marked Fermi's transition from theory to experiment.

In 1946, together with Zinn[12] and the next year with Marshall[13], Fermi demonstrated experimentally the coherent scattering of neutrons from nuclei in a material, an interaction that is analogous to the index of refraction for light traveling through optical elements. This work results in an effective interaction potential,  $V$ , that acts on the neutron. Along these lines there is a critical grazing angle,  $\theta_c$ , for which neutrons of energy,  $E$ , are reflected from the material,

$$\sin \theta \leq \sin \theta_c = \left( \frac{V}{E} \right)^{1/2}. \quad (1.2)$$

---

<sup>1</sup>This is a statement of the approximate symmetry of isospin first proposed by Heisenberg[11] in 1932

In 1959, Zel'dovich was the first to suggest that using a very small fraction of neutrons in the low energy tail of the spectrum from a reactor, one in principle could use material surfaces to confine neutrons via total internal reflection[14]. Specifically he suggested the use of a graphite bottle to confine the neutrons. The first direct measurements using neutrons that were extracted and stored by this technique using the material potential were made by Groshev *et al.*[15]. Here they extracted neutrons from an aluminum converter near the core of the reactor through electro-polished copper guides. Neutrons meeting the criteria that their energy is low enough to undergo reflections from a material surface at all angles of incidence,  $E \leq V$ , are denoted as ultracold neutrons (see Section 2.2). These neutrons have energies  $\lesssim 3 \times 10^{-7}$  eV.

Today, 76 years after its discovery, precision measurements of the neutron still make significant contributions to our knowledge of the nucleus. Constraints from these measurements on various models can rival the discovery potential of accelerator based physics[16]. A precision measurement of the neutron lifetime is important in the models that astrophysicists use to describe the early universe through the theories of Big Bang Nucleosynthesis (BBN)[17]. It is also a part of a redundant suite of experiments that give evidence for the  $SU(3)_c \otimes SU(2)_L \otimes U(1)_Y$  symmetry assumed in the Standard Model[18]. A detailed explanation of these motivations will follow.

## 1.2 Weak Interactions in the Standard Model

The Standard Model (SM) is a framework of the fundamental particles and their interactions. It is a collection of all theories that successfully describe the observations of nature. As such it is very flexible, and while it is known to be incomplete, new additions continue to be added as discoveries are made. The SM is built on the foundation that the world is composed of fundamental pieces, or particles, and that the quanta is the fundamental limit. In this framework not only are the constituents of atoms quantized, i.e. the electrons and quarks from which nucleons are built, but also the fields through which they interact. Such theories are called gauge theories for the local symmetry that allows for the quantization of fields.

There are many texts devoted to the following formulation of the Standard Model. The following is meant merely to highlight the role of the neutron in the Standard Model and the role precision measurements of the neutron's properties play in further developing

this model. For more detailed discussions of each of the topics discussed, see Ref. [19], [20], [21], and [22].

Quantum Electrodynamics (QED) is the theory in which the interactions of electrodynamics are mediated through a massless gauge boson. In the classical limit this theory is expressed by Maxwell's equations. However, beyond this limit that is defined by the Heisenberg uncertainty principle, the gauge bosons of this theory, photons, need not obey conservation of energy,  $m^2c^4 = E^2 - p^2c^2$ . Since the photon is massless, the range of the interaction is thus infinite as is demonstrated by the  $1/r$  potential of the electromagnetic force.

The Lagrangian density,  $\mathcal{L}_e$ , of the free electron field,  $\psi_e(\vec{x})$ , can be written using “natural” units ( $\hbar = c = 1$ ),

$$\mathcal{L}_e = i\bar{\psi}_e\gamma_\mu\partial^\mu\psi_e - m_e\bar{\psi}_e\psi_e. \quad (1.3)$$

From Eqn. (1.3), where  $\gamma_\mu$  and  $m_e$  are the Dirac matrices and electron mass respectively, the relativistic equations of motion for the free electron can be derived by applying the Euler-Lagrange equations,  $\partial_\mu\left(\frac{\partial\mathcal{L}_e}{\partial[\partial_\mu\psi_e]}\right) - \frac{\partial\mathcal{L}_e}{\partial\psi_e} = 0$ , giving what is known as the Dirac equation,

$$(-i\gamma^\mu\partial_\mu + m_e)\psi_e(x) = 0. \quad (1.4)$$

The simplest mathematical description of such a theory is a statement of the fundamental global and local symmetries that it obeys. The global symmetries of a theory can be either discrete, (i.e. Charge, Parity, and Time-reversal) or continuous. An example of a continuous global symmetry is invariance under transformations such as

$$\psi'(\vec{x}, t) = e^{-i\rho}\psi(\vec{x}, t). \quad (1.5)$$

Here  $\rho$  is a constant over all time and space, thus the transformation is considered a global transformation. Because this transformation,  $U = e^{-i\rho}$ , commutes with the Dirac equation, the theory possesses this global symmetry

$$\begin{aligned} (-i\gamma^\mu\partial_\mu + m_e)\psi'_e(x) &= (-i\gamma^\mu\partial_\mu + m_e)e^{-i\rho}\psi_e(x) \\ &= e^{-i\rho}(-i\gamma^\mu\partial_\mu + m_e)\psi_e(x) = 0. \end{aligned} \quad (1.6)$$

Noether's theorem states that for every global symmetry for which the Lagrange density remains invariant, there exists a conserved quantity or corresponding conservation law. In classical mechanics, the conservation of momentum, angular momentum, and energy

follow from translational, rotational, and time invariances of the Lagrangian. These are examples of global symmetries. Similarly, symmetries exist that are local, that is to say the phase of the invariant transformation is a function of space and time

$$\psi'(\vec{x}, t) = e^{ie\rho(x)}\psi(\vec{x}, t). \quad (1.7)$$

Now applying a local transformation such as seen in Eqn. (1.7), one can see that the Dirac equation is invariant

$$\begin{aligned} (-i\gamma^\mu\partial_\mu + m_e)\psi'_e(x) &= (-i\gamma^\mu\partial_\mu + m_e)e^{ie\rho(x)}\psi_e(x) \\ &= e^{ie\rho(x)}[(-i\gamma^\mu\partial_\mu + m_e)\psi_e(x) + e(\partial_\mu\rho(x))\psi_e(x)] \\ &= e(\partial_\mu\rho(x))\psi_e(x) \neq 0. \end{aligned} \quad (1.8)$$

However with the addition of an interaction term in the transformation that tracks the local variations of the field transformation, the invariance can be maintained.

To accomplish this, one must modify the derivative that acts on the electron field in Eqn. (1.4). The new operator that is introduced is called the covariant derivative,  $D_\mu$ . Substituting the covariant derivative into the Dirac equation, one can show how it is invariant under a local transformation such as Eqn. (1.7)

$$\partial_\mu \rightarrow \partial_\mu - ie\partial_\mu\rho(x) = D_\mu. \quad (1.9)$$

The final step in creating a gauge theory for electrodynamics is by associating the correction,  $i\partial_\mu\rho(x)$ , to the Dirac equation with an interaction with the photon field  $A_\mu$ .

$$\begin{aligned} i\gamma^\mu(\partial_\mu - ieA_\mu(x))\psi_e(x) &= m_e\psi_e(x) \\ i\gamma^\mu\{\partial_\mu - ie(A_\mu(x) + \partial_\mu\rho(x))\}\psi'_e(x) &= m_e\psi'_e(x) \\ i\gamma^\mu(\partial_\mu - ieA'_\mu(x))\psi'_e(x) &= m_e\psi'_e(x), \end{aligned} \quad (1.10)$$

where

$$A'_\mu(x) = A_\mu(x) + \partial_\mu\rho(x). \quad (1.11)$$

Therefore, under simultaneous gauge (local) transformations, Eqns. (1.7) and (1.11), the equations of motion remain invariant. For this reason one calls the photon field  $A_\mu$  a gauge field of the theory. In terms of the 4-potential,

$$\begin{pmatrix} A_0 \\ \vec{A} \end{pmatrix} = \begin{pmatrix} \varphi(x) \\ \vec{A}(x) \end{pmatrix}, \quad (1.12)$$

corresponding with the electrostatic potential and the vector potential from classical electrodynamics.

The tensor  $F_{\mu\nu} = \partial_\mu A_\nu - \partial_\nu A_\mu$  is then a representation of electric and magnetic fields. Using  $\vec{E} = -\vec{\nabla}\varphi - \partial_t \vec{A}$  and  $\vec{B} = \vec{\nabla} \times \vec{A}$ , the expression for the electric and magnetic fields can be represented as  $E^i = F^{0i}$ , and  $\epsilon^{ijk} B^k = -F^{ij}$ . Therefore Maxwell's equations can be written:

$$\epsilon^{\mu\nu\alpha\beta} \partial_\nu F_{\alpha\beta} = 0, \quad \partial_\mu F^{\mu\nu} = e j^\nu, \quad (1.13)$$

where  $j^\mu = (\rho, \vec{J})^\dagger$  is the 4-vector electromagnetic current.

Maxwell's equations are invariant under gauge transformations. For consistency one may verify this by making the transformation given by Eqn. (1.11):

$$\begin{aligned} \partial_\mu F^{\mu\nu} &= \partial_\mu \partial^\mu A'^\nu - \partial_\mu \partial^\nu A'^\mu \\ &= \partial_\mu \partial^\mu A^\nu - \partial_\mu \partial^\nu A^\mu + \underbrace{\partial_\mu \partial^\mu \partial^\nu (\rho(x)) - \partial_\mu \partial^\nu \partial^\mu (\rho(x))}_{=0} = e j^\nu. \end{aligned} \quad (1.14)$$

Additionally, by virtue of the invariance of Eqn. (1.11), the gauge photon must be massless. If one forces a mass term into Maxwell's equations  $(\partial_\mu \partial^\mu - m^2)A^\nu - \partial_\mu \partial^\nu A^\mu = e j^\nu$ , they no longer remain invariant under Eqn. (1.11),

$$m^2 A'_\mu = m^2 A_\mu + m^2 \partial_\mu \rho \neq m^2 A_\mu. \quad (1.15)$$

Such gauge transformations tend to produce massless gauge fields. Therefore, with the goal of extending this theory to the weak interaction with gauge fields that are massive, one must employ the additional constraint of spontaneous symmetry breaking in order to impart mass to the gauge fields once they have been created through gauge invariance. To complete the theory, one should now write a new Lagrange density that includes the free electron, the electron-photon interactions, and the free photon,

$$\mathcal{L}_e = \bar{\psi}_e(x)(i\gamma_\mu D_\mu - m)\psi_e(x) - \frac{1}{4} F^{\nu\mu} F_{\nu\mu}. \quad (1.16)$$

By applying the Euler-Lagrange equation, it can be shown that the equations of motion for the free electron can be recovered as well as Maxwell's equations, which are the equations of motion for a free photon. Also, it has been shown that the theory of QED is invariant to transformations belonging to the circle group  $U(1)$  because of simultaneous interactions with the photon gauge field.

### 1.2.1 Yang-Mills Theory

In constructing a similar gauge theory of the weak interaction, it is necessary to determine the irreducible representation for its symmetry group. These are a group of interactions that are of the form represented by Eqn. (1.1) in which, for instance, a quark is transformed within its family and a lepton and its anti-neutrino are created. These interactions are also responsible for leptonic processes in which they transform a charged lepton into its family's anti-neutrino and produce a charged lepton of another family and its anti-neutrino. Additionally the interactions can be responsible for transformations that do not involve leptons. Charge conservation requires that quark combinations have  $\pm e$ , 0 charge through a neutral current coupling. The range of the interactions is finite, of order  $10^{-16}$  cm, and therefore the gauge bosons are massive. The families of leptons and quarks that the weak force couples fall naturally into doublet representations,

$$\begin{pmatrix} \nu_e \\ e \end{pmatrix}, \quad \begin{pmatrix} \nu_\mu \\ \mu \end{pmatrix}, \quad \begin{pmatrix} \nu_\tau \\ \tau \end{pmatrix}, \\ \begin{pmatrix} u \\ d \end{pmatrix}, \quad \begin{pmatrix} c \\ s \end{pmatrix}, \quad \begin{pmatrix} t \\ b \end{pmatrix}. \quad (1.17)$$

The irreducible representation of symmetry group of  $SU(2)$  has three generators that operate on doublets of the form given by Eqn. (1.17),  $\psi_D(x)$ . Moreover, it is known from experience with spin and angular momentum that through the appropriate choice of a basis state, one can combine the generators of  $SU(2)$  to create raising and lowering operators that transform between the two elements of such a doublet. Even though it will generate massless bosons, it is nonetheless tempting to form a gauge theory similar to that of QED with the  $SU(2)$  symmetry group to describe the weak interaction. Starting with the symmetry transformations that may be represented as:

$$\begin{aligned} \psi_D(x) &\rightarrow \psi'_D(x) = e^{-i\tau^a \alpha^a(x)} \psi_D(x) \\ \text{For } \alpha(x) \ll 1, \quad \psi'_D(x) &= (1 - i\alpha^a(x)\tau^a) \psi_D(x). \end{aligned} \quad (1.18)$$

where the latter expression is the former expressed in its infinitesimal form.  $\tau^a = \sigma^a/2$  are a representation of the Pauli matrices, the generators of  $SU(2)$  symmetry, and therefore obey the commutation relation that is characteristic of the symmetry,

$$[\tau^i, \tau^j] = 2i\epsilon^{ijk}\tau^k. \quad (1.19)$$

By analogy with the electrodynamics construction, one can create a covariant derivative that follows the new symmetry with the substitution

$$\partial_\mu \rightarrow \partial_\mu + i(\partial_\mu \alpha^a(x))\tau^a/2. \quad (1.20)$$

If the physical interpretation of the covariant derivative is truly analogous to that of the electromagnetic case, one can associate a new gauge particle field,  $W_\mu^a(x)$  with the correction to the derivative in the Dirac equation,

$$D_\mu = \partial_\mu + \frac{ig}{2}W_\mu^a(x)\tau^a. \quad (1.21)$$

Next, one must find the transformation to  $W_\mu^a$  that must occur simultaneously with Eqn. (1.18) in order to preserve the invariance. Substitution of this new covariant derivative into the Dirac equation will again give the required transformation,

$$W_\mu^i{}'(x) = W_\mu^i(x) + \frac{1}{g}\partial_\mu \alpha^i(x) - \epsilon_{ijk}W_\mu^j(x)\alpha^k(x). \quad (1.22)$$

Unlike Eqn. (1.11), an additional term,  $-\vec{W}_\mu \times \vec{\alpha}(x)$ , arises because the generators of  $SU(2)$  do not commute. Modeling the field strength tensor after the QED representation of Maxwell's equations, one obtains

$$E_{\mu\nu}^i = \partial_\mu W_\nu^i - \partial_\nu W_\mu^i + g\epsilon_{ijk}W_\mu^j W_\nu^k. \quad (1.23)$$

One can now write the Lagrange density,

$$\mathcal{L}_{YM} = \bar{\psi}_D(x)(i\gamma_\mu D_\mu - m)\psi_D(x) - \frac{1}{4}E^{\nu\mu}E_{\nu\mu}. \quad (1.24)$$

This is designated as the Yang-Mills theory, a non-abelian gauge theory where the generators of the gauge symmetry do not commute. This looks like a promising theory of the weak interaction – there are three vector gauge bosons created, two of which can change between the differently charged doublet state elements by a factor of  $\pm e$ . This is easy to see when one changes to basis states analogous with the raising and lowering operators of the  $SU(2)$  symmetry,

$$W_\mu^\pm = \frac{1}{\sqrt{2}}(W_\mu^1 \mp iW_\mu^2). \quad (1.25)$$

The third component,  $W_\mu^3$ , of the triplet does not mix the incoming states and therefore describes a neutral current that did not exist in the Fermi theory of beta-decay. Later one will see how this is a part of the Glashow-Weinberg-Salam theory, however it will be

modified from the present form. A problem with this theory is that the masses of the doublet states are assumed to be equivalent. For the  $(n\ p)$  doublet this may be approximately true, although this assumption clearly breaks down in the case of the lepton doublets. Also, the gauge bosons in this theory are massless, where in reality they must be massive. These failures will be addressed through a spontaneous breaking of the gauge symmetry.

### 1.2.2 Glashow-Weinberg-Salam Theory of Weak Interactions

The theory of Glashow, Weinberg, and Salam (GWS) unifies the weak interaction with electromagnetics by combining the symmetries of the previous sections as  $SU(2) \otimes U(1)$ . It is important to note that the  $SU(2)$  symmetry cannot be uniquely identified with the weak interaction nor the  $U(1)$  symmetry uniquely identified with QED. The GWS theory explicitly includes the Higgs mechanism to impart mass to the gauge bosons of the theory. The Higgs mechanism is a spontaneous breaking in the symmetry of the vacuum state under transformations of the gauge symmetry. Here the vacuum state is not empty space, rather it is the ground state of the quantum fields, that is to say it is the state of minimum energy. It is not necessary that the vacuum expectation value is vanishing and it may be a degenerate set of states. It is this degeneracy that ‘breaks’ the symmetry. Such a ground state would be realized if the fields are under the influence of a potential such as the so-called Mexican hat potential, Figure 1.1.

Since such a potential doesn’t exist in the theories formulated to this point, it is generally accepted that there must be an additional field that interacts in this manner and thereby imparts a mass to the otherwise massless gauge bosons. This field, a complex isodoublet scalar field called the Higgs field,

$$\phi = \frac{1}{\sqrt{2}} \begin{pmatrix} \phi_1 + i\phi_2 \\ \phi_3 + i\phi_4 \end{pmatrix}, \quad (1.26)$$

has not been experimentally observed thus far.

The Lagrangian for such a field looks like the Klein-Gordon equations for a complex scalar field plus a “ $\phi^4$ ” self-interaction term,

$$\mathcal{L} = (\partial_\mu \phi^\dagger)(\partial^\mu \phi) - \mathcal{M}^2 \phi^\dagger \phi - \lambda(\phi^\dagger \phi)^2, \quad (1.27)$$

where  $\mathcal{M}$  would represent an effective mass of the scalar particle and  $\lambda$  the strength of the self-interactions experienced by the particle. The Hamiltonian of such a system defines the

potential energy,

$$V = \mathcal{M}^2 \phi^\dagger \phi + \lambda (\phi^\dagger \phi)^2. \quad (1.28)$$

Since the Hamiltonian for the potential qualitatively described by Figure 1.1 corresponds to an energy density, the value of  $\lambda$  must be positive definite. The value of  $y = \phi^\dagger \phi$  is also positive, thus when  $\mathcal{M}^2 > 0$ ,  $V$  is minimized when  $\phi = 0$ . In this case, the full symmetry of the Lagrangian is maintained. However if  $\mathcal{M}^2 < 0$ , then  $V$  is minimized where  $\phi^\dagger \phi = -\mathcal{M}^2/2\lambda \neq 0$ . We can therefore pick any basis of Eqn. (1.26) that minimizes the energy,

$$\langle \phi \rangle = \phi_{min} = \frac{1}{\sqrt{2}} \begin{pmatrix} 0 \\ v \end{pmatrix} \quad \text{where } v = \sqrt{\mathcal{M}^2/\lambda}. \quad (1.29)$$

However there are infinitely many degenerate states that also minimize the energy,  $\phi'_{min} = e^{i\alpha\tau^a} \phi_{min} \neq \phi_{min}$ . Thus the global  $SU(2)$  symmetry is broken.

Now consider small local excitations around the field minimum,

$$\phi_{min} = \frac{1}{\sqrt{2}} e^{i\xi^a(x)\tau^a} \begin{pmatrix} 0 \\ v + \eta(x) \end{pmatrix}. \quad (1.30)$$

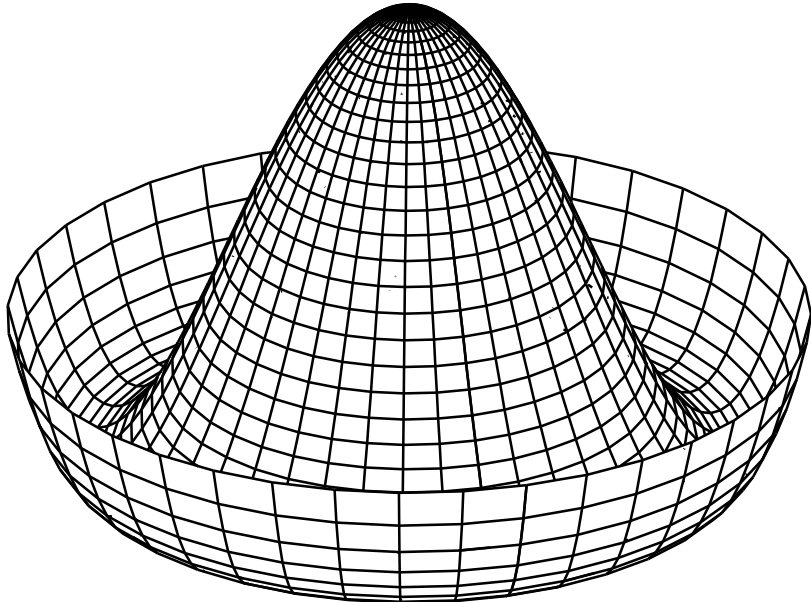


Figure 1.1: The mexican hat potential in polar coordinates is an example of a potential that has a non-zero minimum and infinitely many degenerate minimum states[23].

Since it was shown that three massless bosons are usually associated with broken  $SU(2)$  symmetry, one could try to identify the  $\xi^a$ 's with the massless Goldstone bosons, yet it can be shown that under local  $SU(2)$  invariance that the  $\xi^a$  field has no physical consequence,

$$\begin{aligned}\phi'_{min} = e^{-i\xi^a(x)\tau^a} \phi_{min} &= \frac{1}{\sqrt{2}} e^{-i\xi^a(x)\tau^a} e^{i\xi^a(x)\tau^a} \begin{pmatrix} 0 \\ v + \eta(x) \end{pmatrix} \\ &= \frac{1}{\sqrt{2}} \begin{pmatrix} 0 \\ v + \eta(x) \end{pmatrix}.\end{aligned}\quad (1.31)$$

The local excitation  $\eta^a$  can however be identified with the massive spin-1 Higgs boson. Using the basis state in Eqn. (1.31) and expanding about the minimum of  $V$  from Eqn. (1.28), the Higgs mass can be shown to be  $M_\eta = \sqrt{2\mathcal{M}^2}$ .

In order for the Lagrangian in Eqn. (1.27) to maintain invariance to the  $SU(2) \otimes U(1)$  symmetry, one must replace the partial derivatives with covariant derivatives in order to preserve the symmetry,

$$\phi \rightarrow e^{i\tau^a \alpha^a(x)} e^{i\beta(x)/2} \phi. \quad (1.32)$$

Or equivalently,

$$D_\mu \phi = (\partial_\mu - igW_\mu^a T^a - ig'B_\mu Y) \phi. \quad (1.33)$$

Here the  $W_\mu^a$ 's are the gauge fields associated with the  $SU(2)$  symmetry,  $B_\mu$  is the gauge field associated with the  $U(1)$  symmetry, and their respective couplings  $g$  and  $g'$ . The quantization  $T^a$  and  $Y$  are meant to reflect the fraction each symmetry contributes. For now, assume  $T^a = \tau^a$  and  $Y = 1/2$ , however this will change depending on specific particle couplings. As was shown in Eqn. (1.25),  $W^+$  and  $W^-$  are the basis in which the  $W$  transfers between the doublet of the field. To see how the broken symmetry of  $\phi$  gives rise to the  $W$ 's mass, consider just the kinetic portion of the Lagrangian in Eqn. (1.27) that includes the  $W$ 's coupling to the Higgs field doublet:

$$\begin{aligned}(D_\mu \phi)^\dagger (D^\mu \phi) &= \left\{ (\partial_\mu + \frac{ig}{2} \tau^a W_\mu^a) \phi \right\}^\dagger (\partial^\mu + \frac{ig}{2} \tau^a W^{a\mu}) \phi. \\ &= \frac{g^2}{4} W_\mu^a W^{a\mu} \phi^\dagger \phi + \dots\end{aligned}\quad (1.34)$$

Expanding this about the vacuum expectation value given in Eqn. (1.29) yields,

$$(D_\mu \phi)^\dagger (D^\mu \phi) = \frac{g^2 v^2}{8} W_\mu^a W^{a\mu} + \frac{g^2 v}{8} W_\mu^a W^{a\mu} 2\eta + \dots \quad (1.35)$$

A full application of the Euler-Lagrange equations will lead to an equation similar in form to Maxwell's equations for the  $A_\mu$  photon fields with an additional mass term:

$$\left(\partial_\mu\partial^\mu + \frac{g^2v^2}{4}\right)W_\mu^a = J_\mu^w, \quad (1.36)$$

where  $J_\mu^w$  is a source current for the charged weak interactions. The mass term here is that of the W boson,  $M_W = gv/2$ .

Next considering the coupling of the neutral components with the Higgs vacuum expectation value, one can again focus on a portion of the Lagrangian in Eqn. (1.27),

$$\begin{aligned} \mathcal{L} &= \frac{1}{4}[(gW_\mu^3\tau^3 + g'B_\mu)\phi]^\dagger[gW^{3\mu}\tau^3 + g'B^\mu]\phi \\ &= \frac{v^2}{8}(-gW_\mu^{3\dagger} + g'B_\mu^\dagger)(-gW^{3\mu} + g'B^\mu) \\ &= \frac{v^2}{8} \begin{pmatrix} W_\mu^{3\dagger} & B_\mu^\dagger \end{pmatrix} \begin{pmatrix} g^2 & -gg' \\ -gg' & g'^2 \end{pmatrix} \begin{pmatrix} W^{3\mu} \\ B^\mu \end{pmatrix}. \end{aligned} \quad (1.37)$$

This term is equivalent to the W mass term from the Lagrangian in Eqn. (1.35), but here the mass is mixed between the fields  $W_\mu^3$  and  $B_\mu$ ,

$$M = \frac{v^2}{4} \begin{pmatrix} g^2 & -gg' \\ -gg' & g'^2 \end{pmatrix}. \quad (1.38)$$

Therefore, these fields are not the principal eigenvectors and one cannot interpret them as the gauge bosons. This matrix is diagonalized by the transformation  $M_d = U^{-1}MU$ ,

$$U = \frac{1}{\sqrt{g'^2 + g^2}} \begin{pmatrix} g' & g \\ -g & g' \end{pmatrix}, \quad (1.39)$$

with the important result that one eigenvalue of this matrix is zero. It is thus natural to assign the eigenvector of this basis with the photon gauge field. The other eigenvalue is non-zero,  $M_Z = v^2(g'^2 + g^2)/2$  and can be associated with the mass of the neutral Z boson. With a little foresight one might have expected this result from Eqn. (1.32) as there is clearly a choice in the basis,  $\alpha^1 = \alpha^2 = 0$  and,  $\alpha^3 = \beta$  for which the symmetry will remain preserved.

To build a more physical picture it is useful to rewrite the covariant derivative in Eqn. (1.33) in terms of the mass eigenstates

$$D_\mu = \partial_\mu - i\frac{g}{\sqrt{2}}(W_\mu^+T^+ + W_\mu^-T^-) - i\frac{1}{\sqrt{g'^2 + g^2}}Z_\mu(g^2T^3 - g'^2Y) - i\frac{gg'}{\sqrt{g'^2 + g^2}}A_\mu(T^3 + Y). \quad (1.40)$$

In this basis one recovers the couplings that were derived in the beginning of the section from the last term here if one assigns the electric charge,

$$e = \frac{gg'}{\sqrt{g'^2 + g^2}}. \quad (1.41)$$

Its quantum number  $Q = (T^3 + Y)$  follows from the transformation  $U$ . Since  $U$  is a rotation of the basis states, it is customary to express it in terms of the weak mixing angle, also called the Weinberg angle,  $\theta_w$ , where

$$\cos \theta_w = \frac{g}{\sqrt{g'^2 + g^2}} \quad \text{and} \quad \sin \theta_w = \frac{g'}{\sqrt{g'^2 + g^2}}. \quad (1.42)$$

Thus one has,

$$A_\mu = B_\mu \cos \theta_w + W_\mu^3 \sin \theta_w \quad (1.43)$$

and

$$Z_\mu = -B_\mu \sin \theta_w + W_\mu^3 \cos \theta_w. \quad (1.44)$$

Further simplifying the covariant derivative, it is defined by just two physical parameters,  $e$  and  $\theta_w$ , reducing Eqn. (1.40) to

$$D_\mu = \partial_\mu - i \frac{g}{\sqrt{2}} (W_\mu^+ T^+ + W_\mu^- T^-) - i \frac{g}{\cos \theta_w} Z_\mu (T^3 - Q \sin^2 \theta_w) - ie A_\mu Q \quad (1.45)$$

where,

$$g = \frac{e}{\sin \theta_w}. \quad (1.46)$$

In order to accurately describe nature, one must also include the spin-dependent weak interactions. There are five different covariant forms that the weak interaction Lagrangian could take ( $1, \gamma_\mu, \sigma_{\mu\nu}, i\gamma_5\gamma_\mu$ , or  $\gamma_5$ ) or equivalently scalar (S), vector (V), tensor (T), axial vector (A), or pseudoscalar (P) respectively.

Parity non-conservation was demonstrated by C. S. Wu *et al.* in the decay of  $^{60}\text{Co}$  at the National Bureau of Standards in 1957[24]. Around that same time, Marshak and Sudarshan[25], and independently Feynmann and Gell-Mann[26], showed that the form of the weak interaction couplings should be  $V - A$ ,

$$\frac{\gamma^\mu - \gamma^\mu \gamma^5}{2} = \frac{\gamma^\mu}{2} (1 - \gamma^5). \quad (1.47)$$

The physical implication is that the weak interactions will only couple with left handed fermions or their right handed anti-particles, as  $(1 - \gamma^5)/2$  is the projection operator for left handed helicity.

Table 1.1: Weak hypercharge of the fermion fields.

		Fermion Multiplets			$Q$	$T^3$	$Y$
Leptons	$\begin{pmatrix} \nu_e \\ e \end{pmatrix}_L$	$\begin{pmatrix} \nu_\mu \\ \mu \end{pmatrix}_L$	$\begin{pmatrix} \nu_\tau \\ \tau \end{pmatrix}_L$	0	$\frac{1}{2}$	$-\frac{1}{2}$	
	$\nu_{eR}$	$\nu_{\mu R}$	$\nu_{\tau R}$	-1	$-\frac{1}{2}$	$-\frac{1}{2}$	
	$e_R$	$\mu_R$	$\tau_R$	0	0	0	
Quarks	$\begin{pmatrix} u \\ d \end{pmatrix}_L$	$\begin{pmatrix} c \\ s \end{pmatrix}_L$	$\begin{pmatrix} t \\ b \end{pmatrix}_L$	$\frac{2}{3}$	$\frac{1}{2}$	$\frac{1}{6}$	
	$u_R$	$c_R$	$t_R$	$-\frac{1}{3}$	$-\frac{1}{2}$	$\frac{1}{6}$	
	$d_R$	$s_R$	$b_R$	$\frac{2}{3}$	0	$\frac{2}{3}$	
				$-\frac{1}{3}$	0	$-\frac{1}{3}$	

The kinetic terms of the Dirac Lagrangian can be broken into separate left handed and right handed portions, so it is not a problem for the weak interactions to couple differently to the left handed and right handed parts,

$$\bar{\psi}D_\mu\psi = \bar{\psi}_L D_\mu\psi_L + \bar{\psi}_R D_\mu\psi_R. \quad (1.48)$$

Therefore, by choice of convenience one can define left handed lepton and quark isodoublets that couple to both electromagnetic fields and weak fields, with both weak isospin  $T$  and hypercharge  $Y$ , and right handed isosinglets that only couple with the  $U(1)$  hypercharge,

$$E_L^i = \begin{pmatrix} \nu^i \\ e^i \end{pmatrix}_L; \quad \nu_R^i, e_R^i \quad (1.49)$$

$$Q_L^i = \begin{pmatrix} u^i \\ d^i \end{pmatrix}_L; \quad u_R^i, d_R^i. \quad (1.50)$$

Tabulating the charge and the weak hypercharge of the leptons and quarks provides lookup tables for how the covariant derivatives of their couplings should be expressed.

At this point one has all the information needed to describe the electroweak couplings between the vector bosons and the fermion fields,

$$\mathcal{L}_{int} = \sum_f \bar{f} (i\gamma^\mu D_\mu - m_f) f. \quad (1.51)$$

The sum over  $f$  indicates a sum over all lepton and quark fields defined by Eqns. (1.49) and (1.50). Substituting the charges, weak isospins, and hypercharges from the Table 1.1 into

the covariant derivative given in Eqn. (1.45) this can be re-written more explicitly,

$$\begin{aligned} \mathcal{L}_{int} = & \overline{E}_L^i i \gamma^\mu \partial_\mu E_L^i + \overline{e}_R^i i \gamma^\mu \partial_\mu e_R^i + \overline{Q}_L^i i \gamma^\mu \partial_\mu Q_L^i + \overline{u}_R^i i \gamma^\mu \partial_\mu u_R^i + \overline{d}_R^i i \gamma^\mu \partial_\mu d_R^i \\ & + g(W_\mu^+ J_W^{\mu+} + W_\mu^- J_W^{\mu-} + Z_\mu^0 J_{EM}^\mu) + e A_\mu J_{EM}^\mu, \end{aligned} \quad (1.52)$$

where,

$$J_W^{\mu+} = \frac{1}{\sqrt{2}} (\overline{\nu}_L^i \gamma^\mu e_L^i + \overline{u}_L^i \gamma^\mu d_L^i) \quad (1.53)$$

$$J_W^{\mu-} = \frac{1}{\sqrt{2}} (\overline{e}_L^i \gamma^\mu \nu_L^i + \overline{d}_L^i \gamma^\mu u_L^i) \quad (1.54)$$

$$\begin{aligned} J_Z^0 = & \frac{1}{\cos \theta_w} \left[ \overline{\nu}_L^i \gamma^\mu \left( \frac{1}{2} \right) \nu_L^i + \overline{e}_L^i \gamma^\mu \left( -\frac{1}{2} + \sin^2 \theta_w \right) e_L^i + \overline{e}_R^i \gamma^\mu \left( \sin^2 \theta_w \right) e_R^i \right. \\ & + \overline{u}_L^i \gamma^\mu \left( \frac{1}{2} - \frac{2}{3} \sin^2 \theta_w \right) u_L^i + \overline{u}_R^i \gamma^\mu \left( -\frac{2}{3} \sin^2 \theta_w \right) u_R^i \\ & \left. + \overline{d}_L^i \gamma^\mu \left( -\frac{1}{2} + \frac{1}{3} \sin^2 \theta_w \right) d_L^i + \overline{d}_R^i \gamma^\mu \left( \frac{1}{3} \sin^2 \theta_w \right) d_R^i \right] \end{aligned} \quad (1.55)$$

$$J_{EM}^\mu = \overline{e}^i \gamma^\mu (-1) e^i + \overline{u}^i \gamma^\mu \left( \frac{2}{3} \right) u^i + \overline{d}^i \gamma^\mu \left( -\frac{1}{3} \right) d^i \quad (1.56)$$

Here the  $J_{EM}^\mu = \overline{\psi} \gamma^\mu \psi$  is a conserved Noether current that is a consequence of conservation of gauge invariance of the photon field (Eqn. (1.14)). Likewise the remaining vector parts of the weak currents also form a conserved Noether current associated with the invariance of chiral  $SU(2)$  symmetry,  $V^{\mu a} = \frac{1}{2} \overline{\psi} \gamma^\mu \tau^a \psi$ . This is known as the conserved vector current (CVC) hypothesis and has the consequence that the vector couplings are universal for all weak processes, leptonic, semi-leptonic or non-leptonic. Thus the vector coupling is not modified in any way by the strong force in hadrons. This same statement however is not true for the axial-vector current  $A^{\mu a} = \frac{1}{2} \overline{\psi} \gamma^\mu \gamma^5 \tau^a \psi$ . It will be shown that this is responsible for hadronic flavor changing in the weak interaction.

### 1.3 Beta Decay

The nuclei of ordinary matter, composed of protons and neutrons, may be unstable due to weak interactions through  $\beta$ -decay. The most fundamental  $\beta$ -decay in the nucleus is that of the free neutron. The rest mass of the proton is slightly less than that of the neutron;  $m_p = 938.28 \text{ MeV}/c^2$  is 0.14% less massive than  $m_n$ . Therefore the decay process of

$$n \longrightarrow p + e^- + \overline{\nu}_e + 782 \text{ keV} \quad (1.57)$$

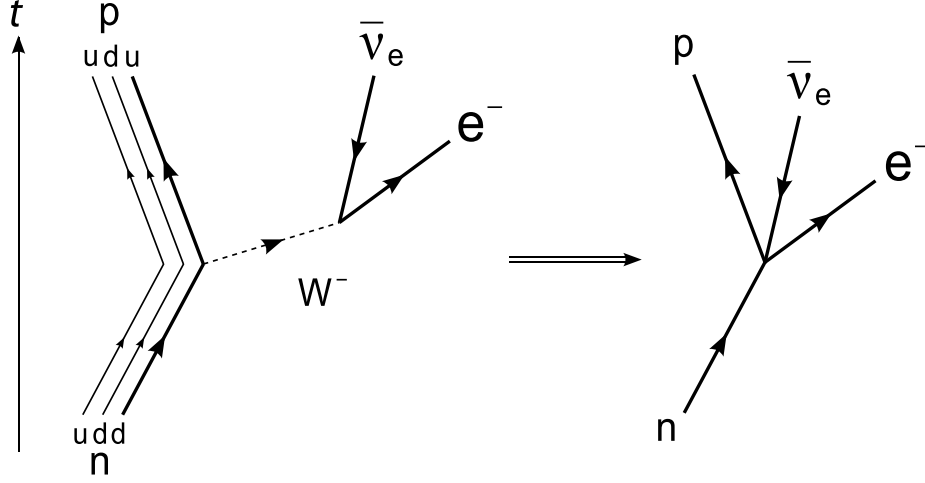


Figure 1.2: Feynman diagram for neutron  $\beta$ -decay[27]. In the limit of low momentum transfer (on right) the current-current Fermi model of beta decay is still valid.

is allowed by the exchange of a  $W^-$  boson. Conservation of energy requires that the remainder of energy is taken by the kinetic energy of the final state particles.

As the energy transfer in weak decay processes is considerably less than the mass of the  $W^-$  boson ( $m_W = 80.4$  GeV), the range of this interaction is short and therefore it is valid to approximate the interaction by the Fermi current-current interaction described by the Hamiltonian

$$H = \frac{G_F}{\sqrt{2}} J_{\mu W}^- J_W^{\mu+}. \quad (1.58)$$

and shown graphically in Figure 1.2. Here  $G_F$  is the Fermi coupling constant.

As was shown in Eqn. (1.56), the currents can be separated into leptonic,  $l_\mu^c$ , and hadronic,  $h_\mu^c$ , components. The leptonic part can be expressed as

$$l_\mu^c = \bar{e}^i \gamma^\mu (c_v + c_a \gamma^5) \nu_e^i = \bar{e}^i \gamma^\mu (1 - \gamma^5) \nu_e^i. \quad (1.59)$$

While the lepton interaction is pure  $V - A$ ,  $c_v = 1$  and  $c_a = -1$  are the vector and axial vector couplings respectively. For this reason, if one ignores neutrino masses and the resulting neutrino flavor changes, there are no flavor changing transitions in leptons. This is known as  $e - \mu - \tau$  universality. It is thus possible to determine the Fermi coupling constant  $G_F$  from purely leptonic decays such as  $\mu$ -decays that can be approximated by the Hamiltonian given in Eqn. (1.58). The hadronic component of the charged weak current is not as straightforward as the lepton current because it is modified by the strong force

interacting with the quarks. This accounts for the experimentally observed flavor changing decays such as  $\Lambda$ -decay in which

$$s \rightarrow u + e^- + \bar{\nu}_e. \quad (1.60)$$

This decay process is completely analogous to neutron decay with the substitution of a strange quark that decays instead of a down quark.

This phenomena can be fundamentally explained if the mass eigenstates of the quarks, analogous to the  $W$  mass eigenstates of Eqn. (1.38), are not exactly the same eigenstates that participate in the weak interaction, Eqns. (1.50) and (1.49). Transformation from mass eigenstates to the weakly interacting eigenstate can be obtained by a unitary transformation  $U^{ij}$ ,

$$u_L^{\prime i} = U_u^{ij} u_L^j \quad (1.61)$$

and

$$d_L^{\prime i} = U_d^{ij} d_L^j, \quad (1.62)$$

with the resulting  $W$  boson current

$$h^c = \frac{1}{\sqrt{2}} \bar{u}_L^{\prime i} \gamma^\mu d_L^{\prime j} = \frac{1}{\sqrt{2}} \bar{u}_L^i \gamma^\mu (U_i^\dagger U_j) d_L^j. \quad (1.63)$$

Here  $U_i^\dagger U_j = V_{ij}$  where,

$$\begin{pmatrix} V_{ud} & V_{us} & V_{ub} \\ V_{cd} & V_{cs} & V_{cb} \\ V_{td} & V_{ts} & V_{tb} \end{pmatrix} = \begin{pmatrix} 0.97419 \pm 0.00022 & 0.2257 \pm 0.0010 & 0.00359 \pm .00016 \\ 0.2256 \pm 0.0010 & 0.97334 \pm 0.00023 & 0.0415_{-0.0011}^{+0.0010} \\ 0.00874_{-0.00037}^{+0.00026} & 0.0407 \pm 0.0010 & 0.999133_{-0.000043}^{+0.000044} \end{pmatrix} \quad (1.64)$$

is the 3 by 3 unitary matrix known as the Cabibbo-Kobayashi-Maskawa (CKM) matrix. While the measured values shown here[18] highlight the small scale of the mixings, off diagonal entries in this matrix allow for transitions between quark generations. In beta-decay

$$h_\gamma^c = V_{ud} \bar{u}^i \gamma^\mu (1 + \lambda \gamma^5) d_\mu^i = G_F^{-1} \bar{u}^i \gamma^\mu (g_v + g_a \gamma^5) d_\mu^i. \quad (1.65)$$

Due to the CVC, the vector current is conserved. However, the axial-vector portion of the hadronic current is modified by the free parameter,  $\lambda = g_a/g_v$ , from its form in Eqn. (1.55).

Limiting to  $V-A$  interactions, and applying Fermi's golden rule to the Hamiltonian in Eqn. (1.58), one arrives at a transition probability that can be parameterized in terms

of the nuclear spin and the electron and neutrino energies and momenta. In beta-decay of polarized neutrons, the distribution in electron and neutrino directions and electron energy of the transition probability is given by[28]:

$$\omega(E_e, \Omega_e, \Omega_\nu) = dE_e d\Omega_e d\Omega_\nu F(E_e) G_F^2 V_{ud}^2 (1 + 3\lambda^2) \left[ 1 + a \frac{\vec{p}_e \cdot \vec{p}_\nu}{E_e E_\nu} + b \frac{m_e}{E_e} + \vec{\sigma}_n \cdot \left( A \frac{\vec{p}_e}{E_e} + B \frac{\vec{p}_\nu}{E_\nu} + D \frac{\vec{p}_e \times \vec{p}_\nu}{E_e E_\nu} \right) \right] \quad (1.66)$$

where  $E_e$ ,  $E_\nu$ ,  $\vec{p}_e$ , and  $\vec{p}_\nu$  are the electron and neutrino energies and momenta respectively.  $F(E_e)$  is the electron energy spectrum. The energies and momenta may be correlated by the parity-violating coefficients  $a$ ,  $b$ ,  $A$ , and  $B$ , as well as the time invariance violating  $D$ . The correlations can be expressed in terms of  $\lambda$ , and the T-odd phase angle,  $\phi$ , between  $g_a$ , and  $g_v$ :

$$\begin{aligned} \lambda &= \left| \frac{g_a}{g_v} \right| e^{i\phi} \\ a &= \frac{1 - |\lambda|^2}{1 + 3|\lambda|^2} \\ A &= -2 \frac{|\lambda|^2 + |\lambda| \cos \phi}{1 + 3|\lambda|^2} \\ B &= 2 \frac{|\lambda|^2 - |\lambda| \cos \phi}{1 + 3|\lambda|^2} \\ D &= 2 \frac{|\lambda| \sin \phi}{1 + 3|\lambda|^2} \end{aligned} \quad (1.67)$$

Thus a measurement of the correlations  $a$ ,  $A$ , or  $B$  will provide  $\lambda$ . The  $B$  correlation is the least sensitive to  $\lambda$ , and while the  $a$  correlation is the most sensitive, it is a more challenging experiment than measuring  $A$ . This is because it requires a measurement of the energy and momentum of the neutrino that can only be obtained indirectly. Currently the best limits on  $\lambda = -1.2694 \pm 0.0028$  are set by measurements of the  $A$  correlation[18]. The  $D$  correlation coefficient depends on the phase angle between the vector and axial-vector couplings, which is nearly  $\pi$ -radians. The measured value of  $D$ [18] is consistent with zero,  $-4 \pm 6 \times 10^{-4}$ .

An expression for the neutron lifetime can be obtained from Eqn. (1.66) by averaging over the neutron spin and integrating over the electron energy,

$$\tau_n^{-1} = \frac{m_e^5 c^4}{2\pi^3 \hbar^7} G_F^2 |V_{ud}|^2 (1 + \lambda^2) f_{RC}. \quad (1.68)$$

Here the value  $f_{RC}$  contains the Fermi integral,  $f$ , calculated from the Fermi function as a part of the integration of  $F(E_e)$ , as well as the calculated radiative corrections[29]. With a measurement of both the neutron lifetime and one neutron decay correlation, one can extract  $V_{ud}$ , the first element of the CKM matrix. Including the most recent calculation of

Table 1.2: Fermi and Gamow-Teller decay mode transitions.

Fermi			Gamow-Teller		
$\uparrow$	$\rightarrow$	$\uparrow +  S = 0, m = 0\rangle$	$\uparrow$	$\rightarrow$	$\left\{ \begin{array}{l} \uparrow \\ \downarrow \end{array} \right. +  S = 1, m = 0\rangle$
$n$		$p + e, \nu_e$	$n$		$p + e, \nu_e$

the theoretical radiative corrections[30], this may be expressed

$$|V_{ud}|^2 = \frac{(4908.7 \pm 1.9)s}{\tau_n(1 + \lambda^2)}. \quad (1.69)$$

This is an important consistency check on the theory because a full theory the CKM matrix should be unitary,

$$V_{ud}^2 + V_{us}^2 + V_{ub}^2 = 1. \quad (1.70)$$

If this condition is not met it could be suggestive of additional generations of quarks which have not been observed.

In principle, one could measure the vector coupling, and therefore  $V_{ud} = g_V/G_F$ , directly in nuclear beta-decay. Since the total angular momentum must be conserved during a beta transition one can classify allowed beta decays in terms of their final state spins as shown in Table 1.2. When the electron and anti-neutrino form a spin singlet with total spin zero, the operator that transforms the neutron spin to the proton spin is the unit operator and the hadronic current is purely the vector form. This type of transition is known as a Fermi transition. When the electron and anti-neutrino form a spin triplet with total spin 1, the spin of the neutron transforms by the Pauli matrices, where  $\Delta J = 0, \pm 1$ . Decays following this set of selection rules are called Gamow-Teller transitions.

A special case of superallowed Fermi decays are defined as transitions between isospin  $T = 1$  analog states where both initial and final states have  $J^\pi = 0^+ \rightarrow 0^+$ . Here the matrix element for the transition is purely Fermi type. Thus due to CVC, this is a system where the measured lifetimes are directly proportional to the vector coupling,

$$\mathcal{F}t = ft(1 + \delta'_R)(1 + \delta_{NS} - \delta_C) = \frac{K}{2g_v^2(1 + \Delta_R^V)}, \quad (1.71)$$

where  $t$  is the partial half-life and is directly related to half-life of the decay,  $K$  contains the physical constants that are known to a high degree of precision, and  $\Delta_R^V$  is the transition independent part of the radiative corrections. The Fermi integral,  $f$ , is a dimensionless function that contains Coulomb and other charge dependent effects on the decay rate. Combining this with the half-life gives an expression, the  $ft$  value, that is only dependent on the nuclear matrix elements[29, 31]. Thus, the  $ft$  values provide a comparison of decay probabilities between different nuclei. Since  $f$  is a function that is computed as a double integral over both the electron energy and the nuclear volume it is weakly dependent on the nuclear model chosen. By removing all transition dependency from the function, one can specify a “corrected”  $ft$ , or  $\mathcal{F}t$ . Specifically the theoretical corrections include,  $\delta_C$ , an isospin-symmetry breaking correction,  $\delta'_R$ , the transition dependent part of the radiative corrections, and  $\delta_{NS}$ , a correction due to nuclear structure. After the corrections, the constancy of the  $\mathcal{F}t$  values across all such transitions is a test of the CVC hypothesis. A summary of all measurements of superallowed  $0^+ \rightarrow 0^+$  transitions to date is shown in Figure 1.3. These data[32] provide the most precise values of  $V_{ud}$ . However, due to the perturbing affects of the nuclear forces, the value of  $V_{ud}$  extracted from superallowed  $0^+ \rightarrow 0^+$  relies more on theoretical corrections than do the value extracted from neutron beta-decay. The value of  $V_{ud}$  extracted from neutron beta decay is however limited experimentally.

One of the most basic semi-leptonic decays can be found in pion beta decay. The rare pion decay branch  $\pi^+ \rightarrow \pi^0 + e^+ + \nu_e$  is a pure vector transition between two spin-zero members of an isospin triplet, and is therefore analogous to the superallowed nuclear beta-decays. Although the number of corrections required to extract a value of  $V_{ud}$  is less than either in nuclear beta-decays or in neutron beta-decay, precision measurements in this system are limited by the size of the branching ratio[33],  $R_{\pi\beta} = 1.036 \pm 0.009 \times 10^{-8}$ . This most precise measurement of the branching ratio made by the PIBETA collaboration sets the most precise experimental limits on  $V_{ud} = 0.9728(30)$  in this system[18].

## 1.4 Big Bang Nucleosynthesis

As previously shown, a precision measurement of the neutron lifetime is sensitive to additional generations of quarks in verifying CKM unitarity. The neutron lifetime is also a dominant uncertainty in the theoretical predictions of helium abundance in the early universe in Big Bang Nucleosynthesis (BBN) models. Additionally, it plays a role in

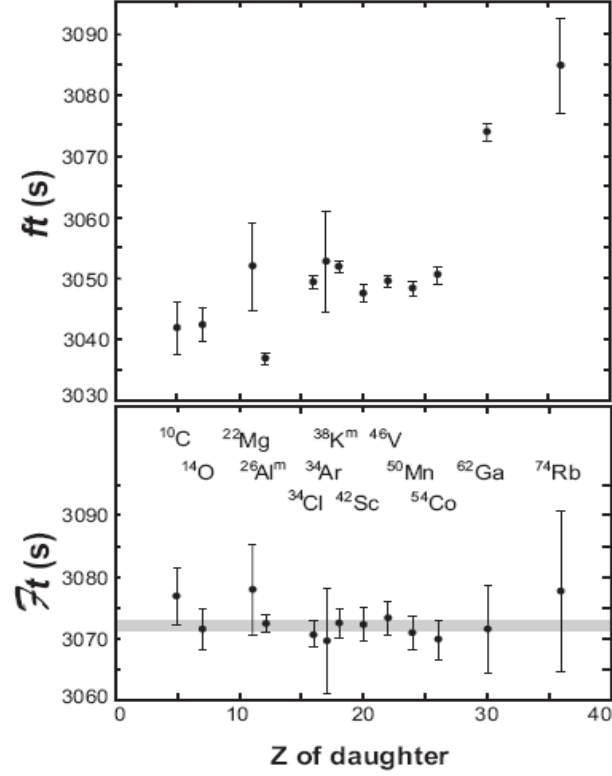


Figure 1.3: Uncorrected  $ft$  values, of 20 superallowed  $0^+ \rightarrow 0^+$  nuclear  $\beta$ -decays (top), and the corresponding “corrected” values[32] (bottom). The grey band represents one standard deviation on the average  $\overline{Ft}$ .

constraining the number of neutrino flavors.

The big bang inflationary model is based on evidence that the universe is expanding,  $\dot{R} \geq 0$ , and that the size of the universe,  $R$ , can be extrapolated back in time to a radius of zero. This singularity is unaccountable for in general relativity and is generally taken as an initial condition for the universe. At this time the radiation and matter is in thermal equilibrium at a temperature  $T \propto R^{-1}$ . What makes the universe unique is the departures from thermal equilibrium that result in its character today. The following sections are meant to highlight the role of the neutron lifetime in the models of the early universe. For a more complete discussion of the big bang inflationary model see Ref. [34].

The number densities of a nuclear species,  $n_A$ , in the expanding universe decrease

as  $R^{-3}$ . It is thus useful to define the mass fraction,

$$X_A \equiv n_A A / n_N, \quad (1.72)$$

of a particular nuclear species  $A$  with density  $n_A$ . The total nucleon density,  $n_N = n_n + n_p + \sum_i (n_A A)_i$ , is used for normalization. In the early universe, the particle species remain in a Boltzmann distribution through interactions that occur at a rate,  $\Gamma = n\sigma|v|$ , where  $\sigma$  is the cross section for the interaction and  $|v|$  the magnitude of the relative velocity. When the rate of interactions become less than the rate of expansion of the universe,  $H$ , the species involved decouple from thermal equilibrium. If the species is stable on the scale of the age of the universe, its abundance remains in this equilibrium distribution at the so-called ‘freeze-out’ temperature. For example neutrinos decouple when neutral current weak interactions responsible for,  $\bar{\nu}\nu \leftrightarrow e^+e^-$ ,  $\nu e \leftrightarrow \bar{\nu}e$ , and etc. occur at a rate less than the Hubble expansion rate,  $T \simeq 1$  MeV. This decoupling created a population of relic neutrinos with a thermal distribution around  $T_\nu = 1.96$  K.

#### 1.4.1 Primordial Nucleosynthesis

As the universe expanded and its temperature cooled to scales comparable to the binding energy of light nuclei, formation of nuclei from baryonic matter began to dominate. The epoch is marked with a freeze-out of the neutron to proton ratio,  $n/p$ , and a subsequent series of reactions that formed stable nuclei from the protons and unstable neutrons further preserving the decoupled species.

Although some binding energies of light nuclei are as high as 8 MeV, conditions were not generally favorable for nucleosynthesis until  $\sim 1$  MeV due to the high entropy of the universe. At  $t \sim 1$  s the universe was radiation dominated and the baryons that had condensed from the quark gluon plasma (QGP) earlier at  $T \sim 300 - 400$  GeV or  $t \sim 10^{-6}$  s, remained in thermal equilibrium

$$n/p = e^{-(m_n - m_p)c^2/k_B T}. \quad (1.73)$$

The weak reactions  $n + \nu_e \leftrightarrow p + e^-$  and  $p + \bar{\nu}_e \leftrightarrow n + e^+$  maintained this equilibrium prior to freeze-out. The equilibrium was maintained until the weak interactions rate,

$$\Gamma(n \leftrightarrow p) \approx \left(\frac{7}{60}\pi\right) (1 + 3\lambda^2) G_F^2 T^5, \quad (1.74)$$

became smaller than the Hubble expansion rate,

$$H \approx \sqrt{\frac{8\pi G_N}{3} \rho_\gamma}, \quad (1.75)$$

thus defining what is known as the freeze-out time[35]. Here the energy density of relativistic bosons is  $\rho_\gamma = \left(\frac{\pi^2}{30}\right) g_* T^4$ , and  $g_*$  is the total number of massless degrees of freedom. The freeze-out time corresponds to a temperature of  $T_{fr} \simeq (g_* G_N / G_F^4)^{\frac{1}{6}} \approx 0.8$  MeV. Using Eqn. (1.73), the ratio of neutrons to protons at freeze-out was  $n/p \approx 1/6$ .

Following this baryon freeze-out, there was a period from  $T \simeq 0.8$  MeV to  $T \simeq 0.3$  MeV, or  $t \sim 1 - 60$  s, when the ratio  $n/p$  changed primarily as a result of neutron beta-decay. At  $T \sim 0.3$  MeV, when nucleosynthesis reactions began, the ratio was reduced to  $n/p \sim 1/7$ .

It is during this period that the temperature of the universe became less than the electron mass. At this point,  $e^+e^-$  pair production ceased and most electrons and positrons annihilated, depositing their energy into the photon population. About one in  $10^{10}$  leptons remained.

Once the temperature of the universe reached  $T \sim 0.3$  MeV or  $t \sim 1$  min, a rapid series of reactions occurred converting the majority of the neutrons into  ${}^4\text{He}$ , the most tightly bound light nuclear species. It is straightforward to estimate the mass fraction of  ${}^4\text{He}$ , typically denoted as  $Y_p$ , if we assume all neutrons were converted:

$$Y_p \equiv X_4 \simeq \frac{4n_n}{n_N} = \frac{4(n_n/2)}{n_n + n_p} = \frac{2(n/p)}{1 + n/p}. \quad (1.76)$$

Taking  $n/p \approx 1/7$  at the time of production yields an estimate of  $Y_p \approx 0.25$ . This assumption is quite good to first order, however it neglects the physics of the reactions that were involved. Considering all reactions that could result in the production of  ${}^4\text{He}$  will allow for non-zero equilibrium values for the abundances of other BBN reaction elements.

### 1.4.2 Nuclear Statistical Equilibrium

Though their mass fractions are orders of magnitude less than those of helium and hydrogen, the abundances of the light elements,  $Z < 7$ , can also be accurately calculated. The equilibrium values are related to the binding energies of the nuclei,  $B_A$ , the baryon-to-photon ratio,  $\eta \equiv n_N/n_\gamma$ , and the temperature. The small value of the baryon-to-photon ratio,  $\eta \ll 1$ , is an expression of the high entropy of the universe and is an important factor

in the calculation of the nuclear statistical equilibrium (NSE) values of the light element mass fractions.

The NSE abundances are derived from the kinetic equilibrium of a very non-relativistic population of nuclear species[34],

$$n_A = g_A \left( \frac{m_A T}{2\pi} \right)^{3/2} \exp \left( \frac{\mu_A - m_A}{T} \right), \quad (1.77)$$

where  $g_A$  are the number of internal degrees of freedom for nuclear species  $A$  and charge  $Z$ . The chemical potential of the species can be expanded to the chemical potentials of the constituent neutrons and protons,

$$\mu_A = Z\mu_p + (A - Z)\mu_n. \quad (1.78)$$

Eqn. (1.77) can then be expressed in terms of the number densities of neutrons and protons,  $n_{n,p} = g_A (m_{n,p} T / 2\pi)^{3/2} \exp[\mu_{n,p} - m_{n,p}/T]$ , and the binding energy of the nuclear species,  $B_A \equiv Zm_p + (A - Z)m_n - m_A$ :

$$n_A = g_A A^{3/2} 2^{-A} \left( \frac{2\pi}{m_N T} \right)^{3(A-1)/2} n_p^Z n_n^{A-Z} e^{(B_A/T)}. \quad (1.79)$$

The mass fraction is calculated by substituting Eqn. (1.79) into Eqn. (1.72). A set of equations for a complete system must obey  $\sum_i X_i = 1$ . The mass fractions are therefore a coupled system since the abundance for each depends on the density of daughters available and on the reaction rates that produce them. Several Monte Carlo codes are publicly available[36] that can be used to calculate the time evolution of the NSE abundances for 26 nuclides from  $n$  to  $^{16}\text{O}$  using 88 reactions. Figure 1.4 provides an example of the evolution of 5 species of interest  $n/p$ ,  $D/H$ ,  $^3\text{He}/H$ ,  $^4\text{He}/H$  and  $^7\text{Li}/H$ .

The entropy,  $S$ , of an expanding universe must be conserved. It is useful to define the entropy density  $s \equiv S/V$ , where a number of species in a co-moving volume is then equivalent to the number density divided by the entropy density,  $N \equiv n/s$ . Thus, as long as any baryon non-conserving process occurs slowly, the quantity  $n_B/s$  is also conserved. While the number density of photons is proportional to the entropy density of the universe,  $n_\gamma = s/g_*$ , the value of  $\eta = n_B/n_\gamma$ , is not necessarily constant. This is because the number of effectively massless degrees of freedom, or relativistic particles  $g_*$ , is not constant but decreases as the particles become non-relativistic and deposit their energy into the photon bath. Since the annihilation of  $e^+e^-$ , the number of relativistic particles has to first order

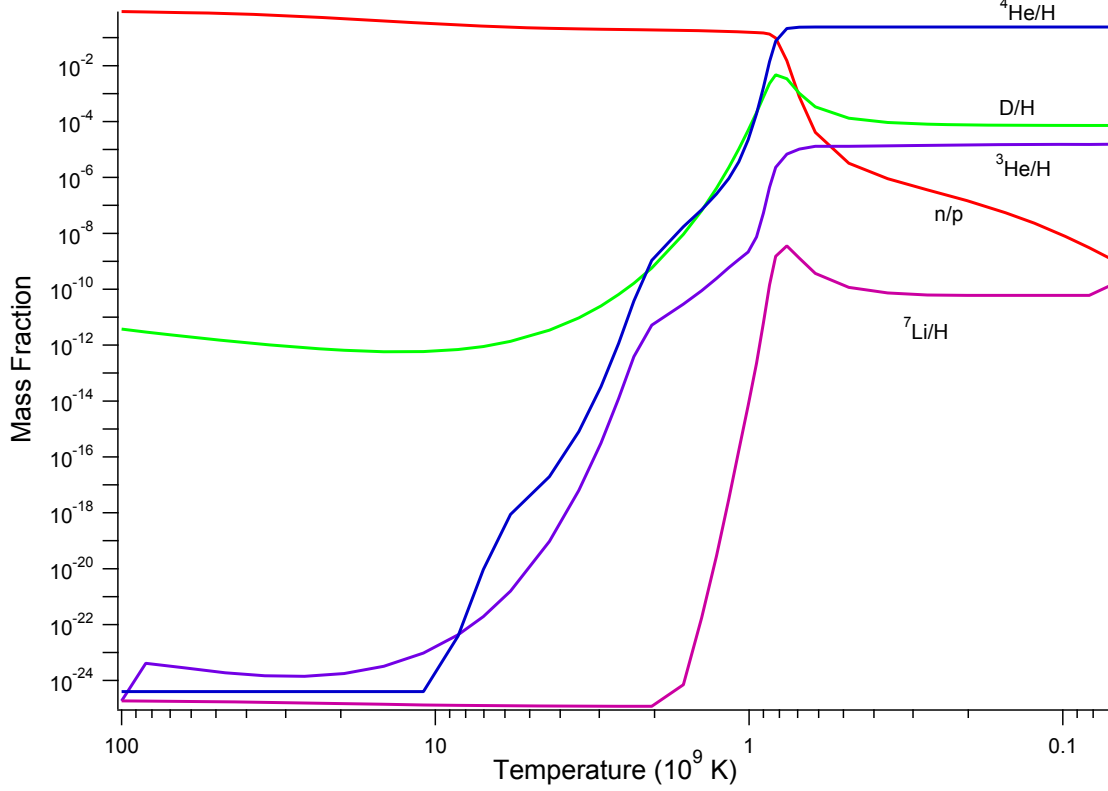


Figure 1.4: The time evolution of the NSE abundances of the nuclides of interest. Calculated using publicly available Monte Carlo code[36, 37].

remained the same and the photon density and entropy are thus directly proportional,  $n_\gamma \simeq s/7.04$ . Therefore,

$$\eta \simeq 7n_N/s \simeq \frac{7(1.13 \times 10^{-5}(\Omega_B h^2) \text{ cm}^{-3})}{2970 \text{ cm}^{-3}} \simeq 2.68 \times 10^{-8}(\Omega_B h^2). \quad (1.80)$$

It is possible to provide experimental constraints on the value of  $\eta$  by comparing the predictions for the BBN light element abundances as a function of  $\eta$  to observational data[18]. Both the theoretical calculation and experimental constraints are shown in Figure 1.5, where the calculation is represented by bands with functional dependence on  $\eta$ , and the observed abundances are shown in boxes ( $\pm 2\sigma$  - small boxes statistical only, larger boxes statistical and systematic). Also shown in this figure are vertical bands that represent constraints from the cosmic microwave background (CMB) taken using the Wilkinson Microwave Anisotropy Probe (WMAP) and the BBN concordance between the calculation and observations. The width of the bands for the calculations represent the uncertainty in

the calculation that are largely due to the uncertainty in the measurement of the neutron lifetime,  $\tau_n = 885.7 \pm 0.8$  s. For example, a  $\pm 0.16\%$  uncertainty in the BBN calculation of  $Y_p$  can be derived from a  $\pm 2$  s uncertainty in the neutron lifetime.

### 1.4.3 Limiting the Standard Model

The Standard Model includes  $N_\nu = 3$  massless neutrinos. It has recently been shown experimentally that an extension must be added to the Standard Model to account for a small neutrino mass and a right handed partner as the measured flavor oscillation between neutrino species requires (see Eqn. (1.49)). One proposed remedy is the addition

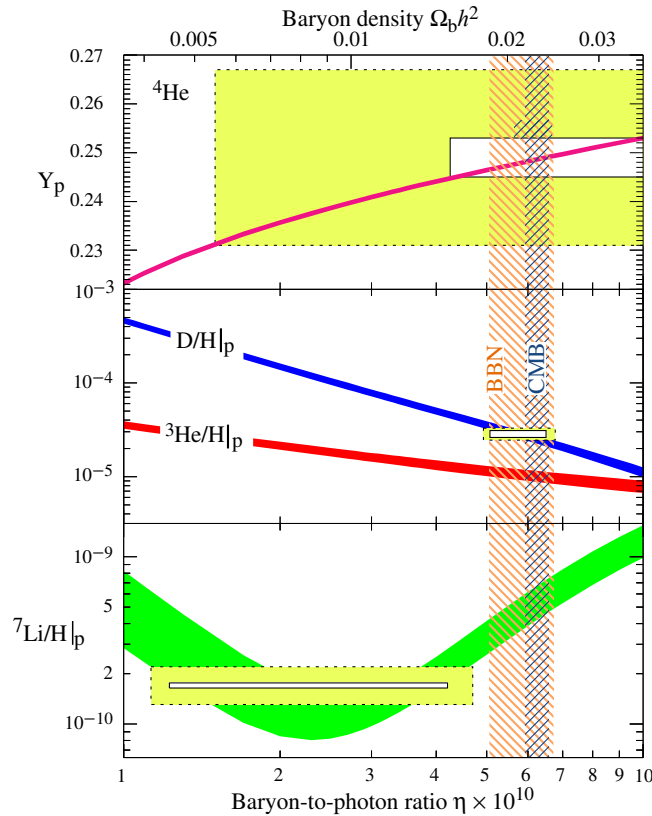


Figure 1.5: Calculation of light element abundances as a function of baryon-photon ratio,  $\eta$ , bands represent the 95% CL. The observed values are shown in boxes (smaller boxes:  $\pm 2\sigma$  statistical; larger boxes:  $\pm 2\sigma$  statistical and systematic). Vertical bands represent the CMB measure of the cosmic baryon density, as well as BBN agreement with data, both at a 95% CL[18].

of a species of sterile neutrinos that does not participate in the weak interaction, but has a small mass. The addition of such a species will not affect the established  $N_\nu = 2.92 \pm 0.05$  [18] from the invisible  $Z$  width measured in  $e^-e^+$  colliders that represents a number of  $SU(2)_L$  doublet neutrinos.

Additional neutrino species are not easily detectable through conventional methods of measuring weakly interacting species. However, if they maintain a coupling to the universe (i.e. via gravitational interactions, etc.) during the epoch of the  $n/p$  decoupling, they will boost the relativistic energy density and therefore the expansion rate of the universe. This will extend the freeze-out to occur at a lower temperature, resulting in an increase in the abundance of  ${}^4\text{He}$  in the early universe. Using known abundances, a bound can therefore be set on the number of neutrino species[38][39][40],

$$N_\nu = 3 + f_{B,F} \sum_i \frac{g_i}{2} \left( \frac{T_i}{T_\nu} \right)^4. \quad (1.81)$$

Here  $g_i$  are the number of weakly interacting helicity states,  $f_B = 8/7$  (bosons) and  $f_F = 1$  (fermions). The situation is further complicated by the matter-enhanced mixings of the sterile neutrino with the left-handed doublets and thereby equilibrating  $T_i/T_\nu \simeq 1$ . Additionally such mixings can produce  $\nu_e, \bar{\nu}_e$  asymmetries that modify the interconversion of neutrons and protons, further modifying the  ${}^4\text{He}$  abundance. Using a  $\chi^2$  fit to minimize uncertainties from both the BBN calculated and measured values of the abundances  $Y_{4,2,7}$  a limit of  $2 < N_\nu < 4$  can be set[39].

## 1.5 Summary

Theories included in the Standard Model of particle physics have been very successful. They have accurately described the weak interactions in terms of an  $SU(2) \otimes U(1)$  gauge theory. This includes a quantitative description of  $\beta$ -decay, and can thus be further used as a probe for additions to the Standard model such as new quark generations.

Similarly, the Big Bang Nucleosynthesis model is a highly successful model of the early universe. It accurately predicts abundances of light nuclei that span eight orders of magnitude. A more precise measurement of the neutron lifetime may allow the theory to provide even more predictive potential in areas such as the number of neutrino flavors.

The next chapter follows with a discussion of neutron lifetime measurements, an analysis of the techniques, and the conclusions one may draw from these.

## Chapter 2

# Neutron Lifetime Measurement Techniques

### 2.1 Neutron Sources

The lifetime of the neutron is short on the scale of the life of a typical observer, but long on the scale of nuclear processes. Therefore, there are no natural sources of free neutrons available with a sufficient density such that the number of decays are statistically significant for studies. The majority of neutrons in the universe are bound within nuclei, and thus to create a source one must liberate them from the nuclei. Two types of laboratory neutron sources commonly used for research are reactors and spallation sources. Through fission processes, reactors can provide useful quantities of neutrons for study. Secondly, when high energy particles are incident on heavy nuclei, the nuclei will fission, and one of the fragmentation products are neutrons.

Just as we classify the different types of electromagnetic radiation by wavelength or energy, so too can one classify neutron radiation. There are no distinct boundaries between the classifications, rather there are rough guidelines highlighting the boundaries between the classes of neutron energies. Neutrons freed from nuclei via fission processes are known as fast neutrons. These are neutrons with energies of  $\sim 1$  MeV, corresponding to velocities of 14,000 km/s.

Neutron sources are typically surrounded by materials that moderate the neutrons to lower energies through successive elastic and inelastic collisions. Neutrons exiting the

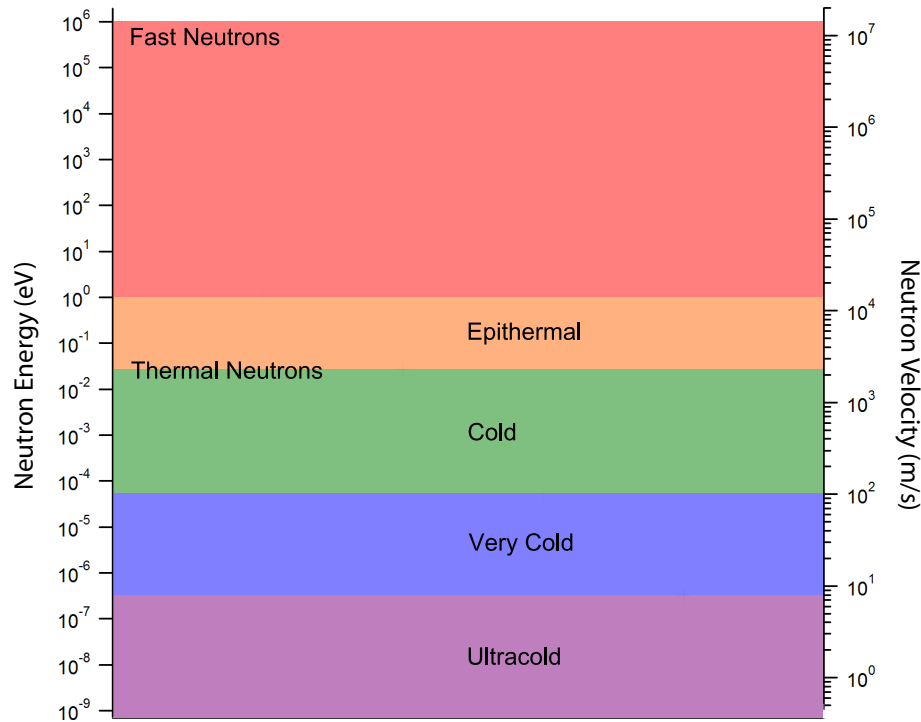


Figure 2.1: Typical neutron energies span many orders of magnitude. As described in Chapter 3, neutrons entering the experimental cell have a peak energy near 1 meV and are subsequently downscattered in liquid helium to energies below 240 neV.

moderator are said to have been thermalized when they have reached equilibrium with the moderator. For room temperature moderators surrounding the source this corresponds to  $k_B \cdot 300$  K, or 25.85 meV, or  $v_{th} = 2224$  m/s, where  $k_B$  is the Boltzmann constant. Those neutrons not fully thermalized by the room temperature moderator are known as epithermal neutrons.

One can use additional cryogenic moderators to further lower the neutron energy. ‘Cold’ neutrons are those with energies in the range of 25 - 0.05 meV, ‘very cold’ neutrons have energies in the range of 25 meV - 300 neV, and ‘ultracold’ have energies below 300 neV. Figure 2.1 depicts the general energy classifications for neutrons.

## 2.2 Properties of Ultracold Neutrons

At very low energies the neutron's wavelength is long enough that it samples many nuclei when it approaches a material surface. The neutron wavefunction can be represented by an incident wave and the sum of spherical scattered waves from the individual nuclei. As a consequence of the difference in scales between the neutron wavelength and the density of nuclear scatterers, the strong nuclear force may be represented as an effective nuclear pseudo-potential[41],

$$V = \frac{2\pi\hbar^2}{m_n} \sum_i N_i a_i. \quad (2.1)$$

A linear combination of the nuclear number density,  $N_i$ , and the coherent neutron scattering length,  $a_i$ , of the full stoichiometry of the material, where  $m_n$  is the neutron mass.

Since  $V$  is typically the same order of magnitude as cold neutrons, they may be reflected from surfaces at angles less than the critical angle (see Eqn. (1.2)). Similar to light transport through fiber optics, neutron scattering facilities utilize this property transporting neutrons long distances via neutron guides.

When neutron energies are sufficiently low such that their energies are equal to or lower than the material wall potential, total internal reflection occurs at normal incidence. Such neutrons are classified as ultracold (UCN) with kinetic energies of 300 neV or less. As such, UCN are slow moving particles. They have a maximum velocity of  $\sim 7.6$  m/s and travel on parabolic trajectories. UCN interact with gravity converting kinetic energy to potential energy at the level of 102 neV/m. The neutron is a neutral particle and to first order does not interact with electric fields. However, its small magnetic moment does interact with a magnetic field at the level of 60 neV/T. Therefore, an ultracold neutron is a class of particles that experience magnetic, gravitation, and nuclear forces with comparable strengths.

## 2.3 Neutron Beta-Decay

Although the precision of early measurements of the neutron lifetime have steadily improved with time (see Figure 2.2a.), currently it would seem that the accuracy of the measurements is suffering. In addition to the theoretical motivations presented in the previous chapter for performing a precision measurement of the neutron lifetime, one also requires self-consistency amongst measurements to insure systematic effects are under control.

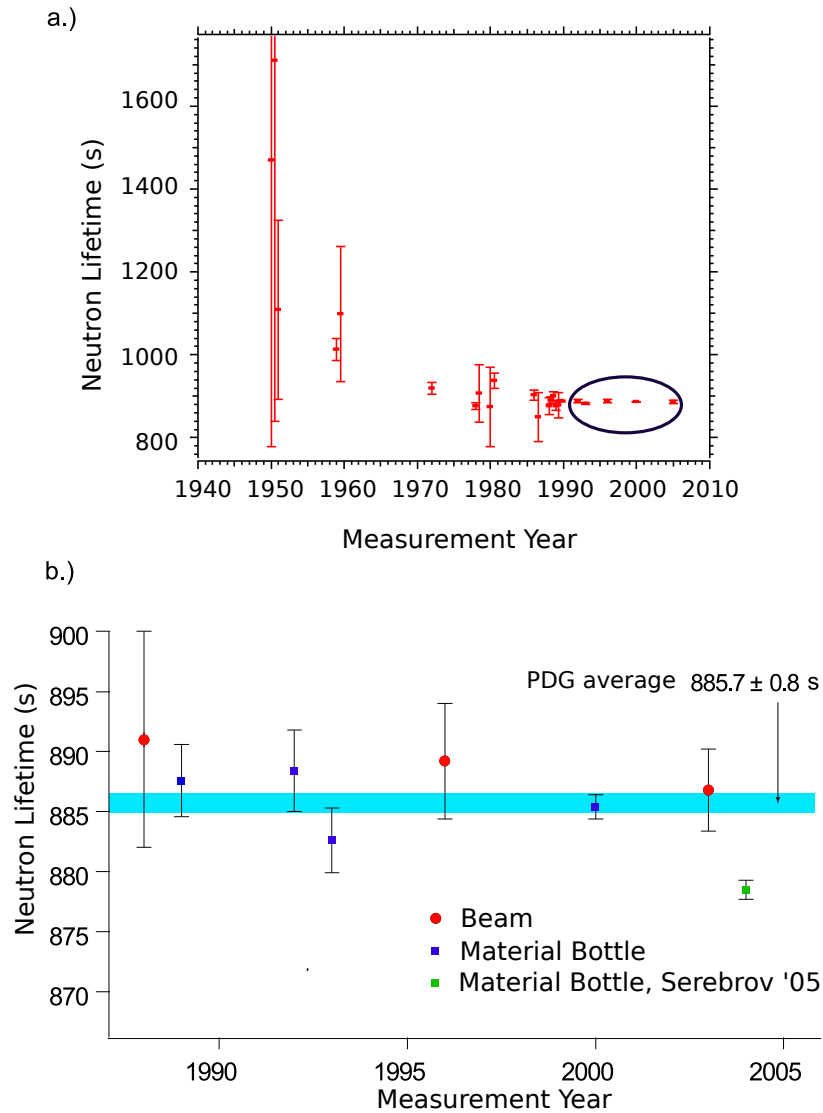


Figure 2.2: a.) A timeline of all neutron lifetime measurements[42], b.) A closer view of the 7 measurements included in the PDG average, as well as a recent measurement by Serebrov *et al.* that was not included in this average[43].

The Particle Data Group (PDG)[18] is responsible for compiling the world average lifetime value. Figure 2.2b. illustrates all statistically significant measurements. The measurement published by Serebrov *et al.* in 2005[44] is not included in this PDG average. While this measurement is similar in precision to the world average, its central value lies 6.5 standard deviations from the central value of the average. Because of this large discrepancy, the PDG argues that it does not make sense to include it in such a statistical average. It

does however reiterate the need for additional measurements with similar precision to solve this discrepancy.

To understand how such a discrepancy effects the unitarity of the CKM matrix, one can create exclusion plots from the differing dependencies on the coupling constants using the most precisely determined decay correlation, the spin-electron correlation  $A$ , and the neutron lifetime. The value of  $A$  provides  $\lambda = g_a/g_v$ , while  $\tau_n^{-1} \propto (g_a^2 + 3g_v^2)$ . This exclusion plot is shown in Figure 2.3.

The PDG values of  $\lambda$  and  $\tau_n$  are consistent, albeit with large error bars, with the more precise determination of  $g_v$  from both measurements of superallowed  $0^+ \rightarrow 0^+$  nuclear beta decays and measurements of  $V_{us}$  and  $V_{ub}$  when combined with the condition that the CKM matrix is unitary. The new  $\tau_n$  measurement [44] deviates from both of these limits. Additionally a new measurement of the  $A$  correlation coefficient by the Perkeo group in Heidelberg also modifies the limits of  $g_v$  away from those of the nuclear  $\beta$ -decays and unitarity requirements[45]. It is interesting to note that the combination of both new values returns the agreement with the  $0^+ \rightarrow 0^+$  CKM unitarity limits.

A global analysis of neutron and nuclear decays further demonstrates the need to quantitatively address the discrepancies. The work of Severijns *et al.*[46] presents an analysis of the current situation in neutron and nuclear  $\beta$ -decay physics by relaxing the  $V - A$  constraints toward the general Hamiltonian for  $\beta$ -decays presented by Jackson *et al.*[28] The authors have computed several fits to all physically relevant data using several models of varying generality.

In the standard  $V - A$  one-parameter fit to  $\lambda$ , Severijns *et al.* computed a  $\chi^2 = 74.08$  for the 25 degrees of freedom resulting in  $\lambda = -1.27293(46)$ . This fit includes the most recent published value of the neutron lifetime[44]. If this value is excluded the  $\chi^2$  for the fit is reduced to 25.86 for 24 degrees of freedom, and the resulting  $\lambda = -1.26992(69)$ . If the  $V - A$  assumption is relaxed to allow for scalar and tensor couplings through a fit to three free parameters,  $C_A/C_V$ ,  $C_S/C_V$ , and  $C_T/C_A$ , the addition of the Serebrov value of the neutron lifetime leads to a non-zero tensor component,  $C_T/C_A = 0.0086(31)$ , albeit with large  $\chi^2 = 82.45$  for 47 degrees of freedom. The parameters  $C_S$  and  $C_T$  are however

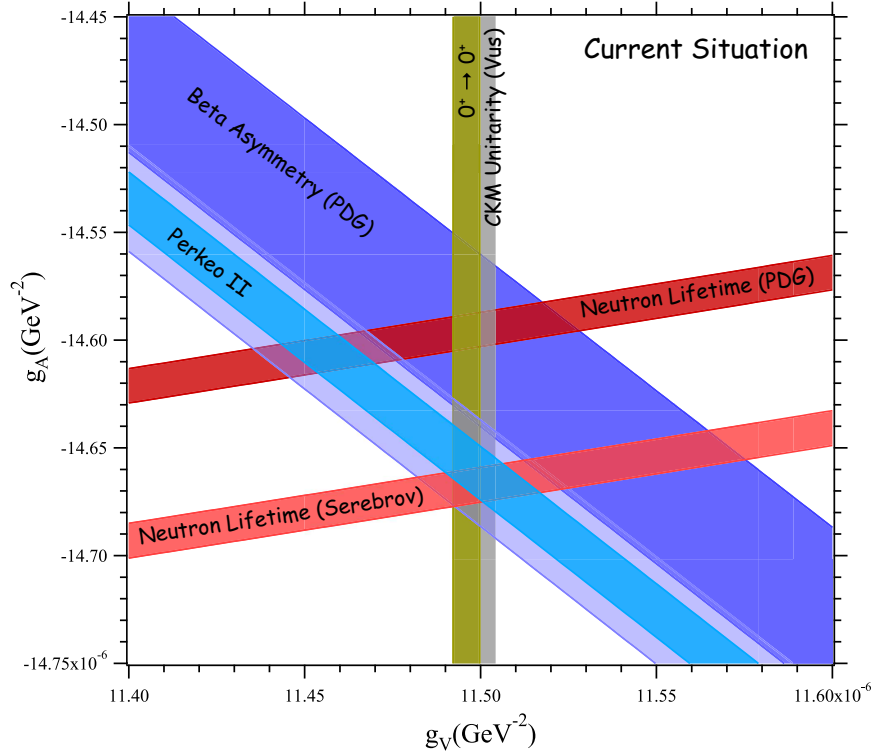


Figure 2.3: The couplings  $g_a$  and  $g_v$  are constrained by measurements of the neutron lifetime and the  $\lambda$  parameter taken from measurements of the spin-electron correlation coefficient,  $A$ .

minimized with the exclusion of the Serebrov result yielding the values:

$$\begin{aligned}
 C_A/C_V &= -1.26994(82), \\
 C_S/C_V &= 0.0013(13), \\
 C_T/C_A &= 0.0036(33),
 \end{aligned} \tag{2.2}$$

with a  $\chi^2 = 40.91$  for 46 degrees of freedom.

Another important observable in the fit to tensor currents is the asymmetry parameter  $A$  in neutron decay. In particular, the aforementioned Perkeo measurement has obtained three mutually consistent values that are higher in absolute value than the results of other measurements, hinting at a possible unknown systematic error in either the older measurements or these newer Perkeo measurements. It is interesting again that in this system as well as an independent fit using only the new data for  $A$ , and  $\tau_n$  yields values of the coupling constants that agree with the Standard Model[47].

Clearly, new precision measurements of both  $A$  and the neutron lifetime using independent setups that have different systematics are needed. The measurements of the neutron lifetime included in the PDG average are of two types, denoted as beam and bottle and therefore may be blinding critical systematics in the analysis. Although each type has different systematics, the precision is currently set by only bottle type measurements.

### 2.3.1 Beam-type Neutron Lifetime Measurements

A lifetime measurement can be performed using a beam of cold neutrons. In such a measurement, the neutron beta-decay rate is measured for neutrons passing through a well defined fiducial volume. From the exponential decay law,  $N = Ce^{-t/\tau}$ , the lifetime is related to the decay rate,  $\frac{dN}{dt} = -N/\tau$ . In this case,  $N$  is the number of neutrons at any given time in the fiducial volume, defined by the cross sectional area of the beam,  $A$ , and a length  $L$ . Using the absolute neutron fluence,  $I(v)$ ,  $N$  can be characterized as,

$$N = \int_0^L dz \int_A da \int dv I(v) \frac{1}{v}, \quad (2.3)$$

where  $v$  is the neutron velocity. The  $1/v$  dependence results from the shorter time spent in the volume by faster neutrons.

The most recent measurement of this type was performed at National Institute of Standards and Technology (NIST)[48]. In this experiment, the decay protons are trapped in a quasi-Penning trap as seen in Figure 2.4 and subsequently counted with an efficiency  $\epsilon_p$ . The measured proton rate is expressed as,

$$\dot{N}_p = \frac{\epsilon_p L}{\tau_n} \int_A da \int dv I(v) \frac{1}{v}. \quad (2.4)$$

Beyond the trap, the neutron beam passes through a thin foil of  ${}^6\text{LiF}$ . Some of the neutrons interact via the reaction  ${}^6\text{Li}(n,t){}^4\text{He}$ , which has a cross section that is proportional

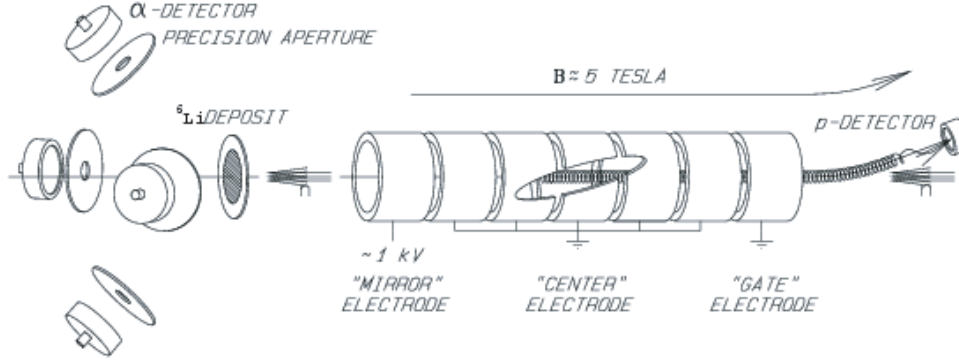


Figure 2.4: Schematic of the NIST neutron lifetime beam measurement[48]. The neutron decay rate in the variable length quasi-Penning trap is extracted by counting protons extracted from the trap. Neutron fluence measurements are made with a “ $1/v$ ” LiF detector by detecting  $\alpha$ 's from the reaction in a well-defined geometry.

to  $1/v$ . The alphas from this reaction are counted using four silicon surface barrier detectors arranged in a well defined geometry. The count rate of alphas can then be related to the neutron fluence. Defining a detection efficiency for neutrons,  $\epsilon_0$  as the alpha count rate for neutrons with an incident velocity,  $v_0 = 2200$  m/s, all other neutron velocities will be detected with an efficiency of  $\epsilon_0 v_0/v$ . Therefore the counting rate in the surface barrier detectors can be expressed as,

$$\dot{N}_\alpha = \epsilon_0 v_0 \int_A da \int dv I(v) \frac{1}{v}. \quad (2.5)$$

The importance of using such a “ $1/v$ ” detector to monitor the neutron fluence is so that its velocity dependence directly cancels the  $1/v$  dependence of the proton rate. Thus the extraction of the lifetime becomes proportional to the ratio of the two count rates,

$$\tau_n = \frac{\dot{N}_\alpha}{\dot{N}_p} \left( \frac{\epsilon_p}{\epsilon_0 v_0} \right) L. \quad (2.6)$$

To measure the lifetime with this technique, each of these values must be measured to the precision of the measurement. The value of  $v_0$  is defined, and a measurement of  $\dot{N}_\alpha$  is relatively precise. Therefore the challenge is to measure  $L/\dot{N}_p$ ,  $\epsilon_p$ , and  $\epsilon_0$  more precisely.

One method used to understand the uncertainty associated with  $L/\dot{N}_p$  is to measure these values using different trap lengths  $L$ . The ratio of alpha to proton rates is linearly dependent on  $L$ , thus a linear fit will improve the uncertainty.

The NIST measurement is limited by the efficiency of the  $1/v$  neutron fluence monitor. Further work is in progress[49] that will improve the calibration of this detector using a high accuracy alpha-gamma neutron fluence monitor. An absolute neutron fluence is measured by counting gammas from the reaction  $n + {}^{10}\text{B} \rightarrow {}^4\text{He} + {}^7\text{Li} + \gamma$  (478 keV) using a calibrated gamma detector. The same  $1/v$  fluence monitors used in the neutron lifetime measurement will then measure the fluence of this well defined beam to improve the uncertainty in the efficiency.

### 2.3.2 Bottle-type Neutron Lifetime Measurements

A second neutron lifetime measurement technique utilizes the properties of UCN described in Section 2.2. Many materials have a Fermi potential large enough to confine a significant number of UCN. With careful consideration of the wall materials, one may construct a material bottle that will store neutrons for times comparable to the neutron lifetime.

The experimental technique for measuring a trap lifetime with such an apparatus is straightforward[50]. The bottle is loaded with a population of UCN,  $N_0$ , that diminishes exponentially with time,  $N(t) = N_0 e^{-t/\tau_{st}}$ . By emptying the remaining neutrons after a varied amount of time,  $t$ , one measures this exponential curve point-by-point with successive measurements.

The storage lifetime,  $\tau_{st}$ , is a combination of both the neutron lifetime and any additional loss mechanisms,

$$\frac{1}{\tau_{st}} = \frac{1}{\tau_n} + \frac{1}{\tau_{loss}}. \quad (2.7)$$

The difficulty in this type of measurement is accurately characterizing all of the loss mechanisms,  $\tau_{loss}$ . There may be many, such as neutron loss due to an imperfect vacuum, neutron loss through gaps in the material surfaces, neutrons having semi-stable orbits that never leave the trap to be counted, and so forth. Typically the largest contribution to  $\tau_{loss}$  arises from interactions of the neutrons with the material wall surfaces.

A common approach to measuring the losses, and thus extracting a neutron lifetime, is to systematically vary the contribution from different loss mechanisms. For example, varying the surface area to volume ratio of the bottle helps to determine the loss due to wall interactions. The population of neutrons,  $N$ , in a container with volume,  $V$ , and neutron

density,  $\rho(E)$ , is

$$N(E) = V\rho(E). \quad (2.8)$$

The loss rate at the container walls is a product of the UCN flux on the walls combined with the neutron loss probability,  $\mu(E)$ ,

$$\frac{dN(E)}{dt} = (1/4)v(E)\rho(E)S\mu(E), \quad (2.9)$$

where  $v$  is the UCN velocity and  $S$  is the surface area of the container. One can parameterize the loss lifetime due to wall interactions as,

$$\frac{1}{\tau_{wl}} = -\frac{dN(E)}{N(E)dt} = \frac{S}{4V}v(E)\mu(E). \quad (2.10)$$

It is then possible to vary the loss contribution due to wall interactions by changing the surface to volume ratio of the storage container. With this method, one can extrapolate to an infinite sized volume (no wall collisions) to remove this contribution to the storage lifetime.

As the uncertainty in such a measurement can be strongly dependent on the length of this extrapolation or the magnitude of the correction applied, much effort has gone into selecting materials with low loss probabilities. The most recent measurements[44, 51] have utilized a coating of fomblin oil that has been shown to have high reflection probabilities for UCN. Additional sources of systematic error may arise from container shapes that affect the wall collision frequency. Also, the details of reflections from rough surfaces play a role. Surface roughness might be macroscopic compared to the wavelength of the neutron, contributing to a potentially larger surface area than expected. It may also be microscopic as compared to the neutron wavelength, which can introduce additional losses due to diffraction and interference effects. For more information regarding the effects of surface roughness on the reflection probability of neutrons, see Section 4.2.1.

### 2.3.3 Neutron Lifetime Measurements Using Magnetic Confinement

One way to address systematic effects present in the previous methods is to utilize a completely different measurement technique. As the neutron has a small magnetic moment, one can construct an inhomogeneous magnetic field geometry taking advantage of the resulting interaction to constrain the neutrons' trajectories as opposed to using material walls. This eliminates the primary systematic effect present in many previous measurements.

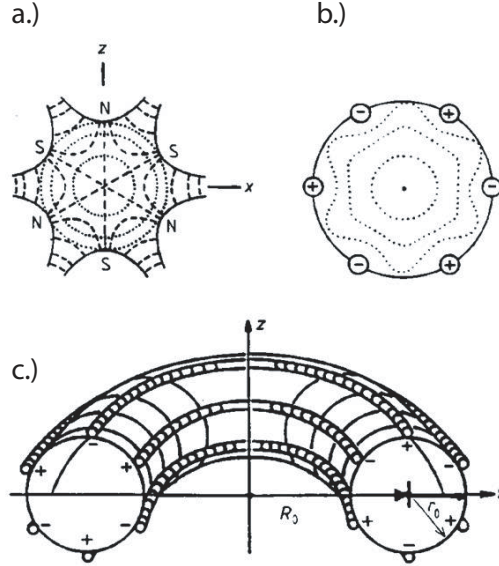


Figure 2.5: Sextupole field lines a.), and potential b.) for six infinite conductors with alternating current sense. A schematic of the toroidal configurations realized in the NESTOR experiment[54] is shown in c.).

The potential energy  $V$  for a neutron with a magnetic moment  $\vec{\mu}_n$  in a magnetic field  $\vec{B}$  is

$$V = -\vec{\mu}_n \cdot \vec{B}. \quad (2.11)$$

As the neutron's magnetic moment is negative,  $\mu_n = -6.02 \times 10^{-8}$  eV/T, it is anti-aligned with its spin direction. A neutron will experience an attractive force to regions of low magnetic field when its spin is aligned parallel with the field. Likewise, it will feel a repulsive force to a field minimum when the spin is anti-parallel with the field direction. Thus one can make use of this interaction to confine neutrons of one spin state to a region of low magnetic field. This technique eliminates interactions of the neutron with any materials that could modify its decay rate.

The first magnetic storage experiment was performed in 1960 used a combination of magnets and gravity to confine neutrons. The field strength was unfortunately too low to trap more than 4 neutrons at one time[52, 53]. Magnetic confinement was also discussed in additional detail by Vladimirkii[53] in 1961.

The first magnetic storage experiment to produce a competitive neutron lifetime

measurement was NEutron STOrage Ring (NESTOR)[54]. This experiment combined techniques of accelerator physics for charged particles in storage rings with magnetic multipole fields and the techniques of atomic and molecular beam physics to guide and focus neutral atoms. To confine a set of particles to a common point of origin one creates a harmonic restoring force. This force should be negative and linearly increasing as a function of distance from the origin,  $\vec{F} = -c\vec{r}$ , yielding a potential that is quadratic in  $r$ . The sextupole term of the multipole field expansion is known to exhibit such a spacial dependence,  $B \propto r^2/B_0$ . Such a field ideally created with six infinite conductors of alternating current sense is shown in Figure 2.5a. However, when realized in the toroidal geometry utilized in the NESTOR experiment and shown in Figure 2.5c, the major component of the beam momentum is confined along the axis of the toroid. Although higher order field coils were used to correct for changes in the field from this geometry, transfer of momentum from the larger beam direction to the smaller transverse components ultimately proved to be the limiting systematic effect in that measurement.

A later experiment[55] used a spherical sextupole field to generate a three dimensional magnetic trap. The neutron energy was dissipated inside the trap using the superthermal production of UCN as is described in the work in this thesis. The problem that limited the performance of this experiment was upscatter of the UCN by phonons in the superfluid helium since the lowest achievable temperature was 1.2 K.

The availability of permanent magnets with high field strengths has allowed scientists to create complex field geometries that make them viable for confining neutrons. The group of V. Ezhov *et al.* constructed the trap shown in Figure 2.6. The vertical cylindrical volume and conical base is constructed from a 20-pole set of permanent magnets. The magnets create a field of 1 T and gradient of 2 T/cm at the walls so that neutrons with energies,  $E < 60$  neV, will not interact with the material walls. Neutrons can however escape from the trap due to spin-flip transitions that arise from inhomogeneities in the field. An external solenoidal field to raise the inhomogeneities above zero fields minimizes the spin-flip probability. The magnet surfaces are also coated with a layer of UCN reflective fomblin oil. This oil serves to reflect neutrons of the untrapped spin state and contain them until they escape through a solenoidal orifice in the bottom of the trap. This field can be energized to allow only wrong spin state neutrons through or de-energized to allow neutrons of both spin states through. The number of the non-trapped spin state neutrons gives the experimenter a handle on the UCN loss mechanism due to spin-flip transitions.

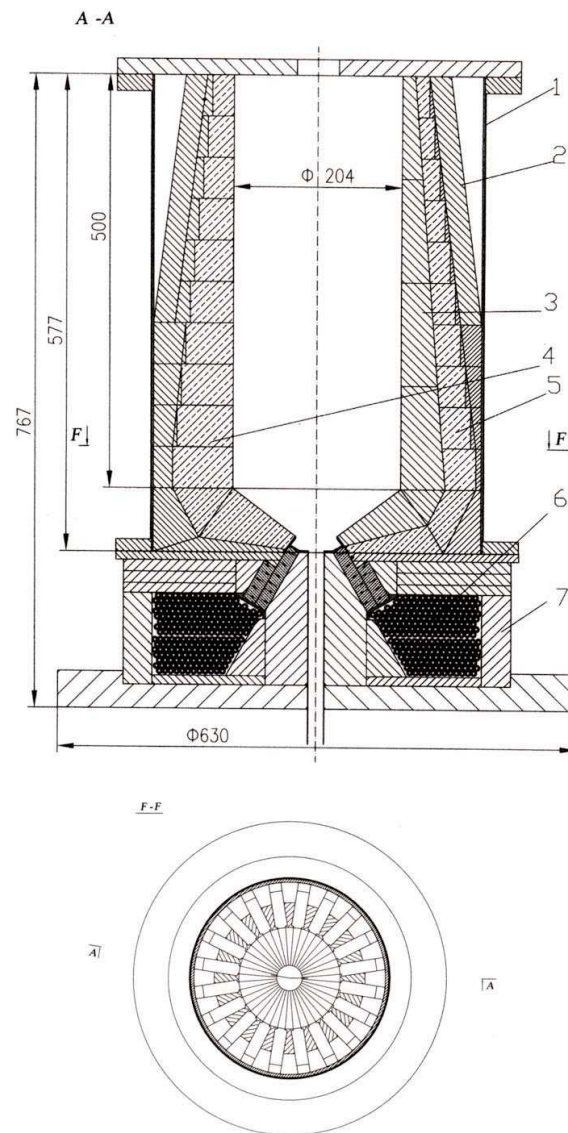


Figure 2.6: Permanent magnet gravitrap[56]. 1-Vacuum chamber, 2-Magnet Yoke, 3-Poles, 4-Primary Magnets, 5-Secondary Magnets, 6-Solenoid, 7-Solenoid Yoke.

One can also obtain the number of trapped neutrons when unpolarized UCN are loaded via a material bottle ‘lift’ from the top of the trap by counting the number of neutrons exiting with the non-trapped spin state during the loading process. As neutrons are loaded, the non-trapped spin state is transported into the detectors from an unpolarized source. There should be equal numbers of the trapped and non-trapped spin state neutrons. At the top of the trap an absorbing material is lowered to a height such that neutrons with energies

greater than  $m_n g h$  will be absorbed. This reduces the likelihood that neutrons will have sufficient energies to penetrate into the material walls. Gravitational confinement is used for the top of the trap.

Care must be taken when analyzing the data from this experiment. If it is assumed that all neutrons of the wrong spin state are reflected from the fomblin surface,  $V = 106$  neV, and collected in the detector, then the upper limit of UCN energies can not be determined for the potential that is set by the field from the permanent magnets. If a neutron with energy,  $E = 60.5$  neV/T, is depolarized, it will gain again this much energy from the field after the spin flip, accelerating it into the fomblin surface covering the magnets. The full height of this trap, 55 cm, therefore could not be utilized, as one is not sure of the reflections of neutrons with energies set higher than the 44 cm height. It may be questionable to rely on the material trapping and collection of UCN from surfaces that are designed for magnetic trapping.

Additionally, the existence of semi-stable neutron trajectories[57] in permanent magnet traps adds significant complication to the analysis. Such neutrons will not necessarily exit the trap when the door is opened. Since these neutrons are not counted in the observation time they introduce additional systematic effects into the extraction of the neutron lifetime. Such systematics can be minimized in superconducting traps since one can ramp the magnetic field in order to change the phase space occupied by all of the neutrons[58]. During a field ramp, the neutrons gain energy and their orbits expand adiabatically. Neutron absorbers can be used outside of the phase space that can be occupied by neutron energies that are fully trapped. Using this technique, the UCN spectrum can be efficiently cleaned. Additional details in the field ramping technique will be discussed in Section 4.2.

## 2.4 Experimental Method

A brief overview of the experimental method used in this thesis work is presented here as an introduction. The following chapters will expand on the various components of this technique in considerably more detail.

This technique utilizes UCNs confined within a three-dimensional magnetic trap. Energy dissipation of the neutrons must occur within the magnetic field minimum due to the conservative nature of the trap. The superthermal technique is utilized whereby

12 K neutrons (0.89 nm) downscatter in superfluid  $^4\text{He}$  to near rest via single phonon emission [59]. The UCN then interact with the magnetic field  $\vec{B}$  via their magnetic moment. The neutron's magnetic moment is anti-aligned with its spin direction. Neutrons with a spin parallel to the magnetic field will seek to minimize potential energy by moving towards low field regions. As the neutron moves in this magnetic field, its spin direction adiabatically follows the direction of the magnetic field. Thus UCN with energies below the trap depth and in the low-field-seeking state are trapped.

The UCN population is thermally detached from the helium bath allowing accumulation of UCN to a density as high as  $P\tau$ , where  $P$  is the superthermal production rate and  $\tau$  is the UCN lifetime in the trap. After a fixed time,  $T_{fill}$ , the 12 K neutron beam is closed off. Neutron decay events are recorded using the scintillation light created as a result of the beta-decay electrons.

When an electron moves through liquid helium, it ionizes helium atoms along its track. These helium ions quickly recombine into metastable  $\text{He}_2^*$  molecules that are in excited states[60]. About 35 % of the initial electron energy goes into the production of extreme ultraviolet (EUV) photons from singlet decays, corresponding to approximately 22 photons/keV of energy deposited. These EUV photons are then frequency down-converted to blue photons using the organic fluor tetraphenyl butadiene (TPB) coated onto a diffuse reflector surrounding the trapping region[61]. The light is transported through light guides to room temperature and detected using two photomultiplier tubes operating in coincidence. The detection method allows one to observe neutron decay events *in situ*, and therefore directly measure the exponential decay in real time.

Using a prototype apparatus, neutron trapping data was previously taken in a number of different experimental configurations, primarily for investigating systematic effects. This data is discussed in detail in Ref. [62] and shown in Figure 2.7. The raw neutron decay curve is shown in blue and exhibits a trap lifetime of  $621.2^{+18.1}_{-17.1}$  (*stat*) s. The low central value suggests that there exist neutron trap loss mechanisms other than beta decay. These losses were shown to be the result of the presence of above threshold neutrons. These neutrons can be removed from the trap by lowering the magnetic field immediately after the loading period, causing their trajectories to expand and thus the neutrons interact with the material walls and become absorbed. As seen in Figure 2.7, data collected using this field-ramping procedure as shown in green exhibits a lifetime consistent with the world average,  $\tau = 831.1^{+58.2}_{-51.0}$  (*stat*) s, albeit with a large statistical uncertainty. In this data, the

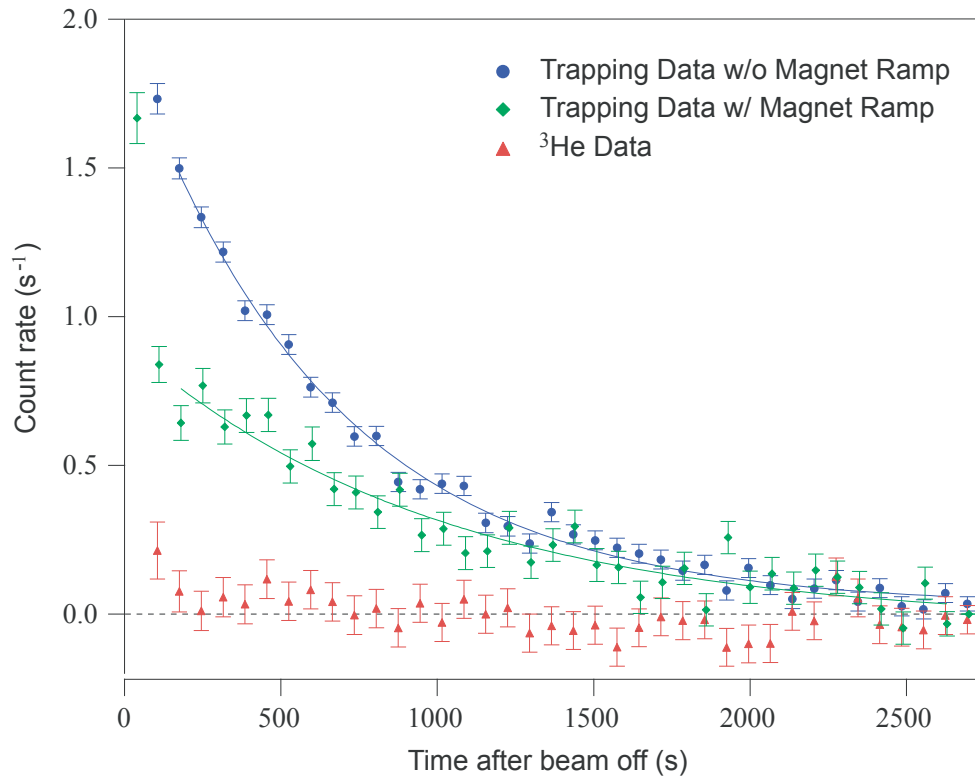


Figure 2.7: Neutron trapping data taken with the Mark II apparatus at NIST. The upper curve represents data taken with no magnetic field ramping as discussed in the text. The middle curve is data taken after the trap field is lowered briefly to remove the above threshold neutrons. The lower curve is data taken with natural isotopic abundance helium, where one would expect no trapped neutrons.

magnetic field was lowered to 30 % of its maximum value immediately after the neutron beam was turned off.

Using these results and our continuing studies of systematic effects, a next generation apparatus has been designed, constructed, tested, and is ready for neutron data collection. The next chapter details the construction of this apparatus.

## Chapter 3

# Apparatus

This chapter describes the development of a new larger magnetic trap for ultracold neutrons. The larger trap also necessitated a new cryostat, as the physical size and weight of the magnets is larger and associated electrical currents are higher than the former cryostat could sustain. Although the design approach taken for each of the elements of this apparatus was drawn from experience gained in the previous setup, this is in most aspects an entirely new apparatus.

### 3.1 Facility

The neutron participates in all forces of nature; electroweak, strong, and gravitational. For this reason, neutron scattering has become a useful diagnostic tool that is highly complimentary to x-ray scattering. The NIST Center for Neutron Research (NCNR) is a 20 MW research reactor facility that sponsors a user program for researchers to use both thermal and cold neutrons for scientific studies. Some particularly unique examples of this research include measurements of both hydrogen storage and transport in fuel cell applications, the characterization of iron based high temperature superconductors, and characterization of ion channels through biological membranes. Additionally, the facility has programs in activation analysis, analytical nuclear chemistry, neutron imaging, and fundamental physics.

The facility currently supports nine thermal neutron beams with a direct view of the central region of a split reactor core. Neutrons exiting the core through these beam tubes are first thermalized by heavy water at room temperature. Additionally, the NCNR has

a liquid hydrogen cold source[63] that thermalizes neutrons to a much lower temperature. Neutrons leave the cold source having an approximately Maxwellian distribution peaking at 2.6 meV, or 30 K. They are transported to an adjacent building through one of seven  $^{58}\text{Ni}$  coated glass guides. Transport away from the reactor provides increased space for scattering instruments as well as significantly reducing the backgrounds in these instruments from prompt-gammas and fast neutrons from the reactor. The high nuclear potential of the nickel coating acts as a potential barrier to the neutrons and those with an angle of incidence less than the critical angle are reflected to the end of the guide with minimal loss. One of the seven cold neutron guides at NCNR, NG-6, is dedicated to fundamental physics experiments. This guide is maintained by the Neutron Interactions and Dosimetry group, a part of the Ionizing Radiation Division of the Physics Laboratory. Unlike the other guide stations that have dedicated instruments for performing measurements on material samples, each fundamental physics experiment is designed specifically for a particular measurement. These measurements are typically precision measurements of the symmetries of nature or properties of the neutron itself.

### 3.1.1 Superthermal Production of UCN

Inelastic scattering of the neutron is a process where the neutron may gain or lose energy. At low neutron energies, this energy transfer is the result of emission or absorption of vibrational states in the medium where the scattering takes place. At low temperatures, the vibrational excitations can be described by quasi-particles such as the phonon or roton. For liquid helium, the energy-momentum dispersion relation that describes the allowed states for phonons and rotons, also known as the Landau curve[64], is well characterized[65, 66]. The free neutron has an energy,  $E = p^2/2m$ , that intersects the Landau curve in only two points, 0 K and 12 K, as shown in Figure 3.1. Therefore the inelastic scattering of a neutron with a single phonon in liquid helium can take place only for neutrons with these energies. The downscatter process occurs through the emission of a 12 K phonon. Furthermore, the population of 12 K phonons that can upscatter a low energy neutron is proportional to the Boltzmann factor  $e^{-12 \text{ K}/T}$ . By lowering the temperature of the helium bath to a few hundred milliKelvin, one can suppress the single phonon upscatter process. Within a bath of low temperature ( $< 500 \text{ mK}$ ) liquid helium, one can build up a population of very low energy neutrons by scattering 12 K (or 0.89 nm) neutrons from the helium, producing

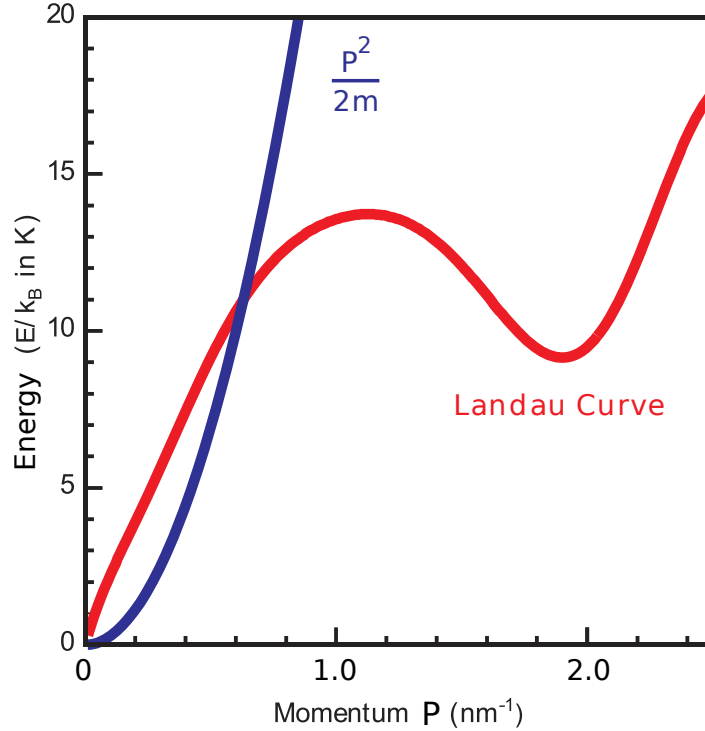


Figure 3.1: The exchange of a single phonon between a free neutron and a bath of superfluid helium can occur at the intersection of their energy-momentum dispersion curves. As seen here, this occurs at just two points,  $E = 0$  K and 12 K.

ultracold neutrons that remain thermally isolated from their surroundings. This process is known as “superthermal” production.

### 3.1.2 0.89 nm Monochromatic Beam

The polychromatic spectrum of neutrons at the end of the NG-6 guide has roughly a Maxwellian wavelength distribution that is peaked near 0.4 nm (see Figure 3.22). Only a small fraction of the beam intensity with a wavelength near 0.89 nm can be used in the production of UCN. Since all neutrons can potentially produce backgrounds, a monochromator is used to Bragg reflect neutrons with a narrow range of wavelengths into the apparatus.

A Stage-2 potassium Graphite Intercalated Compound (GIC) monochromator is used to reflect a beam of 0.89 nm neutrons into the apparatus. Within this graphite crystal, every second plane is separated by a layer of the potassium intercalant. Bragg’s law,  $n\lambda = 2d\sin\theta$ , sets the angle of reflection of the 0.89 nm beam to  $30.6^\circ$  based on the inter-

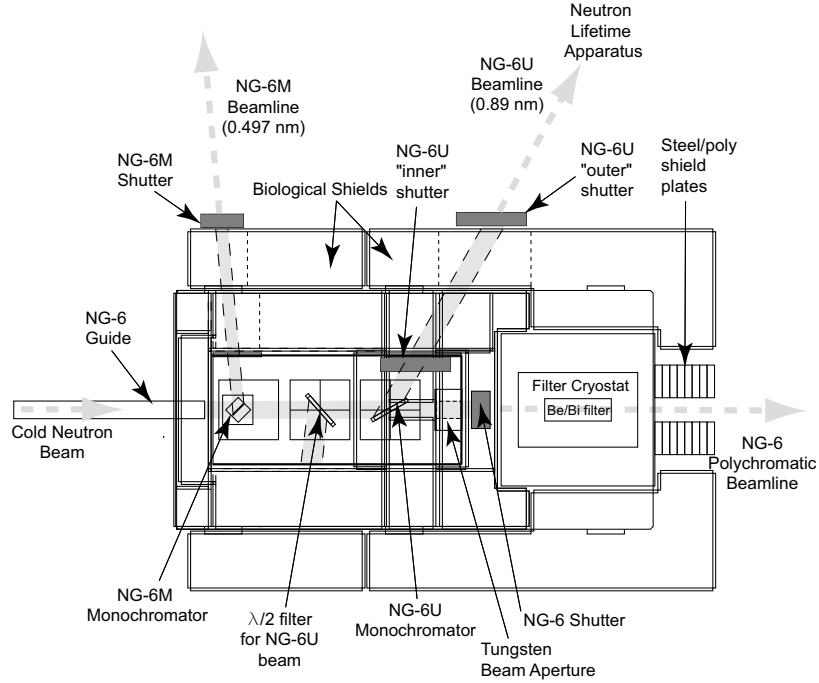


Figure 3.2: Layout of the cold neutron monochromators, beamlines, and shielding at the end of the NG-6 neutron guide. The NG-6U monochromator is a potassium intercalated graphite.

planar spacings of the intercalant,  $d = 0.874$  nm. For more information on the design and production of the monochromator see Ref. [67].

The resultant 0.89 nm neutron beam has additional peaks due to higher order Bragg reflection at  $\lambda/2 = 0.45$  nm and  $\lambda/3 = 0.3$  nm. To reduce the number of neutrons from the  $\lambda/2$  reflection into the apparatus that do not produce UCN, an additional graphite crystal was installed upstream from the GIC monochromator. The crystal is set at an angle of  $45.6^\circ$  to reflect the  $\lambda = 0.45$  nm neutrons into the shielding walls as shown in Figure 3.2. The resulting 0.89 nm beam has a peak wavelength at 0.89 nm with a half width of  $\sim 0.05$  nm. The total monochromatic beam flux was measured using a fission chamber containing a 502 ng deposit of  $^{235}\text{U}$  and determined to be  $\phi_n = 7.1 \times 10^6 \text{ cm}^{-2} \text{ s}^{-1}$ . From this measurement and the neutron time-of-flight spectrum it was determined[62] that the fraction of this flux in the 0.89 nm peak is  $\phi_{0.89 \text{ nm}} = 3.7 \times 10^6 \text{ cm}^{-2} \text{ s}^{-1}$  (see Figure 3.3).

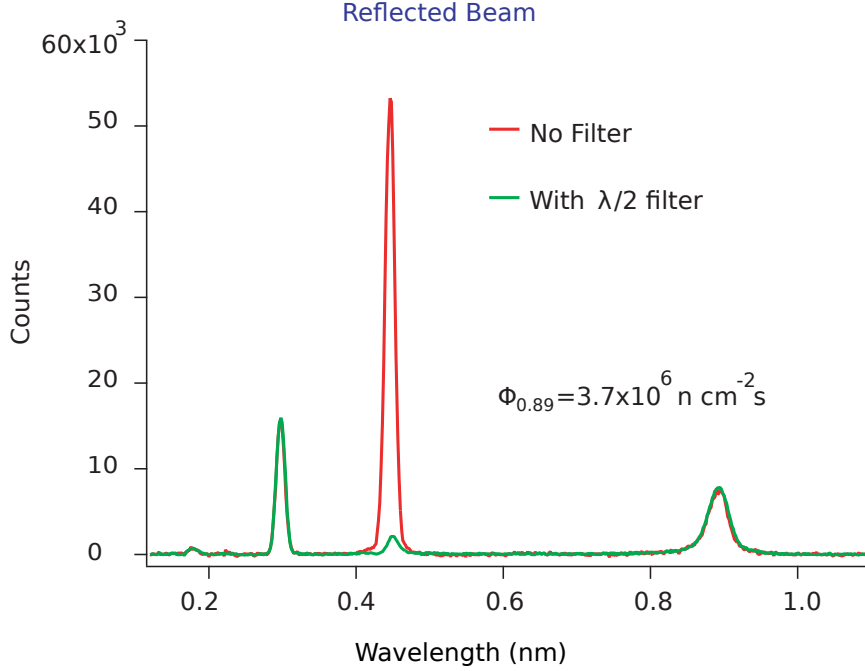


Figure 3.3: Time-of-flight spectra of the neutrons reflected by the GIC monochromator towards the apparatus.

### 3.2 Magnetic Trap

The key component of the upgraded apparatus is the incorporation of a deep Ioffe-type superconducting magnetic trap[68]. As discussed in Section 2.3.3, a neutron may be confined in a three dimensional magnetic field minimum. Such traps are commonly used in atomic physics to trap neutral atoms with magnetic moments, however neutrons have a considerably smaller magnetic moment. The number of trapped UCN scales as  $n \propto \phi_n V B^{3/2}$ , so a large magnetic field minimum with a large volume is desired.

The Ioffe configuration produces field minimum in a cylindrical geometry with no zero-field regions. A quadrupole magnet provides a radial field gradient, while two solenoids provide axial confinement. This state-of-the-art trap is the product of both development within our group and technology borrowed from high-energy accelerator facilities. The magnet described here is the third iteration in this design sequence.

The first two magnetic traps, denoted as Mark I and II, were designed and wound in-house using low current (several hundred amperes) superconducting wire. It was demonstrated using the Mark I trap that UCN could be both produced and magnetically trapped.

Using the somewhat larger Mark II trap, a trap lifetime was extracted, however not at a level sufficient for a high precision measurement of the neutron lifetime.

In addition to their smaller volume and trap depth, the magnetic performance of these traps was limited in two areas. Superconducting magnets may quench, rapidly becoming resistive, when operated at currents higher than the critical current that the wires can sustain. This quenching behavior is normal as one conditions the magnet during initial testing, a process also known as “training.” Upon successive quenching the magnet typically approaches the maximum field set by the critical current of the wire. At low temperatures, the heat capacities of most materials is quite low and very small heat loads can cause significant rises in temperatures. For this reason, small movements of the wires can generate enough heat to bring the wires above the critical temperature causing them to become normally resistive. Training a magnet will allow the wires to settle into a preferred location after which the magnet will generally perform better.

The Mark I and II magnetic traps both showed signs of what is known as excessive training, the behavior of consistently quenching at currents lower than the critical current. This is suggestive of problems in the pre-stressing of the coils or movement of the wires within the coils themselves. Secondly, there were issues related to removing the stored energy from the magnets after a quench. The fraction of the energy stored in the magnets that can be dissipated outside the coils, known as the quench protection efficiency, was shown to be quite low in both the Mark I and II magnets due to the large inductance of the coils. When the quench protection efficiency is low, there is a high risk of permanently damaging the magnet during a quench. For these reasons, a different approach was required in creating magnetic traps with higher trap depths and larger volumes. One must use lower inductance magnets, which in turn require considerably higher currents.

With this in mind, a high current quadrupole magnet originally used for electron beam focusing at the TRISTAN accelerator[69] was obtained on loan from the High Energy Accelerator Research Organization in Japan (KEK). This magnet was designed to operate at 3,405 A (at 4.2 K), providing a radial field gradient of 70 T/m with a maximum field of 4.9 T at the surface of the bore. It has an effective field length of 1.14 m, a bore size of 14 cm, and an outer diameter of 28 cm. It is composed of 16 layers of racetrack shaped coils wound on a circular cylindrical surface in a  $\cos 2\theta$  configuration in 4 sets of 4 concentric layers. Each of the layers is wound from keystoneed cabling with a right handed lay for left handed windings, and with left handed lay for right handed windings. The cable, composed

Table 3.1: Parameters of the new Ioffe-type magnet trap.

	KEK Quadrupole	Solenoid
Form Outer Diameter	28 cm	39.5 cm
Form Inner Diameter	14 cm	28.1 cm
Form Length	145 cm	30.8 cm
Winding Outer Diameter	21.8 cm	36.1 cm
Winding Inner Diameter	14 cm	29.5 cm
Winding Length	114 cm	18.0 cm
Inductance	58 mH	7 H
Operating Current	3400 A	225 A
Critical Current (4.2 K)	4000 A	300 A
Stored Energy	336 kJ	180 kJ

of 27 wires, has a mean thickness of 1.27 mm and a width of 9.09 mm. The strand wires have a diameter of 0.68 mm and are made from roughly 2,200 twisted NbTi filaments embedded in a copper matrix with a copper to superconductor ratio of 1.8. The wires have a strand packing factor of 0.89, meaning that the remaining 11% is expected to be filled with liquid helium for additional stability. After the coils were wound, 30 mm thick 316LN stainless steel collars were stacked around the coils, and a radial pre-stress of  $6.5 \times 10^5$  N was applied. The collars were keyed to keep the pressure on the coils. At its operating current, the KEK quadrupole can produce radial trapping fields with a maximum field of about 3.85 T on the cylindrical boundary of the experimental cell walls.

The pinch solenoids of an Ioffe trap are typically designed to provide the same axial trapping field as the radial field. However, the addition of the solenoids modify the critical field of the quadrupole, so the design of the solenoids must factor in the constraints set by the quadrupole. This leads to an additional design consideration that the maximum field on the quadrupole windings must stay below 7 T.

The Lorentz forces in a solenoid act to compress the wires towards one another and radially outward. Thus a superconducting solenoid for stand-alone operation does not typically exert forces on the form for the windings. The solenoid in an Ioffe trap however experiences additional forces due to the magnetic field of the quadrupole magnet. The result is a force towards the end flanges of the winding form that reverses every 90 degrees around the coil causing an unconstrained wire to twist into a saddle shape. The total force on the flanges of the magnet is roughly  $7.9 \times 10^4$  N. This required a careful design and is described in detail in Ref. [58]. Additionally, support structures were designed to counter

the attractive force between the two solenoids and reduce the likelihood of excessive training of the magnets.

### 3.2.1 Quench Protection

With such large current densities, superconducting magnets store large amounts of energy. A total of 696 kJ is stored in the new magnetic trap when it is fully energized. If this energy is not properly dissipated during a quench, the resistive heating of the wires can cause them to fuse together, or even to vaporize, as the heat of vaporization of copper is 300.3 kJ/mol.

One can protect against such catastrophic failures either actively or passively. In active quench protection, a detection circuit is designed for fast identification of a quench, usually indicated by a voltage change across a superconducting coil. Ideally, the energy is then dumped in an external resistor. Since the response should be prompt in order to dissipate most of the energy externally, this approach works best for magnets with a low inductance. Passive protection relies on engineering design of the magnets to withstand internal dissipation of the energy, resulting in the transfer of this energy to the cryogens surrounding the magnet. Here, active protection is employed in the quadrupole while passive protection is utilized in the solenoid magnets.

The solenoid magnets and the quadrupole magnet are powered using separate power supplies. To improve the efficiency of the passive quench protection in the solenoids, diodes are installed across six subdivisions of each magnet. If the voltage across any subdivision surpasses the breakdown voltage of the diode, the diode begins conducting and shorts out that section. The diodes are physically large so that they can dissipate the energy in the form of heat.

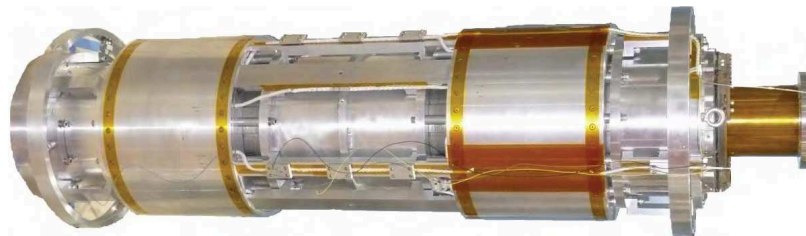


Figure 3.4: A photograph of the assembled Ioffe trap.

The quadrupole has a small inductance so that one can protect quenches actively. A quench is detected by monitoring the voltages across eight sets of coils. In order to distinguish a quench from voltages induced during normal field ramping, the voltage sum across opposing coils is measured. By summing the voltage of two coils from the same layer but with opposite current sense the induced voltages will cancel because they have equal and opposite magnetic flux penetration. A voltage signal is measured that remains zero even during a magnet ramp; any voltage signal above a pre-set threshold will be from resistive sources. For the KEK quadrupole magnet a signal that surpasses a threshold of 300 mV is used to initiate the quench protection circuitry.

When the quench protection voltage signal surpasses the threshold, a SN74121N multivibrator used in monostable mode produces a TTL signal. A LeCroy 688AL level adapter converts this TTL signal to a NIM logic pulse. A Phillips Scientific model 794 quad gate and delay generator is used to lengthen the pulse. This signal switches an isolated pull-up transistor through a MCT6 optocoupler to apply a floating 3.3 V power supply to the gate of the dump silicon controlled rectifier<sup>1</sup> (SCR),  $S_D$ , to switch it to a conducting state.

In normal operation, the current for the quadrupole is directed through a bank of four SCRs,  $S_{1-4}$ , shown in Figure 3.5. These thyristors are changed to their conductive state by applying a voltage greater than the threshold of 1.4 V across the gate and cathode. The SCRs only become non-conductive when the voltage across the terminals is reversed or the current flowing through them drops below a critical value. Therefore the magnets remain energized until they are ramped down fully by the power supplies, or until a quench is detected. Upon detection of a quench, the trigger from the quench detection is applied to the dump SCR,  $S_D$ . The energy stored in a capacitor bank acts to momentarily stop the flow of current in the magnets, thus turning  $S_{1-4}$  non-conductive. The current is then redirected through the dump resistor  $R_D$ , dissipating the energy stored in the magnet. The resistor, made from a 1.6 cm thick plate of 316 stainless steel, has a resistance of  $R_D = 100 \text{ m}\Omega$ . This gives a characteristic time of dissipation,  $L/R$ , of  $\sim 0.6 \text{ s}$ .

The purpose of resistors  $R_{1-4} = 0.6 \text{ m}\Omega$  is to regulate the current so that it is evenly divided between the four SCRs so that all four stay below their maximum rated currents. Since 460 W is dissipated in each resistor and 1.2 kW in each SCR when at full

---

<sup>1</sup>International Rectifier PN ST1200C20K

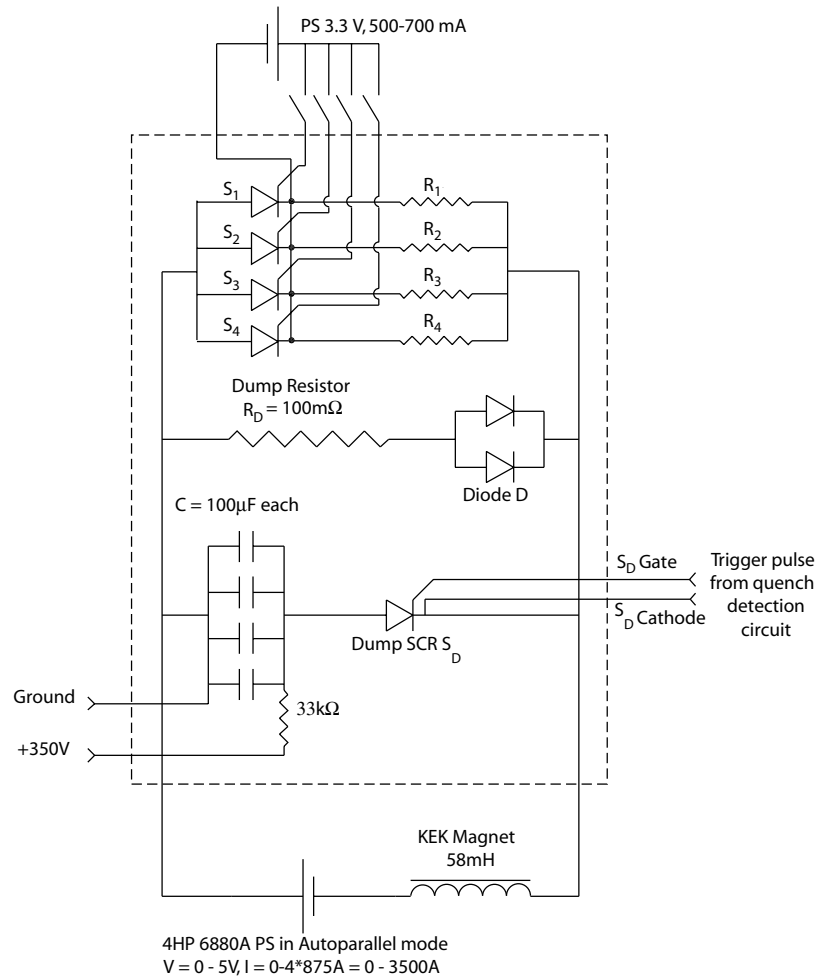


Figure 3.5: Circuit diagram for the active quench protection of the quadrupole magnet.

operating current, all are water cooled. A hardware interlock inhibits the power supplies when the cooling water is not flowing.

The KEK magnet was tested independent of the solenoids as described in previous work[58]. During these tests the dump resistor voltage was monitored to evaluate the quench protection efficiency of the system. It was determined that 95 % of the stored energy of the quadrupole magnet is dissipated in the dump resistor.

### 3.2.2 Magnetic Field Compensation

The experimental hall where the apparatus is located is also home to experiments that may be sensitive to magnetic fields. Notably, the spin-echo spectrometer uses precession of polarized neutrons about a magnetic field to achieve high resolution measurements of the energy transfer during a neutron scattering process. A magnetic field compensation coil was designed to reduce the stray magnetic fields from the magnetic trap and is optimized for cancellation at this instrument, located a distance of 15-17 m upstream along the neutron guide. The magnitude of the solenoid falls off as  $\propto 1/r^3$ , as opposed to the quadrupole field that falls off as  $\propto 1/r^4$ . Thus, one needs only to compensate for the solenoid fields at large distances. This can be accomplished by creating a field that mimics the opposing dipole moment,  $\vec{\mu} = NI\vec{a}$ .

For the size of dipole required, one must maximize both the number of turns,  $N$ , and the area of the coils,  $\vec{a}$ , given the maximum current power supply available. Two coils roughly 140 cm by 280 cm rectangular are attached to either end of the support frame for the two cryostat towers. This maximizes the efficient use of space in the experimental area, while still providing a large area dipole.

A large dipole field cancellation magnet was designed using the calculated fringe fields from the magnetic trap (see Section 4.2.1). It was found that compensation is optimized when two solenoidal magnets are energized, each with a current opposing the trap solenoids of 21500 A-turns. In the model, this configuration reduces the fields at the spin-echo instrument from an uncompensated 100 mG to  $<3$  mG.

The decision was made to limit the design to room temperature copper coils powered by an existing model EMHP 40-600-4111 power supply. This supply can provide a maximum current of 600 A at a voltage of 40 V. To minimize resistive heating, 0.635 cm by 3.175 cm copper bars were used to create the current loops. The number of turns,  $N$ , required for each coil was 39, at a current of 540 A. The copper bars are stacked in rectangular layers in the style of Lincoln Logs<sup>2</sup>, as shown in Figure 3.6, with the current path defined using insulating kapton film or conductive grease to insulate or connect adjacent bars. The geometry is realized by constructing two concentric coils on each end of the cryostat. The outer coil has 20 turns and encloses an area of 4.05 m<sup>2</sup> and is supported from the floor. A second coil of 19 turns and an area of 3.70 m<sup>2</sup> is placed inside the first and is supported

---

<sup>2</sup>Lincoln Logs is a trademark of HASBRO



Figure 3.6: Top view photograph of one field compensating solenoid magnet within an acrylic housing. Fans on the top of the housing provide cooling for the magnet. Also pictured in this photograph is the rack (black) for the quadrupole power supplies.

using 12.7 mm (0.5") thick acetal plastic sheets.

In order to maintain the temperature of the copper bars at  $< 60\text{ }^{\circ}\text{C}$ , an acrylic housing was constructed around the outside of the coils. Slotted air intakes are cut into the bottom of the acrylic housing, while two 15.24 cm (6") diameter fans of a non-magnetic aluminum construction are installed on the top of each acrylic case. The fan speeds are controlled by pulse width modulation and can be adjusted using a square wave generator with variable duty cycle. Without this cooling system the temperature of the coils rises to 80 – 100  $^{\circ}\text{C}$  at full field operation.

The coils are held together using stainless steel threaded rods electrically insu-

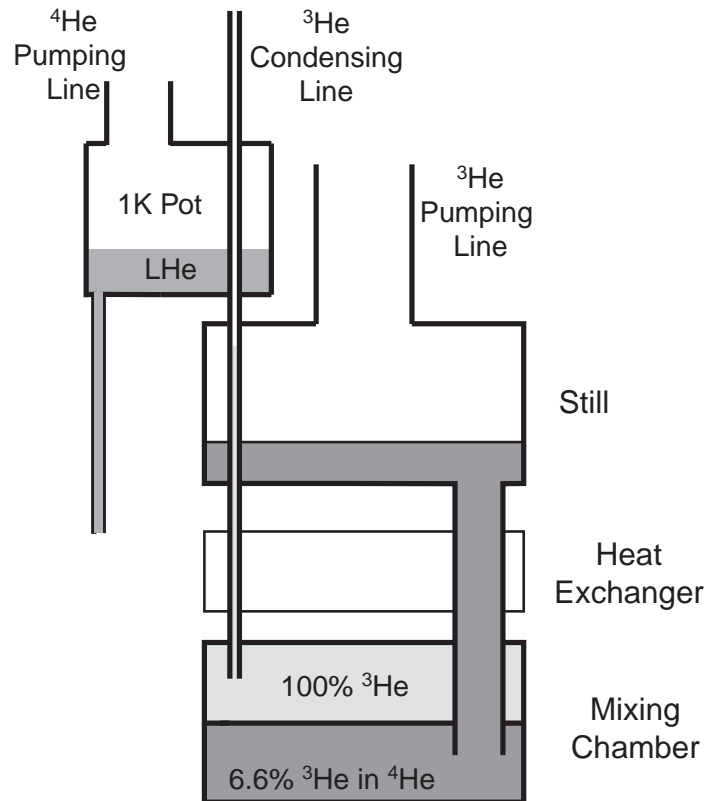


Figure 3.7: Schematic of the operation of a dilution refrigerator.

lated by nylon sheaths having a heat deflection temperature at 1.8 MPa of 60 °C[70]. An interlock system was designed to eliminate the danger of the magnet shorting above this temperature. Thermocouples are installed on the upper corner of each magnet. The voltages are monitored with two thresholds. The first threshold produces a TTL logic output to allow the DAQ to notify someone that there is a problem with the system. The second threshold will inhibit the compensation coil power supply, and output a TTL logic signal to the DAQ that initiates the magnetic trap power supplies to ramp the trap current down in a controlled manner.

### 3.3 Cryostat

The superthermal production of UCN described earlier requires the experimental cell to be filled with superfluid  $^4\text{He}$  at temperatures below 600 mK to suppress upscatter of

UCN. To further reduce the possibility of neutron upscatter from multiple phonon events ( $T^7$  dependence) the cell is further cooled to temperatures below 300 mK.

This temperature can be achieved using a commercially available dilution refrigerator<sup>3</sup> shown schematically in Figure 3.7. The operation of a dilution refrigerator relies on the principle that below the tri-critical point a mixture of  $^3\text{He}$  and  $^4\text{He}$  separates into two phases, a lighter “concentrated phase,” rich in  $^3\text{He}$  and a “dilute phase”, rich in  $^4\text{He}$ . Since the enthalpy of the concentrated phase is less than the dilute phase, as  $^3\text{He}$  crosses the phase boundary from concentrate to dilute the required energy is drawn from the surrounding environment. The concentration of  $^3\text{He}$  in the dilute phase can be reduced from the equilibrium value by pumping on the still. The vapor pressure of  $^4\text{He}$  is several orders of magnitude lower than that of  $^3\text{He}$ , and thus the  $^3\text{He}$  is preferentially removed from the mixture. To restore the equilibrium,  $^3\text{He}$  from the concentrate phase diffuses across the phase boundary, removing heat from the sample. The  $^3\text{He}$  is then recondensed back into the mixing chamber to sustain this cooling process. In order to minimize the heat load on the mixing chamber from the returning  $^3\text{He}$  it is cooled through a series of heat exchangers. First it is passed through a “1-K pot” which is a  $^4\text{He}$  refrigerator that operates at a temperature of 1.2 K by pumping on liquid  $^4\text{He}$ . The recondensed  $^3\text{He}$  is further cooled by the “Still” at  $\sim 0.6$  K from the evaporation of  $^3\text{He}$  being pumped through the cycle. Finally the recondensed liquid  $^3\text{He}$  follows the temperature gradient of the outgoing  $^3\text{He}$  in reverse through a series of counter-flow type heat exchangers as it makes its way back into the mixing chamber.

The cooling power of our refrigerator<sup>4</sup> was recently measured to be 1.1 mW at 300 mK[58]. For the mixing chamber and the experimental cell that is thermally linked to it to reach a base temperature  $< 300$  mK, they must be thermally isolated from the external environment. The isolation is achieved using layers of increasingly lower temperature, typically labeled by the boiling point of the cryogen used to cool the layer. A room temperature vacuum chamber “300 K” surrounds a “77 K” liquid nitrogen cooled jacket that blocks blackbody radiation from room temperature onto the “4 K” liquid helium vessel. Each layer is isolated by a vacuum region and many layers of aluminized mylar “super-insulation” that has very low emissivity and reflects the majority of the infrared radiation to the warmer layer.

---

<sup>3</sup>For a discussion on techniques of achieving low temperatures see Ref. [71].

<sup>4</sup>Oxford Instruments Kelvinox 400

The design for the new cryostat has three sections, as can be seen in Figure 3.8. Much like the previous cryostat<sup>5</sup>, there is a horizontal cylindrical section that contains the magnetic trap and the experimental cell that is required because the neutron beam that illuminates the experimental cell is horizontal. As the dilution refrigerator uses gravity to set up the phase boundaries and thermal gradients, it operates in a vertical orientation. To support the dilution refrigerator the tower from the previous apparatus was reused in the new cryostat. The inner vacuum chamber (IVC) is the volume surrounding the dilution refrigerator. It is a continuous vacuum space surrounding the dilution refrigerator and extending through the bore of the magnet to the light collection optics. This vacuum chamber was designed and constructed in-house. The outer vacuum chamber (OVC) is the vacuum space outside of both helium baths and between 77 K and 300 K. The 77 K heat shields do not provide any vacuum seals and solely block blackbody from room temperature to reduce heat loads on the 4 K shields and volumes. A second vertical section was added to the new design to accommodate the larger high-temperature superconducting (HTS) current leads for the quadrupole magnet.

There are two liquid helium volumes, one surrounding the magnet and extending into the tower for the magnet leads, and a second surrounding the dilution refrigerator. In the event that the magnet quenches, a large fraction of the liquid helium will boil as some of the magnets' energy is dissipated in the cryogenic bath. A large safety vent is installed on the magnet lead tower for this exhaust. All access for cryogen filling and instrumentation enters through flanges on the top of each tower. In order to create a thermal gradient between the bath and room temperature, low thermal conductivity stainless steel is used in the construction of the bath walls and baffles are installed with no direct pathways to the top of the chamber to slow convection of the boil-off gas. These baffles are also polished to reflect blackbody radiation that could additionally heat the liquid helium.

In the previous cryostat, all cryogenic shields were suspended from the top flange of a single tower to minimize thermal conduction between 300 K, 77 K, and 4 K. The weight of the new magnet trap is 560 kg, precluding this possibility. The new apparatus is now supported from the bottom. Cryogenic posts constructed from 1 mm thick G-10 fiberglass tubes support the shields and magnet assembly. The tubes are captured between an aluminum disk and a ring flange that are cryogenically shrink-fit in place[58]. At room

---

<sup>5</sup>The previous cryostat is described in detail in Ref. [72]

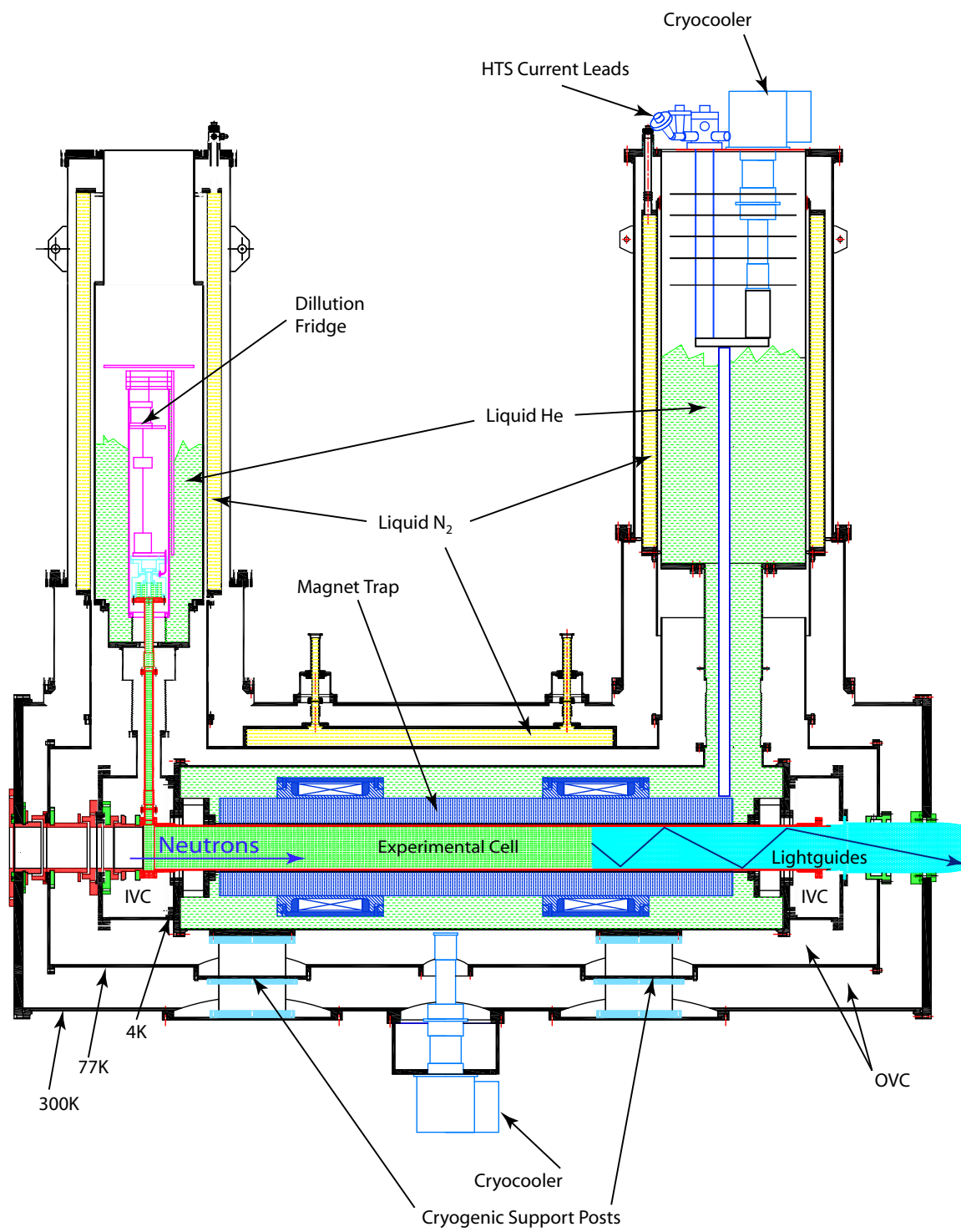


Figure 3.8: A cross sectional view of the cryostat.

temperature a single post was load tested at up to 1360 kg without failure. The magnet and supporting cryostat is supported on two posts of the same construction. To relieve stress from thermal contractions, one of these posts is bolted to all three cryostat layers, while the second support rests in the bottom of the 300 K layer on a sheet of Teflon.

Thermally linked to the bottom of the helium volume is a long copper bar 9.53 mm (3/8") thick. This copper bar thermally links the two support posts and allows one to extract the heat without depositing it into the liquid helium. The copper is an oxygen free, high conductivity (OFHC) grade with less than 0.001% oxygen content and a purity greater than 99.95%. Such high purity is required because the lattice conduction is limited by scattering of phonons from electrons, lattice defects, or other phonons. Thus the residual resistivity ratio ( $RRR = \rho_{273K} / \rho_{4K}$ ) can range from 20 to 2000 in copper[73] is dramatically affected by the purity of the metal. The heat load due to the cryogenic supports from room temperature into the 4 K helium bath is calculated to be 0.6–0.8 W. To remove the heat load from the support posts a Gifford McMahon type cryocooler<sup>6</sup> that provides 1.5 W of cooling power at 4.2 K is thermally linked to the copper bar. Copper braiding<sup>7</sup> made of oxygen free electronic (OFE) grade copper, a 99.99% pure copper with 0.0005% oxygen content, is used to thermally link the cryocooler to the copper bar while allowing freedom for thermal contraction as the apparatus cools. Copper braids are also used to shorten the thermal distance from the ends of the copper bar to the neutron entrance and light exit windows, as these are also significant sources of heat load to 4 K.

Typically a superconducting magnet is operated in what is known as “persistence” mode. The magnet is energized and the superconducting coils are then shorted together. As long as the magnet is kept below the superconducting critical point, the wires have no resistance and dissipate no energy, allowing the magnet to remain energized indefinitely. This method of energizing the trap is not feasible due to the procedure for cleaning the magnetic trap of above threshold neutrons. As described in Section 4.2, the magnets are ramped to lower current immediately after filling the trap with neutrons. The ability to ramp the fields requires a continuous current sink and source.

To bring 3400 A into the liquid helium bath using conventional vapor cooled leads as done with the earlier traps would result in a continuous heat load of 8.2 W. Dissipating this heat in the helium bath results in a cost prohibitive helium consumption rate of

---

<sup>6</sup>Sumitomo model SRDK-415D

<sup>7</sup>Purchased from Cooner Wire, Inc., Chatsworth, CA.

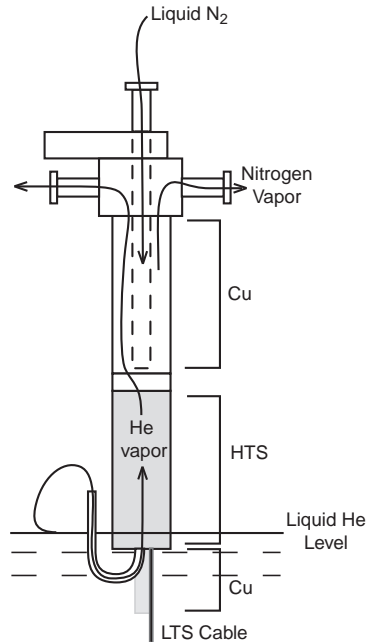


Figure 3.9: Schematic of the Fermilab HTS current leads.

246 L/day. High temperature superconducting (HTS) materials were used to ameliorate this problem. At Fermilab, HTS leads were developed to replace about 50 pairs of 5-6 kA leads[74]. The lab has graciously given a prototype pair of these leads for use in the apparatus.

The leads, as shown in Figure 3.9, are constructed in three sections. The upper section is constructed from copper and provides a thermal gradient from room temperature to the HTS section. The middle section consists of parallel tapes of BSCCO-2223 (Powder-In-Tube) multifilamentary conductor in a silver alloy matrix. The  $\text{Nb}_3\text{Sn}$  low temperature superconductor (LTS) leads are connected to the HTS section through a copper section that also acts as a thermal link to 4 K. Since the HTS material must be kept below 80 K to remain superconducting, the copper/HTS junction is cooled with a continuous flow of liquid nitrogen. The boil-off nitrogen gas is passed through meters to regulate the flow to 0.7 g/s (70 scfh), consuming about 70 L/day of liquid nitrogen. Helium vapors provide further convective cooling to the leads. To maintain a temperature below the critical point of the HTS material it is recommended to maintain a flow rate of 0.026 g/s of the boil-off vapors through the current leads. This corresponds to a helium consumption rate of about

16 L/day passing through the leads. While the boil-off helium is allowed to pass through the leads, it is also routed out of the apparatus through a separate vent for safety. The fraction of vapors that are allowed through each current lead is less than recommended[75], so a second cryocooler<sup>8</sup> is thermally linked to the bottom copper section of the current leads to provide an additional 1.5 W of cooling power at 4.2 K. A thin layer of kapton is used to provide the necessary electrical isolation.

Since thermal gradients across the leads may vary depending on the operating conditions there is a risk of operation above the critical current that could trigger a quench within the HTS material. As in the superconducting magnets, a quench needs to be detected, however the required actions are different because the amount of stored energy is significantly smaller. The straight sections of HTS leads have a very low inductance so any measured voltage must arise from a quench. The manufacturer recommended minimum voltage for quench detection is 3 mV. In this event the current through the leads must be stopped within 20 s to prevent damage. In addition, it is recommended to take this action if the copper section surpasses 30 mV.

In the previous design of this protection system, the HTS lead voltages were summed with the magnet quench threshold. In this configuration a quench trigger from the leads would cause all of the energy stored in the quadrupole magnet to be dumped into the quench protection circuit shown in Figure 3.5. Since the energy density of the HTS leads is considerably lower than in the magnets and a quench propagates more slowly within the HTS material, it is desirable to slowly remove the energy from the magnets to avoid triggering a quench in the magnets. A new protection scheme is to use a separate trigger that starts a slower ramp-down of the current. In order to avoid false triggers due to noise, filtering is implemented with the active operational amplifier circuit shown in Figure 3.10.

The use of HTS current leads for the quadrupole magnet significantly reduces the heat into the liquid helium bath. For similar reasons, HTS tape leads are also being used for the 250 A low-current leads. The 30 cm long multi-filamentary HTS tape leads<sup>9</sup> are rated for 250 A at 64 K, however the rating is reduced in a high magnetic field. The maximum field in the location of the leads is expected to be 0.3 T in the directions parallel to the plane of the tape, resulting in a rating factor of 0.8 that should be applied at 64 K. Silicon diode thermometry is placed on either end of the HTS current leads and is monitored to

---

<sup>8</sup>Sumitomo model SRDK-415D

<sup>9</sup>HTS-1100 Ltd. from New Zealand

ensure the current ratings are not exceeded.

The current is carried from room temperature power supplies to the HTS leads through a carefully designed wire. This wire has a specific ratio of cross sectional area to length  $A/L = 4.5 \times 10^{-3}$  cm that minimizes both the ohmic heating in the wire and the conductive heating of the leads. For details of this calculation see reference [58]. The length of the wire is 13.7 cm and extends to the Cu-HTS junction that is connected to the first stage of a cryocooler mounted on the top flange of this tower. To maintain the calculated  $A/L$  ratio, this fixed distance requires a wire diameter of 2.9 mm. The first stage of this cryocooler provides a cooling power of 40-50 W at 64 K. This is sufficient to remove the 12.6 W of heating at the junction. The thermal connection between the cryocooler and the current leads is electrically isolated using a kapton film. The low temperature end of the HTS leads are connected to the magnet wires through a 19 cm long, low-temperature

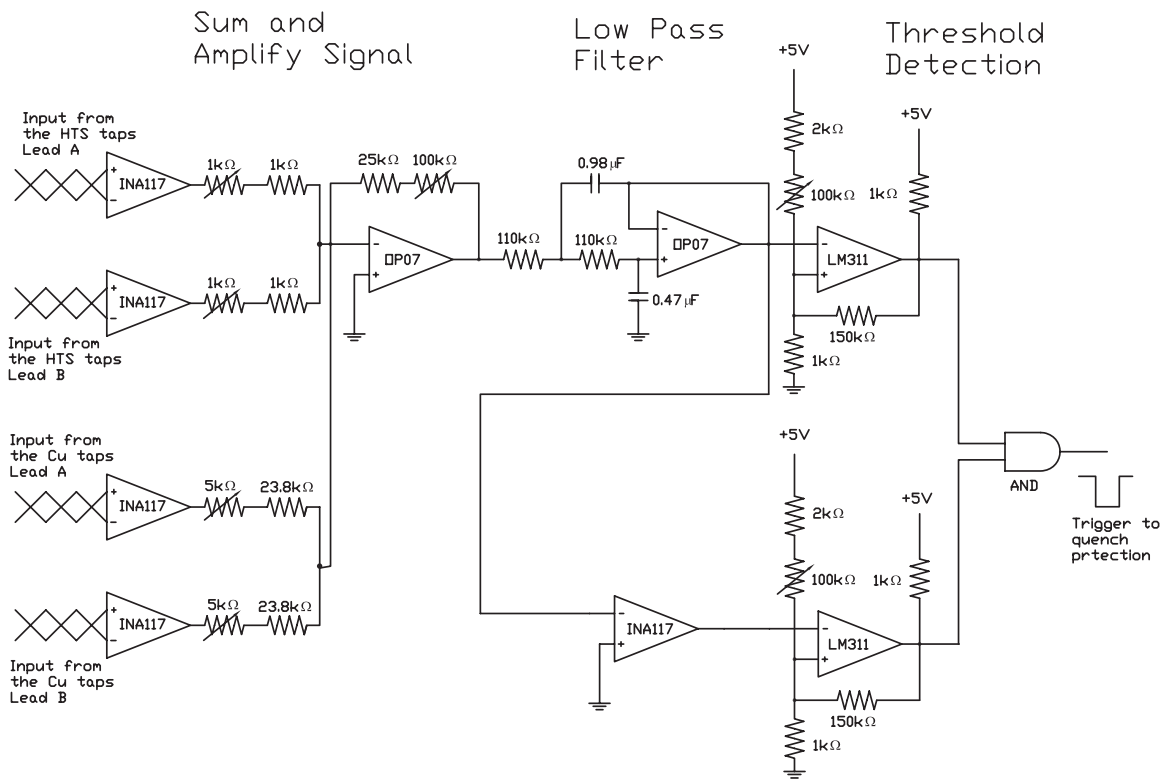


Figure 3.10: HTS high current leads quench detection

superconducting bus bar<sup>10</sup> (LTS). This bus bar is above the liquid level in the helium bath, however it is made of a Nb<sub>3</sub>Sn material with a critical temperature of 18.3 K and is supported by copper bars that provide cooling of the wires outside of the liquid. Additionally this material has a high threshold for magnetic fields, a current density of 2680A/mm<sup>2</sup> has been claimed[76] at fields of 10 T.

### 3.3.1 Neutron Entrance

One of the major modifications to the cryostat was the redesign of the neutron entrance area that allows the external beam (described in Section 3.1) to enter the cell. The beam entrance performs multiple functions, it allows the neutrons pass through the vacuum and radiation shielding with minimal loss in order to maximize the number of neutrons that enter the cell, it blocks blackbody radiation from warmer areas to reach cooler areas with minimal neutron activation, and it shields the remainder of the apparatus from exposure to the entering neutron beam.

Almost all neutrons entering the measurement region are absorbed through neutron capture reactions in the materials surrounding the cell. This absorption deposits about 44  $\mu$ W in the cell. Additional heat loads associated with transporting neutrons into the cell should be kept to a minimum. Due to the finite cooling power of the dilution refrigerator one must minimize conductive loads along the neutron beam flight path. Similarly, there should be minimal convective or radiative loads.

A schematic of the neutron entrance area is shown in Figure 3.11. There are three vacuum windows that are each made from 20 mil (508  $\mu$ m) thick perfluoroalkoxy (PFA) Teflon<sup>11</sup> film[77]. Teflon does not have any metallic contaminants that could activate and potentially produce background events in the apparatus. While fluorine does activate, its lifetime is 1.6 s, and will have decayed away prior to the observation of the neutron lifetime. Since Teflon is a soft material, often used as a gasket material to create seals, one is able to clamp the material tightly against a smooth, scratch-free surface to create a vacuum seal. Windows of this type are found on the room temperature 300 K vacuum seal, at 4 K between the OVC and IVC, and on the end of the experimental cell to contain superfluid helium. These windows efficiently pass neutrons, have minimal activation, and provide reliable vacuum seals.

---

<sup>10</sup>American Magnetics, Inc.

<sup>11</sup>Teflon is a registered trademark of E. I. du Pont de Nemours and company

The Teflon material is however not an ideal material to block blackbody radiation. With no additional windows, blackbody radiation would have a direct line of sight on the experimental cell and provide a significant heat load. Two additional windows made from beryllium<sup>12</sup> foil are included in the flight path. One at 77 K blocks blackbody radiation from 300 K to 4 K, and a second at 4 K blocks the radiation originating at 77 K from reaching the experimental cell. Beryllium activates with a long lifetime of  $6.83 \times 10^{13}$  s, for this reason the background from beryllium activation is essentially a constant background, and introduces no systematic shift in the neutron lifetime. For a discussion of the activation analysis of the beryllium foils and the identification of trace impurities see Ref. [67].

As the neutrons enter the apparatus, the entire neutron beam having a divergence of  $\pm 1^\circ$  illuminates the entrance windows. Scattered and highly divergent neutrons are captured in the surrounding materials and could produce backgrounds to the experiment. Materials exposed to the beam must be chosen such that the only by-product of the neutrons' deposited energy is prompt gammas. The predominant capture process used to absorb neutrons that are scattered out of the beam is  $^{10}\text{B} + \text{n} \rightarrow ^7\text{Li} + \alpha$ . In this reaction the  $^{10}\text{B}$  captures a neutron becoming an excited state of  $^{11}\text{B}$  for a short time  $\sim 10^{-12}$  s upon which it fissions producing  $^7\text{Li}$ , an  $\alpha$  particle, and a  $\gamma$  in 94% of reactions. Although the reaction produces a large signal in the apparatus, it is entirely prompt and therefore not a background during the observation period approximately 300 s after the beam is blocked. Natural boron contains an abundance of  $^{10}\text{B}$  of 0.199. There is a sufficient amount of  $^{10}\text{B}$  in natural Boron Nitride<sup>13</sup> (BN) to completely shield the apparatus from the neutron beam. In the flight path between 300 K and the cell, one must construct a shield for the surrounding apparatus that is hermetically sealed to neutrons, while maintaining vacuum spaces to break the thermal gradient between layers of the cryostat. To accomplish this flight tubes are interleaved as shown in Figure 3.11. The vacuum space between layers is minimized so that a neutron must reflect multiple times before it could escape the flight tube. The probability of neutron capture on boron in this region is near unity.

### 3.3.2 Experimental Cell

The experimental cell is the centerpiece of the apparatus. Within the cell, UCN are produced using the superthermal technique in isotopically pure  $^4\text{He}$  that has been

---

<sup>12</sup>The beryllium foils are purchased from Brush Wellman Engineered Materials, Fremont, CA.

<sup>13</sup>Saint Gobain Ceramics Grade AX05

cooled to  $T \lesssim 300$  mK. Extreme ultraviolet (80 nm) scintillation light produced in the same helium by the neutron decay electron is converted to visible light (430 nm) by Tetraphenyl Butadiene (TPB) lining the trapping region. The visible light is transported from the cell out of the apparatus through acrylic light guides. To perform all of these functions there are many constraints placed on the cell. It must contain superfluid helium at  $T \lesssim 300$  mK. All joints in the cell must therefore be leak tight and mechanical supports should conduct minimal amounts of heat. Neutrons must enter the cell from one end and the interior must be shielded to minimize neutron capture events that have the potential of generating background events within the cell. The other end must have an optical widow to transport

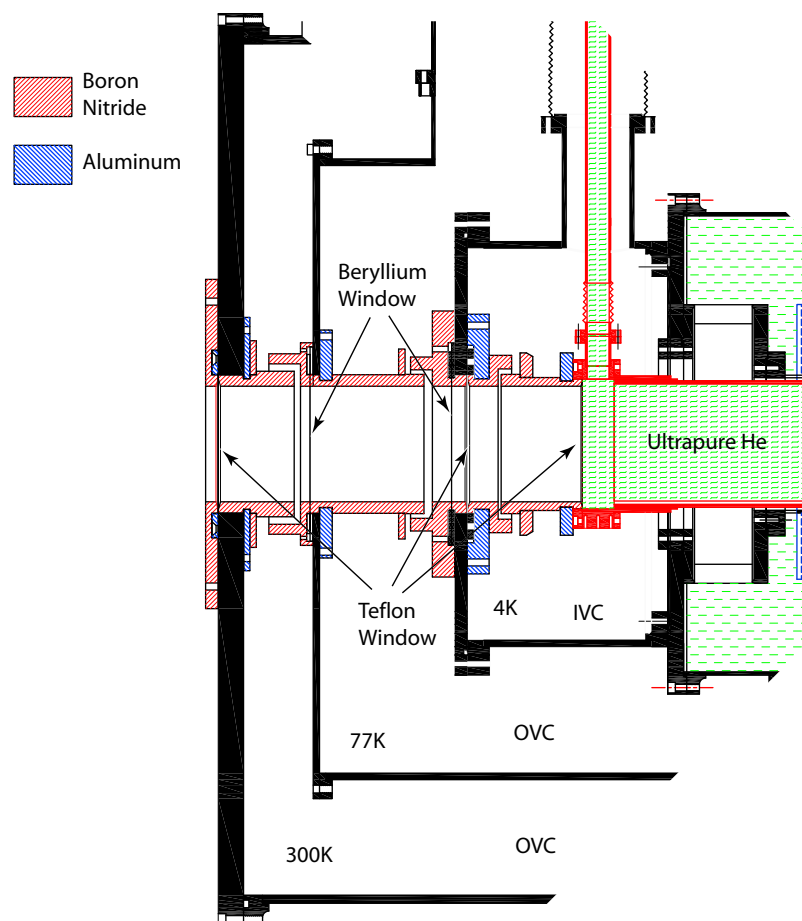


Figure 3.11: A side view of the neutron entrance and shielding materials. The boron nitride is used to shield the apparatus from neutrons to minimize activation.

the visible light signal out of the experiment. Solutions to each of these constraints are described in detail here.

One advantage of the ‘U’-shaped cryostat design over the previous ‘T’-shaped design is simplified plumbing of the helium to the cell. Since the vertical section housing the dilution refrigerator is situated over one end of the cell, the linkage between the refrigerator and the cell can be made through a 2.54 cm diameter cupronickel (CuNi) vertical tube connecting to one side of the cell. The other end of the vertical tube is connected to a buffer cell attached to the bottom of the dilution refrigerator mixing chamber.

Below the lambda point, superfluid helium has the unique characteristic of zero viscosity. Thermal conduction no longer takes place as a diffusion process, rather it takes on the characteristics of wave propagation (known as second sound [65]). At 300 mK, the thermal conductivity is high enough that thermal gradients across the cell will be small,  $< 1$  mK. Two copper fins inside the buffer cell are coated with sintered silver to overcome Kapitza resistance  $\lesssim 300$  mK. The entire volume of the cell must remain in good thermal contact with the mixing chamber of the refrigerator. Forces arising from the thermal contraction of the CuNi tubing is minimized using two beryllium copper bellows.

The cell is constructed from 316L grade stainless steel tubing with an outer diameter of 12.7 cm (5”), an inner diameter of 12.4 cm (4.875”), and length of 182.9 cm (72”). This tubing was custom produced using a cold-extrusion process called flowforming<sup>14</sup>. In this process a blank is created that is spun and pressed into a mandrel. Localized heating causes the thinning and extension of the material. The extrusion process can be precisely controlled to create the required thickness and diameter of the final tube.

The clearance between the cell and the IVC tube is between 5–6 mm over the 1610 mm length through the magnet. It is critical that the cell supports suspend the 26 kg mass of the cell for prolonged periods (a typical reactor cycle is 40 days) with little relaxation, while conducting minimal heat to the cell. Zylon is a high strength, low creep, liquid crystalline material that can be spun into long fibers. With a room temperature ultimate tensile strength of 37 cN/dtex, Zylon has almost twice the strength of Kevlar. Used in its filamental form, 8.25 cm long single fibers support the cell from the 4 K shield. The thermal conductivity of Zylon was extrapolated from data taken between 10 K and 260 K to be  $k_Z(T) \sim 10^{-5}$  W/cm K at a temperature  $\approx 2$  K[78]. This is similar to the

---

<sup>14</sup>Purchased from PMF Industries, Williamsport, PA

value measured for Kevlar,  $k_K(T) = 8 \times 10^{-6}$  W/cm K at 2 K[79]. For the design, it was assumed that a comparison in the performance of the fibers could therefore be scaled by the ultimate tensile strength.

Recent measurements of the thermal conductivity of Zylon at low temperature suggests otherwise[80]. The thermal conductivities of Zylon and Kevlar are indeed similar at 4.2 K; for Kevlar  $k_K(4.2 \text{ K}) = 4.5$  mW/cm K and for the Zylon  $k_Z(4.2 \text{ K}) = 1$  mW/cm K. The temperature dependence of the thermal conductivity for the Zylon,

$$k_Z(T) = (440 \pm 10) \cdot T^{2.30 \pm 0.03} \frac{\text{pW mm}}{\text{dtex K}^{2.3}}, \quad (3.1)$$

was however found to be less than that of the Kevlar,

$$k_K(T) = (100 \pm 5) \cdot T^{2.71 \pm 0.04} \frac{\text{pW mm}}{\text{dtex K}^{2.3}}. \quad (3.2)$$

These expressions of the thermal conductivity represent the cross sectional area of the fibers in terms of their decitexi (dtex). Due to this temperature dependence, the thermal conductivity of a fiber spanning the temperature range 0.3 K to 4.2 K can therefore be estimated by the properties of the fibers at  $T = 0.7 \pm 0.1$  K. Additionally, since the ultimate tensile strengths of the materials are also of interest, one can normalize the thermal conductivities by this strength to determine an approximate figure of merit. For Zylon at 0.7 K one finds,

$$\frac{k_Z(0.7 \text{ K})}{\sigma_Z} = 5.24 \frac{\text{pW mm}}{\text{cN}} \quad (3.3)$$

and for Kevlar,

$$\frac{k_K(0.7 \text{ K})}{\sigma_K} = 1.83 \frac{\text{pW mm}}{\text{cN}}. \quad (3.4)$$

Using this new data it appears that at an operating temperature of 300 mK Kevlar is a better choice for the mechanical supports. The current design using Zylon is nevertheless sufficient to support the cell with minimal heat loads.

Metals are used in the cell construction for their rigid structure, and the ability to contain superfluid helium. As they are conductive materials they may sustain eddy currents during magnet ramps introducing another type of heat load on the experiment. Some metals are also ferromagnetic and retain a magnetization after the magnetic fields are removed. The grade 316L was chosen for its low magnetization and high resistance to eddy current heating. The end flanges for the cell are made from CuNi<sup>15</sup>, another material which meets

---

<sup>15</sup>The cell is not entirely made from CuNi because the material was not as easily obtained as stainless steel.

these criteria. This material is useful in that it can be bonded using a low temperature soft solder, while stainless steel can only be bonded by higher temperature brazing or welding processes. The mating surface of the cell is prepared for the soft solder connection with the end flanges by brazing a sleeve of CuNi which is small enough to pass through the IVC tube. The end flanges are larger in diameter than the IVC tube through the magnet and one of these flanges must be sealed after the cell is inserted. Because this is done in place the seal is made horizontally which is not the ideal mode for capillary action in this geometry. The solder tends to pool in the bottom of the joint making it a difficult seal.

Soldering and brazing are processes in which a liquid is introduced into a small gap through the capillary action[81], it then hardens as it cools forming a bond between the surfaces on either side of the gap. The material with an appropriate surface energy will attract the liquid solder. If the spacing between the two materials is small enough, the surface energy of the materials being joined will draw the liquid through the joint forming a seal that is impervious even to superfluid helium. Since the melting temperature for 50/50 PbSn soft solder is 220 °C this can be a repeatable process if the seal needs to be removed as is often the case with the cell end flanges. For example, anytime the IVC or magnet needs repair this must be removed and replaced. Silver solder<sup>16</sup>, the alloy used in brazing, has a higher melting point 630 – 710 °C. This is much closer to the melting temperatures, 1100 – 1300 °C, of typical metals joined by braze, therefore there is more of a risk of deformation when brazing, and while possible to remove and replace it isn't as easy to work with in the confined spaces of the apparatus.

As described in Section 3.3.1, a Teflon Window admits neutrons into the experimental cell. While helium is observed to diffuse through a 508  $\mu\text{m}$  thick Teflon window with an area of 103  $\text{cm}^2$  at rates in excess of  $10^{-4}$  mbar L/s. This diffusion rate drops below  $10^{10}$  mbar L/s when the temperature of the Teflon reaches 77 K[77].

Of the neutron flux entering the cell,  $\phi_n = 7.1 \times 10^6 \text{ cm}^{-2}\text{s}^{-1}$ , only 40,000 UCN are expected to be trapped in a loading period of 2100 s. With a neutron entrance window area of 103  $\text{cm}^2$  this relates to a production fraction of  $2.6 \times 10^{-8}$ . The remaining  $1.53 \times 10^{12}$  neutrons only contribute by producing backgrounds. As in the neutron entrance window, a BN grade AX05 material is used to absorb neutrons in the cell. Interlocking 3.5 mm thick tubes line the interior of the experimental region to block the neutrons from activating the

---

<sup>16</sup>Typically an alloy of silver, copper and zinc, but also may contain cadmium tin or nickel.

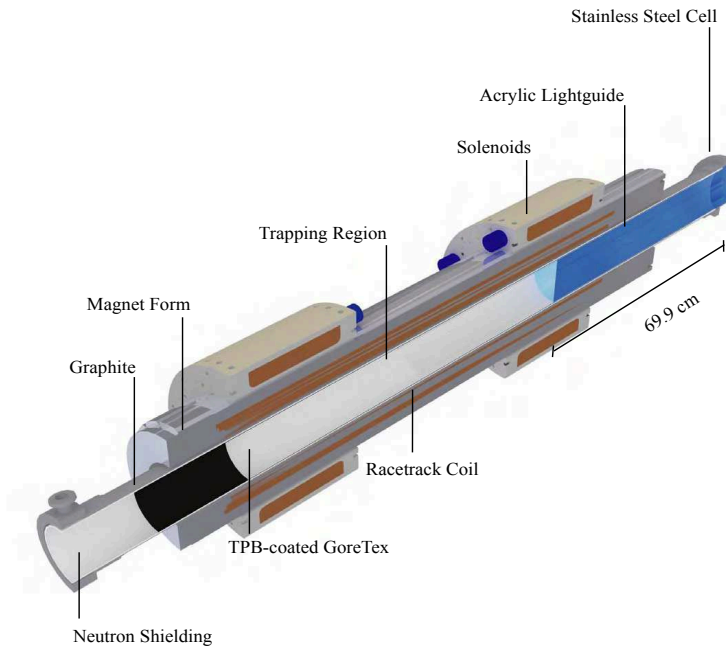


Figure 3.12: A cross section of the experimental cell.

surrounding cell metals. This thickness is roughly six characteristic attenuation lengths for the absorption of the 0.89 nm neutrons[82]. It was shown previously that BN produces luminescence light from neutron irradiation at low temperatures[83]. Since this produces time-dependent backgrounds, a 1 mm thick tube of graphite is inserted within the BN tubing to block this light. The graphite used is an industrial grade<sup>17</sup> which has been purified by baking, leaving only a trace amount ( $< 5$  ppm) of ash impurities. The detector insert is TPB evaporatively coated onto a Gore-Tex<sup>18</sup> substrate. Gore-Tex is a very pure material as it is made from expanded PTFE-Teflon, and has only the same short fluorine lifetime activation issues as the Teflon entrance windows. The cell light guide is a cast acrylic rod made from ultraviolet transmitting (UVT) grade polymethyl methacrylate (PMMA)<sup>19</sup>. The characteristic scattering length for the 0.89 nm neutrons in acrylic is nearly 0.2 cm, thus neutrons reaching the light guide will be scattered within a centimeter or so. The only place for them to scatter to is the walls of the cell where they will be absorbed in the BN shielding material.

<sup>17</sup>Poco Graphite, Inc. grade TM-1

<sup>18</sup>Gore-Tex is a registered trademark of W. L. Gore and Associates

<sup>19</sup>Supplied by Laird Plastics, Inc.

The detector inserts were produced by evaporating TPB onto an embossed Gore-Tex GR gasket material. Due to size limitations of the bell jar which was evacuated for the evaporations, sheets of 14 cm (5.5") by 19 cm (7.5") were coated with an average TPB screen density of 0.29 mg/cm<sup>2</sup>. The optimal coating thickness was found in earlier work[61] to be 0.2 mg/cm<sup>2</sup>. These inserts were then tiled two by two, creating 14 cm segments the entire length of the experimental region. The molecular dynamics of a recoil beta from the decayed neutron produces prompt EUV light which is downconverted in the TPB layer of the detector inserts. Diffuse reflections guide this light to the light guide for collection in the PMT detector outside of the apparatus. The details of the design are given in the next section.

In the previous apparatus the isotopically pure <sup>4</sup>He was stored at room temperature in four 0.45 m<sup>3</sup> tanks at a pressure of about 3 bar[62]. Since the expansion ratio of liquid helium to room temperature gas is 1 to 757, this is sufficient to store about 7 L of liquid helium as room temperature gas. The volume of isotopically pure liquid required to fill the cell is nearly 15 L, so a storage with at least twice the capacity of the previous system is required. For a safety margin one would also like to store a larger volume, at least 23 L of liquid helium. At a pressure of 3 bar, the capacity of the pump previously used for pressurizing the storage tanks, this would mean a storage volume of 6 m<sup>3</sup>, or about 13 tanks of the same volume as the previous system. Since there is not enough real-estate for this in the experimental hall it was clear that higher capacity compression was going to be necessary. In the new system the former is used as the first stage of compression. After that system a single stage metal diaphragm compressor<sup>20</sup> capable of a 41 bar pressure difference compresses the helium into high pressure gas cylinders for storage. A bank of nine 50 L cylinders provides adequate storage for nearly 24 L of liquid helium. To prevent contamination from natural purity helium in the experimental hall all of the seals are made by metal VCR<sup>21</sup> gaskets. This is because rubbers, and other polymer type of seals are known to diffuse helium[84]. Furthermore the valves, regulators, and the compressor were specifically chosen to utilize all metal seals.

---

<sup>20</sup>Fluitron, Inc. model S1-35

<sup>21</sup>VCR is a registered trademark of Swagelock, Solon, OH.

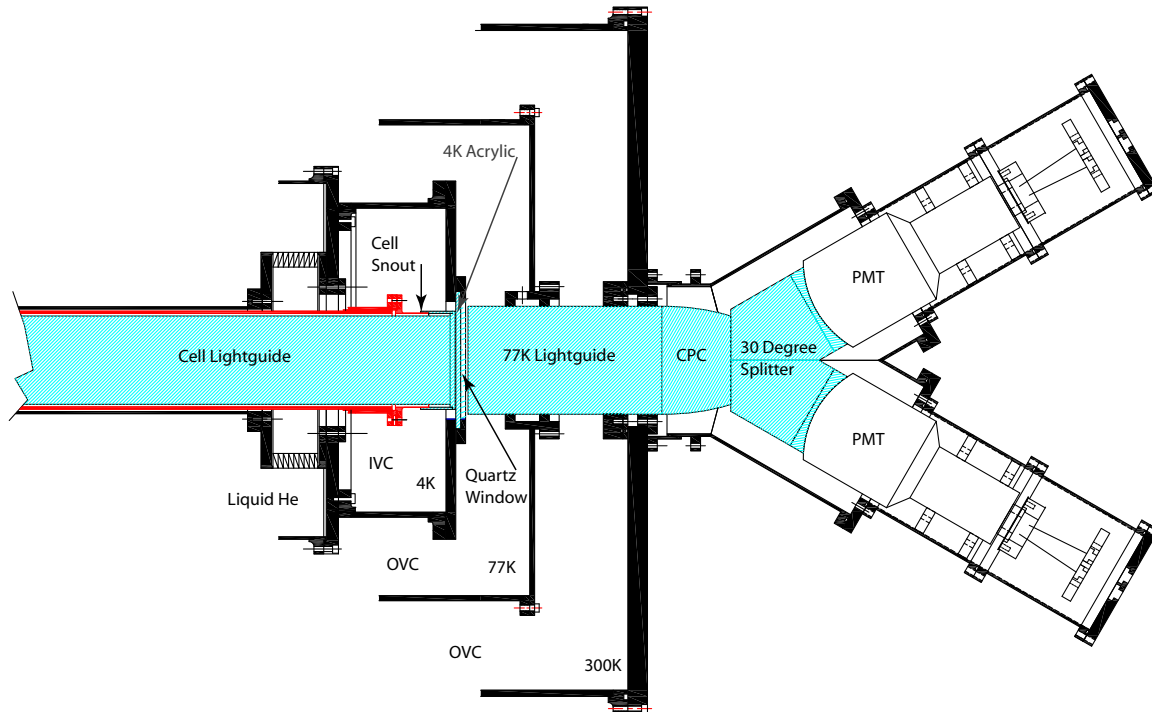


Figure 3.13: A top view of the new light collection system. Illustrated here are the cryostat in black, the experimental cell in red, and the light collection system in blue.

### 3.3.3 Light Collection System

The visible light signal generated in the TPB coating of the cell wall must be transported out of the apparatus. The efficiency of the collection system directly impacts the detection efficiency and an improvement will help to increase statistics. Since the geometry of the magnetic trap is not ideal for collecting a signal, it was decided that a systematic approach for upgrading the light collection system was needed.

The approach taken is to model the photon propagation using the ray tracing code GuideIt. This code is based on the earlier CERN Fortran code Guide7[85]. From input of the boundary conditions of a specified light guide geometry, the code is capable of tracking likely paths for photons using Monte Carlo techniques. The output provides the number of photons that have crossed each surface. In this manner, the efficiency of the light collection system can be estimated. Modifications were made to this code that added capabilities for both diffusely reflecting surfaces and improved source generation. These modifications improve estimates of the light generation and propagation from a beta event originating

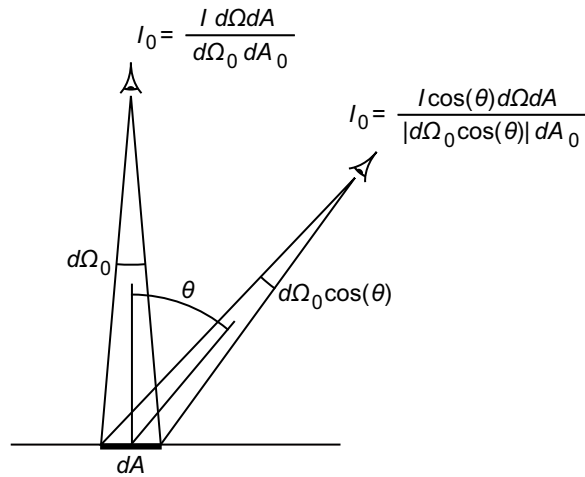


Figure 3.14: Lambert's cosine law requires that for a surface with an apparently uniform intensity emitted from all angles must in fact be emitting light with a  $\cos\theta$  dependence in order to account for the observing aperture's subtending of a surface area[87].

within the experimental cell. The code has been successfully benchmarked against both a simple LED test cell and calibration data obtained using the previous apparatus[62].

One significant improvement in the design of the new cryostat that allowed a greater flexibility in design of the new collection system is the extended length between the 4 K helium bath flange and room temperature. This allowed for two major improvements. An improved design of the 300 mK window makes this a more reliable vacuum seal and a longer 77 K light guide element allows for a longer thermal path between 300 K and 77 K without the use of additional higher thermal conductivity materials such as the sapphire window of the previous apparatus.

### Modeling Diffusely Reflecting Surfaces

A fully specular reflection is one where all of the reflected intensity is distributed into the same angle from the normal as the angle of incidence from the source illuminating the surface. Conversely, a material where there is no angular dependence of the reflected intensity is called a Lambertian reflector[86]. The intensity emitted from such surfaces follows a  $\cos\theta$  angular distribution that acts to cancel the angular dependence on the surface area as seen by the external observer (see Figure 3.14).

The technique of a Monte Carlo simulation relies on a uniform distribution of

randomly chosen numbers. Hence, scenarios where a fractional probability should be distributed randomly is straight forward. For example, starting with a fraction,  $a$ , of the interactions that reflect specularly, one defines a random variable with uniform probability from zero to one,

$$\int_0^1 dx = x|_0^1. \quad (3.5)$$

If the value of this number is less than the fraction,  $x < a$ , then in this case an outcome with the probability of  $a$  is observed. For example, a photon is reflected specularly. If a large enough population of scenarios is sampled, a representative distribution is produced. One can generalize this to a distribution that is not uniform by selecting a function,  $f(y)$ , for which a random variable chosen with a uniform probability, this then provides a random number with a weighted distribution,  $F(y)$ ,

$$\int_0^1 f(y) dy = F(y). \quad (3.6)$$

This is known as a probability density function (pdf). An example of this is if one were to generate an angular distribution that is uniform in all directions, one must populate the solid angle uniformly:

$$\int d\Omega = \int_{-\pi}^{\pi} \int_0^{2\pi} \sin \theta d\theta d\phi. \quad (3.7)$$

In order to accomplish this one needs two random numbers. For the first random number a pdf is defined as follows,

$$f(y) = \cos \theta|_0^1 \Rightarrow F(y) = \sin \theta, \quad (3.8)$$

so as to define the  $\sin \theta$  weighting. Then the second random number defines,

$$\phi = \int_0^{2\pi} d\phi, \quad (3.9)$$

a uniform weighting of the  $\phi$  variable from 0 to  $2\pi$ . Therefore, in order to implement Lambert's cosine law to define the proper distribution of angular intensity for a diffuse surface, one applies the following pdf:

$$f(y) = \cos^2 \theta \Rightarrow F(y) = 2 \sin \theta \cos \theta. \quad (3.10)$$

The above discussion is representative of how a Monte Carlo simulation reproduces interactions that result in known stochastical distributions. A complete Monte Carlo will

follow deterministic trajectories from one such stochastic interaction to the next, this is also called ‘ray-tracing.’ The pdf shown in Eqn. (3.10) can be applied to represent interactions with a diffusely reflecting surface. The next section will discuss how this interaction was implemented in the simulation of light collection efficiencies of the neutron lifetime apparatuses.

### Light Collection Simulations

GuideIt implements routines that impose a boundary condition referred to here as the surface detail, which simulate reflections from the surface that are not caused by a mismatch of refraction indices. The possibilities for surface detail include ‘MIRROR’, ‘METAL’ or ‘NONE’. The detail named ‘MIRROR’ creates a surface that produces completely specular reflections with unit probability. ‘METAL’ is a surface detail routine that accounts for the photon interactions through the photoelectric effect. In addition, a surface detail routine called ‘PAPER’ has been written which allows for reflections off a diffuse wrapping. Two Monte Carlo parameters must be set for each instance of the ‘PAPER’ detail. One parameter, ‘ABSORPTION’, allows a fraction of the photons incident on the paper to be absorbed into it, and the second, ‘SPECULARITY’, defines the fraction of specular reflections. The specularity code has been modified by Steven Williamson at University of Illinois at Urbana-Champaign to include the proper distribution, Eqn. (3.10) for a diffuse Lambertian surface.

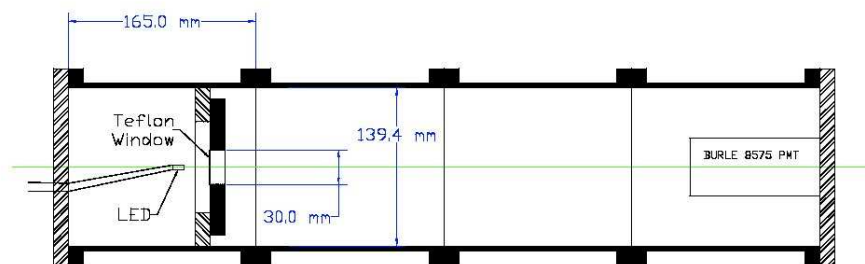


Figure 3.15: The experimental apparatus used to benchmark a new routine for simulating diffuse reflecting surfaces.

An experimental setup was designed to benchmark the performance of this new subroutine in GuideIt. A test cell was constructed that consisted of a segmented aluminum

tube. A blue LED was mounted on one end flange and placed behind a bulkhead with Teflon tape stretched across a circular opening 30 mm in diameter in the center as shown in Figure 3.15. The Teflon window is assumed to create a uniform source of light. A Burle 8575 photomultiplier tube (PMT) was mounted on the other end of the cell for light collection. The LED was pulsed using an HP 8013A Pulse Generator. This setup created a cylindrical region between the LED source and the PMT for insertion and testing of different paper wrappings around the diameter of the tube. The light collected in the PMT originated either directly from the source or from reflections off of the paper wrapped walls.

A pulse height spectrum was taken for various cell lengths with both black construction paper and Tyvek<sup>22</sup> lining the cell walls. A comparison was then made between the pulse height peaks for a cell with black walls that absorb most photons and a cell with Tyvek walls that reflect a significant number of photons. Since the difference in the two cases was the material lining the walls, an asymmetry was formed to highlight this difference,

$$2\frac{T(z) - B(z)}{T(z) + B(z)}. \quad (3.11)$$

Here,  $T(z)$ , represents the pulse height peak position when the source was situated a distance  $z$  from the detector with Tyvek lining the setup walls, and  $B(z)$  is the same except for black paper lining the walls.

This asymmetry is small at close distances when the majority of the light that reaches the detector does not reflect from the walls. At large distances, the solid angle of the source subtended by the detector is smaller and a larger fraction of the light reaching the detector comes from scattered photons.

By simulating the same geometry in GuideIt, the values of absorption and specularly in both the Tyvek and black paper were varied until the asymmetry results matched the results obtained in the experimental setup. It was determined that the source generation in the simulation had a large impact on the results. While it was assumed that the Teflon tape would have the effect of scattering photons, thereby generating a uniform source with an opening angle from zero to 90 degrees, agreement between experiment and simulation showed that this angular distribution required modification. The best fit was obtained with an opening angle of zero to 24 degrees. This is consistent with the 50 degree viewing angle specified for the LED.

---

<sup>22</sup>Tyvek is a registered trademark of E. I. du Pont de Nemours and Company

With the improvements in source generation, it was possible to further improve the fit between data and simulation, the results of which can be seen in Figure 3.16. For the simulation of black paper a specularity of 0.99, and an absorption of 0.88 was found to fit the data, while for Tyvek a specularity of 0.93, and an absorption of 0.10 are a best fit. An additional improvement could be made to the source generation by creating the source photons over the entire surface of the Teflon tape, in this analysis it was assumed to be a point source.

### Improvements to the Light Collection System

The light collection system of the neutron lifetime apparatus consists of a number of optical elements that transport a photon from the experimental cell to PMTs where they are detected. The previous apparatus was first modeled to benchmark the code using previously collected data. Each of the components are then assessed independently such that the largest losses may be corrected in the design of the upgrade to the apparatus.

Decay electrons interact with the superfluid helium[88] and produce extreme ultraviolet (EUV) photons in a quantity of 22 photons per keV of beta energy. The helium is transparent to its scintillation light, thus these photons propagate isotropically to the

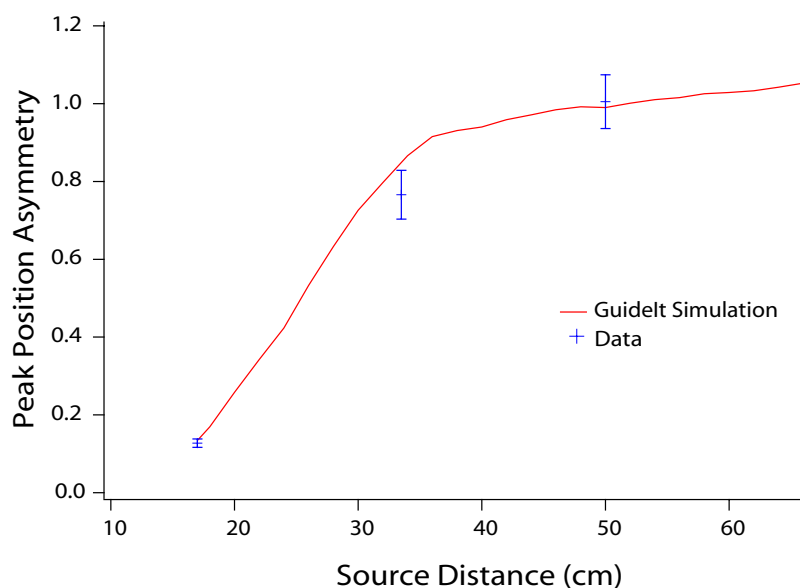


Figure 3.16: The difference in pulse height peak positions for Tyvek and black paper walls, represented as an asymmetry between the two measurements.

inner surfaces of the cylindrical experimental cell. The cell is lined with Gore-Tex with a thin coating of Tetraphenyl Butadiene (TPB) evaporated on its inner surface. This element serves two functions. First, the TPB is an energy downconverter[61, 89], absorbing the EUV photons and emitting visible light photons with an average wavelength of 440 nm, having a fluorescence conversion efficiency of 1.4. This process converts the EUV decay signal to one that may be collected using conventional optics. Secondly, the detector insert acts as a diffuse reflector, transmitting the light to either end of the cell through a series of diffuse reflections.

Photons reaching the downstream end of the cell pass through an optically transparent  $B_2O_3$  boron oxide beam stop, after which they pass through an ultraviolet transmitting (UVT) acrylic light guide. The index of refraction of liquid helium at the operating temperature[90] is roughly 1.029, therefore total internal reflection in the acrylic is the same as if it were in air. Upon leaving the light guide the photons pass through a small gap of liquid helium through a 0.635 cm thick acrylic optical window, and exit the measurement cell.

The remainder of the light collection system consists of an acrylic optical and vacuum window at 4 K, and an additional quartz window in the same location to remove the heat load to this surface from blackbody radiation originating at the 77 K surfaces. An acrylic light guide extends from 77 K to 300 K. In the Mark II apparatus this element was limited in length and therefore required an additional surface of sapphire at the 77 K end to remove the heat load conducted from room temperature.

To more accurately represent the generation of light from the neutron lifetime experiment, a new source creation code for GuideIt was written to simulate a distribution of photons generated from the TPB coating on the cell walls due to a point like interaction in the helium. To do this an initial EUV photon is created at a specified event position within the trapping volume with an isotropic angular distribution. This EUV photon is then tracked to the surface of the cell where the initial position for the simulated visible photon is generated. In this way, the photon source is generated on the inner surface of a volume with a specific probability distribution function. At this new position, the visible photon is reinitialized with a new random direction. Although the mechanics of the down conversion of EUV to visible light is a complex process, the conversion efficiency of the TPB is well understood[61]. Producing the proper position and angular distributions of visible photons is a sufficient initial condition for the simulation.

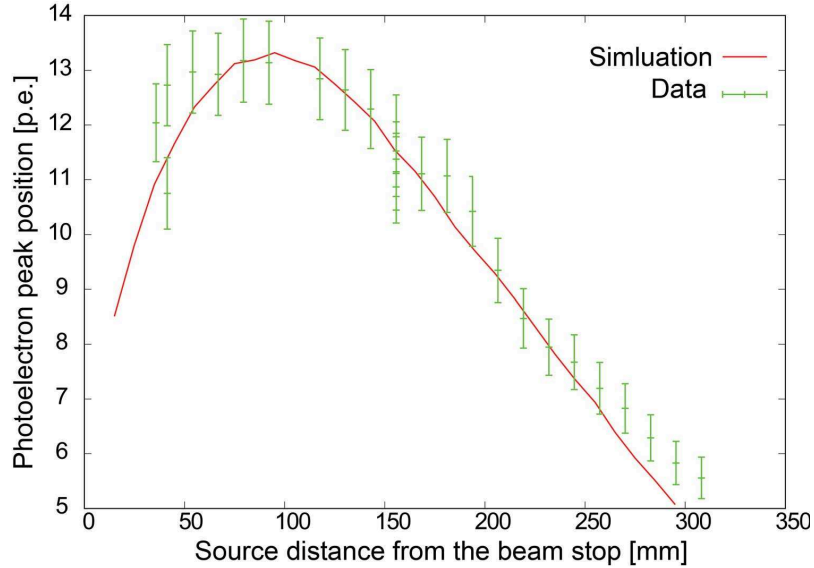


Figure 3.17: A comparison of the simulated number of photoelectrons with the experimental data from the Mark II light collection geometry.

Using this source generation and the new Lambertian diffuse surface detail routine described previously, a light collection efficiency for the guide system of the neutron lifetime experiment was calculated for initial events occurring along the axis of the trap. As the calibration measurements were performed using a  $^{113}\text{Sn}$  source in the previous apparatus, a model of that geometry provided an adequate benchmark to the calculation, and a strong footing from which to base the design of a new light collection system.

The collection efficiency is calculated as the number of photons passing the last surface into the photomultipliers (PMTs) normalized by the number of source photons created. The measured detection efficiency on the other hand is the number of photoelectrons (p.e.) counted in a single PMT on the end of the apparatus for each of the 364 keV events created by the  $^{113}\text{Sn}$  beta source. Details of the elements of the light collection system modeled here are shown in Figure 3.18 and can be found in Ref. [58, 62].

Each beta event is expected to create on average 11,200 visible photons. Additionally, at the peak emission wavelength of the TPB, 430 nm, the quantum efficiency for the PMT[91] is 17 %. After applying the appropriate scaling to the simulation the results are in good agreement with the calibration data taken in the previous apparatus, shown in Figure 3.17.

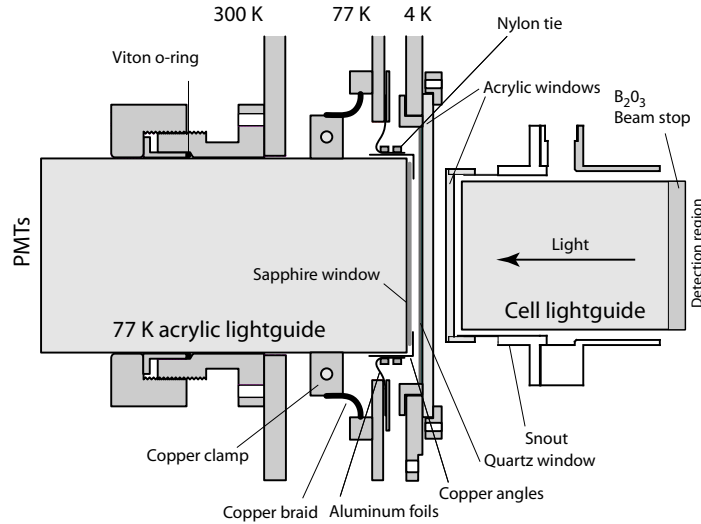


Figure 3.18: Light Collection System from the previous apparatus[62]. Calibration data taken in this apparatus was used as a benchmark for the GuideIt simulation of this geometry.

In addition to the specularity and absorption parameters of the diffuse materials described above, other input parameters for these simulations are the values of the index of refraction, the surface roughness, and the bulk attenuation length for each of the materials. Indices of refraction are needed for calculating both the transmission and reflection probabilities, as well as the refraction angle. The bulk attenuation length is the length for which the intensity is reduced by a factor of  $1/e$ . The surface roughness parameter applies an additional loss at the surface due to imperfect reflections. When dealing with a diffuse surface, the roughness is a redundant parameter and should be set to one, although it was not done in the work described here. Since this mistake was made consistently when both defining and using diffuse reflection parameters, the results are unaffected.

For UVT acrylic[92], the index of refraction for light with a wavelength of 430 nm is 1.5085. Measurements of the attenuation length of acrylic can vary depending on the source of the acrylic, with values in the literature ranging from 111 cm[93] to 751 cm[94]. Here we have assumed 150 cm to be conservative. The acrylic surfaces are polished and so the roughness is estimated to be 0.99. The Burle 8854 PMTs used in the experiment have a window made of UV transmitting glass[91] (Corning #9741 or equivalent) with an index of refraction of 1.48 at 404.7 nm. An approximate value of 300 cm is used for the attenuation

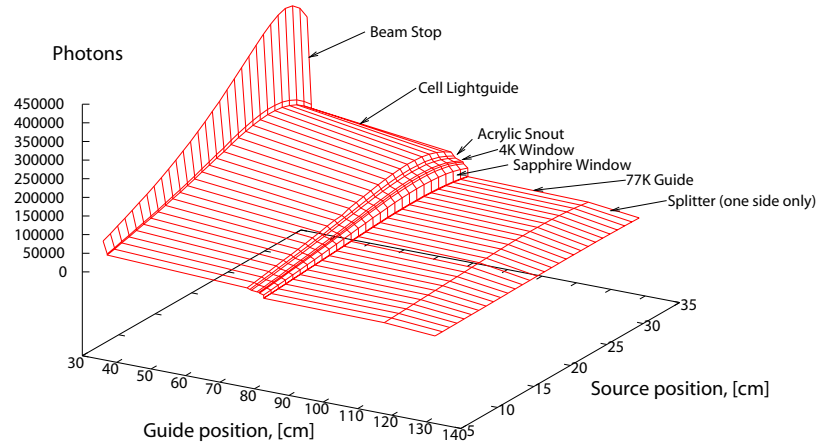


Figure 3.19: A number of photons passing each of the elements of the Mark II collection system for various source positions within the cell. The total number of photons launched initially is 1,000,000.

length of glass. The surface roughness of a cast surface such as the glass window is estimated to be 0.999. The index of refraction of the 4 K quartz window[95, 92, 96] is 1.5538 at 430 nm. The bulk attenuation and surface roughness of quartz are assumed to be like those of the glass PMT window. The sapphire window[95, 97, 96] has an index of refraction of 1.7820 at 430 nm, and the attenuation and roughness of this material are also assumed to be similar to glass. Several values of the index of refraction were found for Boron Oxide, but it is unclear at what wavelength these values were measured. The values 1.459, 1.462, 1.464, and 1.485 have been quoted in Ref. [98], [99], [100], and [101] respectively. These simulations are run with the intermediate value 1.464. Again the attenuation length and surface roughness are assumed to be similar to glass. For more details on the simulation, the commented input file has been included in Appendix A.

Figure 3.19 shows results of the simulation as a function of both position of the  $\beta$  source as well as along the guide position. The region corresponding to each of the optical components from the previous apparatus are labeled. A large loss through any component can be seen as a large change in efficiency through that component. The largest losses are due to the diffuse reflections leading into the beam stop. Two components of the guide system that serve as large barriers to the photons and are not necessary in the redesign are the  $B_2O_3$  beam stop and the sapphire window on the face of 77 K guide. The function of the beam stop was to remove the possibility of radiation damage in the acrylic from

neutron capture. In neutron beams with higher intensity and higher energies of neutrons, color center formation has been observed in acrylic that leads to a discoloration and thus a decrease in the collection efficiency. However, it has been observed in recent tests with cold neutrons of the low fluence and energy used in this apparatus that color center formation in acrylic does not occur. Additionally a sapphire window was included to provide good thermal conductivity for cooling the cold face of the 77 K guide. In the design of the new apparatus the distance between the 300 K and 77 K surfaces was increased to further lengthen the thermal path between the upper and lower temperatures in this element. Based on an ANSYS finite element analysis of the heat flow in the 77 K guide, it is expected that the sapphire will not be needed for sufficient cooling of this longer guide. See Section 3.3.3 for more details on this analysis.

To see how each component affects the efficiency, Figure 3.20 shows the collection efficiency at the end of the 77 K guide as a function of the source distance from the guide for each of four cases: the full geometry of the previous apparatus, the same apparatus with the beam stop removed, the same apparatus with the sapphire window removed, and the same apparatus with both the beam stop and the sapphire window removed. Thus one can obtain a 50 % increase in the light collection efficiency by removing these two elements.

Having completed the benchmark with prior data, a new light collection system was designed without these two elements. As described in Section 3.2, the new trap is both larger radius and longer. Simulation of the new design are shown in red in Figure 3.21. The average gain in photoelectrons per event will be significantly higher. The average photoelectron peak position of the new collection system is a factor of 1.64 greater than the average peak position of the previous apparatus.

In the cylindrical geometry of the apparatus, neutrons enter the cell from one end, while the light is collected from the opposite end. In both the previous and current configurations, there is no means for collecting light that is directed towards the neutron entrance end of the cell. This immediately cuts the light collection efficiency in half. If an optical element could be used to redirect the photons at the neutron entrance toward the light collection end of the cell one might regain some of this loss.

There are two problems in implementing this type of element. First, the types of materials that are good reflectors of light are also typically metallic, which tend to activate when exposed to neutron irradiation thus increasing the number of background events in the experiment. Additionally, any material placed in the upstream end of the experiment must

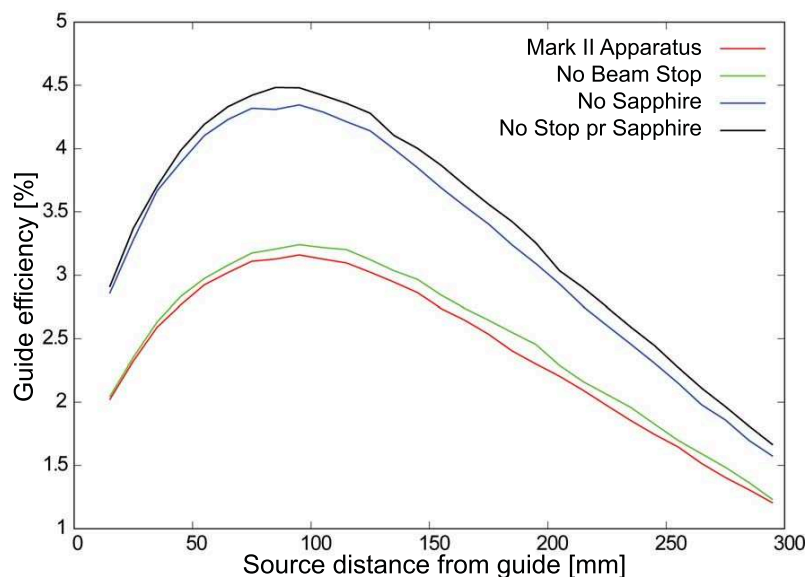


Figure 3.20: The light collection efficiencies in the Mark II apparatus after the 77 K guide. The source position is relative to the closest component of the guide, either the beam stop or the cell light guide if there is no beam stop.

pass neutrons into the cell. If such a reflective material were found that could pass neutrons without generating backgrounds the detection efficiency of the new apparatus would be increased as seen in the blue curve in Figure 3.21.

### Reflective Polymer Characterization

Vikuiti<sup>23</sup> Enhanced Specular Reflector (ESR) is a 65  $\mu\text{m}$  thick polymer film with a reflectivity > 98 % over the visible spectrum. Neutron activation analysis of this material was performed to determine if the material will produce additional backgrounds to the experiment when irradiated with neutrons. Neutron transmission studies were also performed on the Vikuiti ESR material to determine if it is a suitable material to use as a neutron window.

<sup>23</sup>Vikuiti is a trademark of 3M, St. Paul, MN, more information can be found at <http://www.3M.com/Vikuiti>

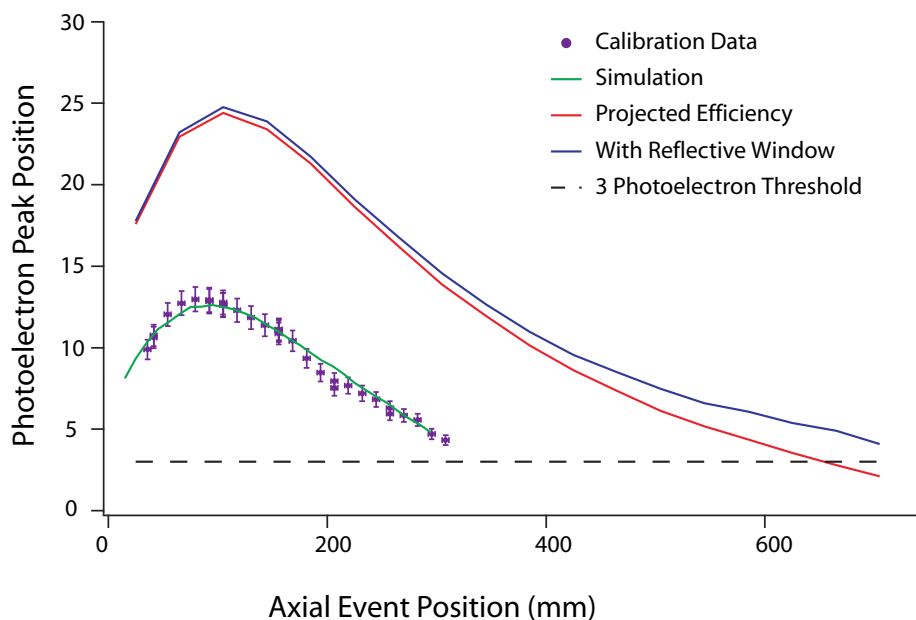


Figure 3.21: Detection efficiency as a function of axial position within the cell. Data from events generated using a  $^{113}\text{Sn}$  line source (purple) confirms the validity of the GuideIt model (green) on the MarkII apparatus geometry, the upgraded geometry of the KEK Trap predicts a significant improvement both with (red) and without (blue) a reflective window as described in the text.

### Activation Studies

Since the elemental composition of Vikuiti ESR is proprietary information, activation studies were performed on the material. A small sample of the ESR material, 2 cm by 4 cm, was placed into the NG-6 polychromatic beamline, first for one minute, then a second time for five. No activation was detectable. This was performed as a precautionary measure in case there was a reaction that created an unwanted radioactive material. When it was determined that there was not any measurable activation, a test was performed to simulate one year worth of neutron exposure. The material was positioned close to the NCNR reactor core using the pneumatic rabbit tubes and was exposed to an estimated fluence of  $1.6 \times 10^{14} \text{ n/cm}^2$ . An estimate of the activated metals are observed using gamma spectroscopy measurements of the activated sample at the 50 % level of accuracy. It is determined that there are 1 ppm  $^{27}\text{Al}$ , 30 ppm  $^{55}\text{Mn}$ , and 20 ppm  $^{59}\text{Co}$ . Using this information and a knowledge of the cross sectional area, flux, and exposure duration, one can extract a number of unstable elements per gram of exposed material,  $N^*/\text{g}$ , produced from

neutron irradiation [67, 102],

$$\frac{N^*}{g} = 5\sigma_{th}\Phi \left( X \frac{N_A}{A} \right) \tau \left( 1 - e^{-t/\tau} \right). \quad (3.12)$$

The factor 5 is result of the  $1/v$  dependence of the reaction cross section of the 8.9 Å monochromatic beam as coupled to the thermal cross section,  $\sigma_{th}$ . The total flux of the 8.9 Å neutron beam,  $\Phi$  is  $4.9 \times 10^6$  n/cm<sup>2</sup>s. For each gram of the material,  $X$ , the mass fraction of the impurity and the ratio of Avogadro's number to the atomic mass of the parent nuclei,  $A$ , gives the number of impurities available to interact with. The number of activated elements may therefore be written purely in terms of the properties of the reaction elements,

$$\frac{N^*}{g} = 1.48 \times 10^5 \frac{\sigma_{th} X}{A} \tau \left( 1 - e^{-t/\tau} \right), \quad (3.13)$$

where the activity, or number of disintegrations per second, may be expressed as  $\dot{N}^* = N^*/\tau$ ,

$$\frac{\dot{N}^*}{g} = 1.48 \times 10^5 \frac{\sigma_{th} X}{A} \left( 1 - e^{-t/\tau} \right). \quad (3.14)$$

Many of the radionuclides with short lifetimes saturate at a maximum activity. Therefore, another interesting rate is the saturated activity that occurs when  $t \gg \tau$ ,

$$\frac{A_{sat}}{g} = 1.48 \times 10^5 \frac{\sigma_{th} X}{A}. \quad (3.15)$$

The number of elements unstable to radiative decays produced by neutron capture or other reactions for a trap loading time of 2500 s has been summarized in Table 3.3.3. Here, the initial decay rate and the saturation activity are given. There is one unstable element produced which may be of concern. The <sup>60m</sup>Co metastable undergoes an isomeric transition with a lifetime,  $\tau_{IT} = 906.3$ , in which it will decay to a <sup>60</sup>Co state by the emission of a 58.6 keV gamma. Since the lifetime is similar to the neutron lifetime, and one expects a signal of 2.3 s<sup>-1</sup> at the beginning of each observation period, it was decided that the gain was not worth the potential added uncertainty. However, as can be seen in Figure 3.21, the detection efficiency for a 364 keV beta is expected to be just slightly above a 3 photoelectron threshold at the position of the reflective polymer. The use of the ESR reflective material can not be entirely dismissed on the basis of added background events, although a critical estimate of the added uncertainty may be necessary.

Table 3.2: A summary of all neutron induced radioactivity identified using the abundances of the impurity metals determined using gamma spectroscopy on the irradiated ESR sample. The mass of the sample is  $m = 0.833$  g.  $N^*$  is the number of unstable elements produced in a single trapping run of 2500 s neutron exposure.  $\dot{N}^*$  is the initial decay rate arising from the exposure.  $A_{sat}$  is the maximum decay rate of the reaction or element.

Element/Reaction	$A$	$\sigma_{th}$ (barns)[102]	$ppm$	$\tau$ (s)[102]	$N^*$	$\dot{N}^*$ ( $s^{-1}$ )	$A_{sat}$
$^{27}\text{Al}(n, \gamma)^{28}\text{Al}$	27	0.234	1	196	0.208	$1.07 \times 10^{-3}$	$1.07 \times 10^{-3}$
$^{27}\text{Al}(n, p)^{27}\text{Mg}$	27	$3.5 \times 10^{-3}$	1	822	$1.25 \times 10^{-2}$	$1.52 \times 10^{-5}$	$1.59 \times 10^{-5}$
$^{27}\text{Al}(n, \alpha)^{24}\text{Na}$	27	$0.61 \times 10^{-3}$	1	77,905	$6.84 \times 10^{-3}$	$8.78 \times 10^{-8}$	$2.78 \times 10^{-6}$
$^{55}\text{Mn}(n, \gamma)^{56}\text{Mn}$	55	13.3	30	13,410	2,040	0.152	0.892
$^{55}\text{Mn}(n, 2n)^{54}\text{Mn}$	55	$180 \times 10^{-6}$	30	$3.78 \times 10^7$	$3.02 \times 10^{-2}$	$8.16 \times 10^{-10}$	$1.21 \times 10^{-5}$
$^{59}\text{Co}(n, \gamma)^{60m}\text{Co}$	59	58	20	906.3	2,050	2.27	2.42
$^{59}\text{Co}(n, \gamma)^{60}\text{Co}$	59	2.0	20	$2.39 \times 10^8$	208	$8.72 \times 10^{-7}$	$8.34 \times 10^{-2}$
$^{59}\text{Co}(n, \alpha)^{58}\text{Co}$	59	$0.3 \times 10^{-3}$	20	$3.89 \times 10^{10}$	$3.13 \times 10^{-2}$	$8.04 \times 10^{-9}$	$1.25 \times 10^{-5}$

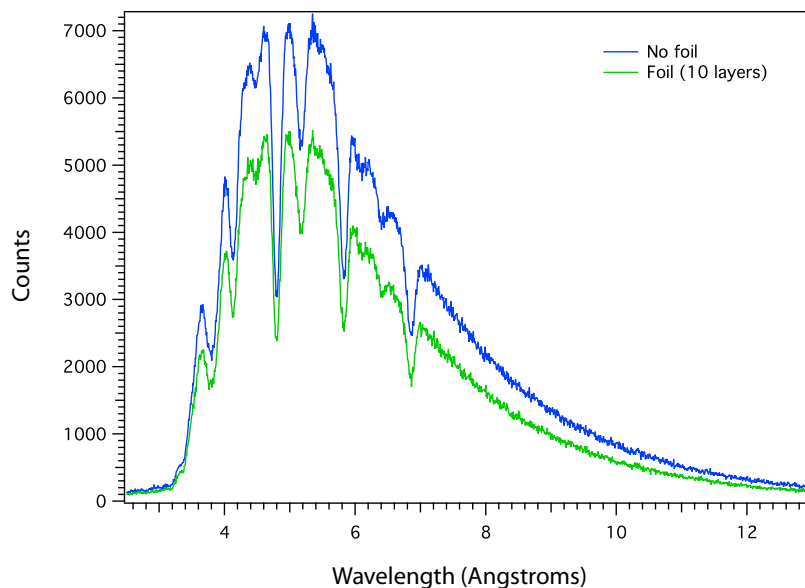


Figure 3.22: Neutron time-of-flight spectrum of the NG-6 polychromatic beam both with (green) and without (blue) the reflective polymer stack in the beam.

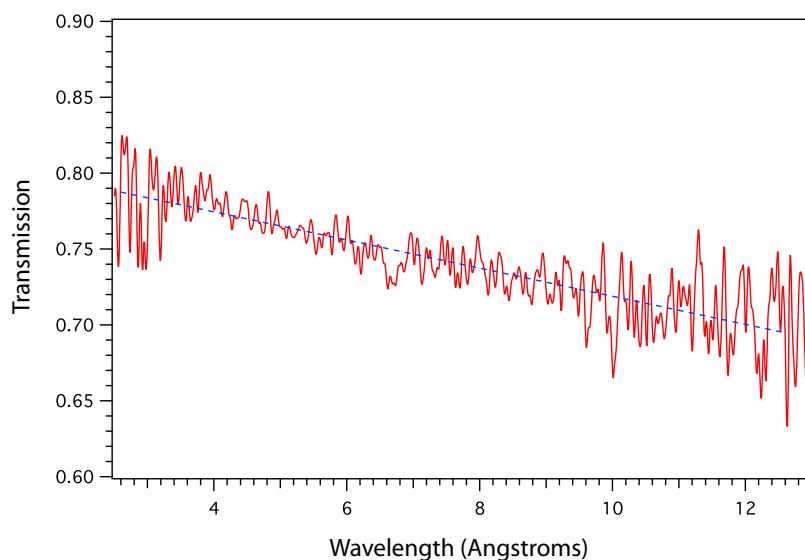


Figure 3.23: The normalized difference of the two spectra (red line) shows the characteristic  $1/v$  dependence, the fit is represented by the blue line. This measurement was made with a stack of 10 reflective films.

### Transmission Studies

Another function of a reflective window in the neutron entrance to the cell is the transmission of neutrons. Material will scatter neutrons based on their scattering cross

sections with a  $1/v$  dependence. The transmission studies were performed using the polychromatic neutron beam exiting the NG-6 beamline. Ten samples were stacked together to provide a sufficient thickness for attenuation. The neutron time-of-flight energy spectrum was measured using a rotating wheel chopper to pulse the neutron beam. Measurements were performed both with and without the polymer reflector in the beam. The results of the time-of-flight spectra are shown in Figure 3.22. The energy dependent measurement allows one to determine the transmission at the wavelength used for neutron production in superfluid helium,  $\lambda = 8.9 \text{ \AA}$ . The energy dependent measurement allows one to verify the  $1/v$  absorption as a test of the technique and to determine the transmission at any given energy. The difference of the spectra at  $8.9 \text{ \AA}$ , normalized to the average of the spectra, gives the percentage of neutrons that will be lost in this material. The normalized difference is shown in Figure 3.23. The measured attenuation was 2.7 % for one layer of the material.

### 300 mK Optical Window

There is a significant difference in the coefficient of thermal expansion (CTE) of materials that make good low temperature vessels for superfluid helium, typically a metal, and the materials which make good optical windows. These are commonly either ceramics with low thermal expansion, or plastics with high thermal expansion. Since ceramics are generally brittle and more likely to fracture under the high stresses created by this mismatch in thermal expansion, acrylic was chosen as the optical window material. Aluminum is chosen as the mating metal as it has a relatively low Young's modulus, and therefore exerts less stress on the joint at low temperatures.

The basic idea is to create a joint in these materials along a cylindrical geometry. By mating the surfaces with the acrylic (CTE  $6.8 \times 10^{-5} \Delta\text{m/m K}$  at 300 K) on the outside of the aluminum (CTE  $2.2 \times 10^{-5} \Delta\text{m/m K}$  at 300 K), the forces on the joint will be inward holding the joint together as it is cooled. The aluminum section is a flange that mates with the cell using an indium seal. The circular cylindrical cross section is as thin as possible in the joint region and is longer than in the previous design to further minimize stress on the joint. The acrylic section is a machined cup shaped window to reduce the number of glue joints required.

The joint between the aluminum and acrylic was made with Emerson & Cuming

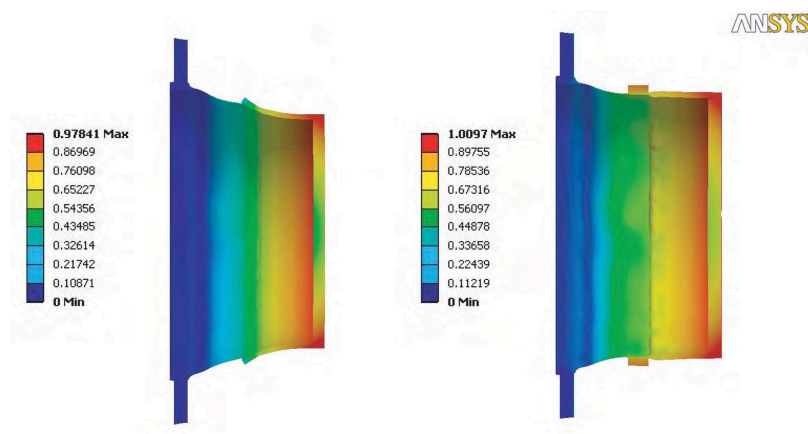


Figure 3.24: Finite element analysis of the thermal expansion mismatch in the cell optical window shows peeling of the acrylic can be relieved with additional Delrin rings. The color scale represents the strain in % of  $\Delta L/L$ .

Stycast 1266 epoxy<sup>24</sup>. The clearance between the two pieces was machined such that there was very little gap, and the aluminum slid tightly inside of the acrylic. The adhesive is quite thin when mixed, and wets both surfaces by capillary action. If cured at an elevated temperature the glue thins further, and might leak out of the joint further. For this reason the glue was first cured for an hour or two at room temperature.

The annealing schedule for acrylic was then followed. In an oven with a computerized control a ramp schedule was programmed to take the window up to about 80 °C (low enough to avoid deformation of the acrylic) in about 4 hours. The temperature was taken back to room temperature in nearly 8 hours. This had two benefits. The acrylic was machined and therefore annealing it relieves residual stresses that could cause it to warp or fracture at low temperatures. Additionally, it is recommended to cure the adhesive at elevated temperatures to fully form all cross-links in the epoxy making a stronger bond. The final step in production of the optical window was to have the faces polished, for this we are indebted to the NIST optical shop.

The joint was modeled during a cooldown using ANSYS finite element analysis. From this it could be seen that the joint had the tendency to peel up at the end of the acrylic. To counter this action a ring of Delrin<sup>25</sup> (CTE  $1.1 \times 10^{-4} \Delta m/m K$  at 300 K)[70]

<sup>24</sup>Supplied by Ellsworth Adhesives

<sup>25</sup>Delrin is a DuPont trade name for an acetal polymer.

placed around the outside of the joint was shown to improve the contact along the joint. In an attempt to further reduce the taper in the aluminum cylinder, thus relieving even more stress on the joint, an additional sleeve of acrylic and Delrin that are not physically attached to those shown in Figure 3.24 is placed nearer to the flange end.

### 77K Guide

The longer distance between 77 K and 300 K on the light collection end of the new horizontal cryostat creates a longer thermal path into the light guide than in the previous cryostat. Assuming the thermal conductivity of acrylic is 0.19 W/mK at room temperature and 0.16 W/mK at 77 K, an ANSYS finite element model was used to optimize the boundary conditions created by thermal clamps for the light guide which generate the thermal gradients from one end to the other. Two flanges were precisely machined to have an inner diameter smaller than the outer diameter of the acrylic rod in order to ensure the full thermal contact at 77 K and a vacuum seal at 300 K. The rod was then cooled to 77 K such that thermal contraction allowed it to slide through the room temperature flanges. However, upon simultaneous cooling of the aluminum and the acrylic, the dimensions are such that full contact of the mating surfaces will remain until temperatures are well below 77 K.



Figure 3.25: Photograph of the 77 K light guide element. Photon signals enter from the right in this picture, and exit toward the PMTs on the left.

Upon repeated vacuum, and cooldown cycling this guide element has reliably performed its functions.

### 3.4 Experimental Procedure

The operation of the apparatus can be understood by following the neutrons and their decay products. Neutrons enter the apparatus from one side, some of these are scattered to near rest where they may be trapped. Those neutrons above the trapping threshold are ejected from the trap by a magnetic field ramping procedure. Decay events from fully trapped neutrons are then observed as the recoil beta deposits energy in the liquid helium and produces scintillation light. The scintillation light is transported out the other side of the apparatus and detected by PMTs. The prompt capture reactions when the neutron beam is on produce significantly more light than the neutron decays, so the experimental schedule is divided into three time periods, a trap loading period, a magnetic field ramp, and an observation period.

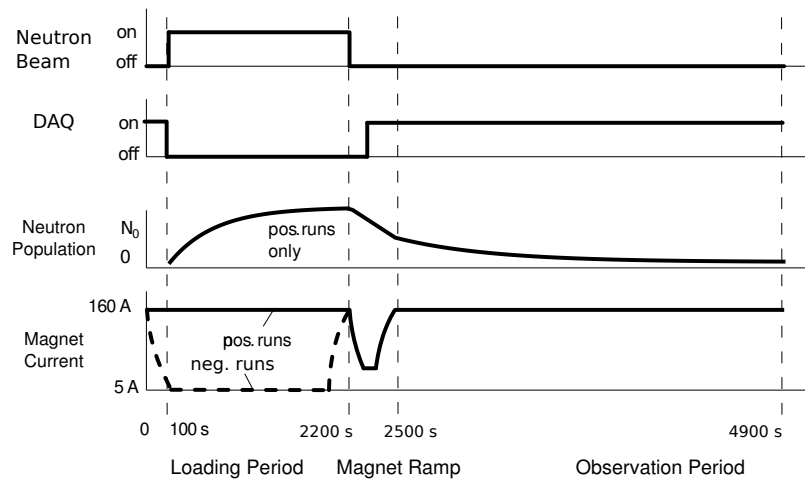


Figure 3.26: A time line of the major events during the run schedule. The run schedule is divided into three time periods; trap loading, magnetic ramp and observation.

At the beginning of the trap loading sequence the bias voltage on the PMTs is lowered, zeroing their gain in order to prevent damage from the large amounts of light from capture events. The trap loading begins as the beam shutter is moved into the open

position<sup>26</sup>. Additional shielding materials on a ‘slider’ table will be moved from a position where they block the view of the beam and into a position in which a flight tube<sup>27</sup> around the beam will pass neutrons. The population of neutrons will increase according to

$$N = R\tau_n \left(1 - e^{-t/\tau_n}\right) \quad (3.16)$$

until it reaches its theoretical maximum value,  $N_{max} = R\tau_n$ . Since the production of neutrons approaches its maximum with the same characteristic time as the neutron decay, the loading and observation periods take a similar fraction of the total run schedule.

At the end of the loading period the ‘inner’ shutter is closed and the slider table is moved into its background blocking position. At this point a magnetic field ramp is performed as described in Section 4.2 in order to remove neutrons above the trapping threshold. The PMTs are energized and the data acquisition begins.

During the final period a photoelectron signal is observed which has multiple sources. The component of the signal due to neutron beta decay is only a fraction of the observed signal. In the previous apparatus this ratio was roughly 1/12 at the beginning of the observation period. There are both constant and time varying components to this background. A fit to the raw data can be performed in attempt to identify each of these components, however there is a loss in sensitivity for each additional fit parameter introduced. Instead, the method adopted to analyze data from the previous apparatuses has been to perform two different run schedules, ‘positive’ and ‘negative’ runs. In the positive runs the trap loading phase progresses with the magnetic trap fully energized. As neutrons downscattered by the superthermal process, the UCN are trapped by the magnetic field gradient. In the negative runs however, the trap is not energized during the trap loading phase. In these runs UCN are produced, but they are not trapped and can reach the surfaces of the experimental cell where they are captured in the shielding materials with high probability. At the end of the loading period the magnets are energized, and the rest of the procedures are identical between the two types of run. Since all other conditions are the same, the only difference between the runs is the presence of neutrons in the trap, and the difference in the observed signals gives a neutron decay signal that may be fit using only one parameter.

---

<sup>26</sup>There are actually two shutters on the NG-6U beamline, one that can be controlled by a voltage signal from the data acquisition system, while the second shutter is manually controlled.

<sup>27</sup>A shielded tube preventing the air scatter of neutrons into the local area of the lab.

A test of this background subtraction can also be performed. After sufficient lifetime data has been collected one can ‘poison’ the experimental cell with  $^3\text{He}$ . This is accomplished by running the experiment with natural abundance helium with  $^3\text{He}/^4\text{He} \sim 10^{-7}$ . Since  $^3\text{He}$  has an absorption cross section of 5333 barn, natural helium results in a trap lifetime of  $\tau_{\text{trap}} \approx 1$  s. The difference between the ‘positive’  $^3\text{He}$  runs and the ‘negative’ runs has been shown to be consistent. Further analysis of the systematic effect from contamination of the isotopically pure helium can be found in Section 4.1.

## 3.5 Data Acquisition System

The data acquisition system is responsible not only for recording data, but also for monitoring the function of the various parts of the apparatus and controlling the prescribed run schedule.

### 3.5.1 Data Collection

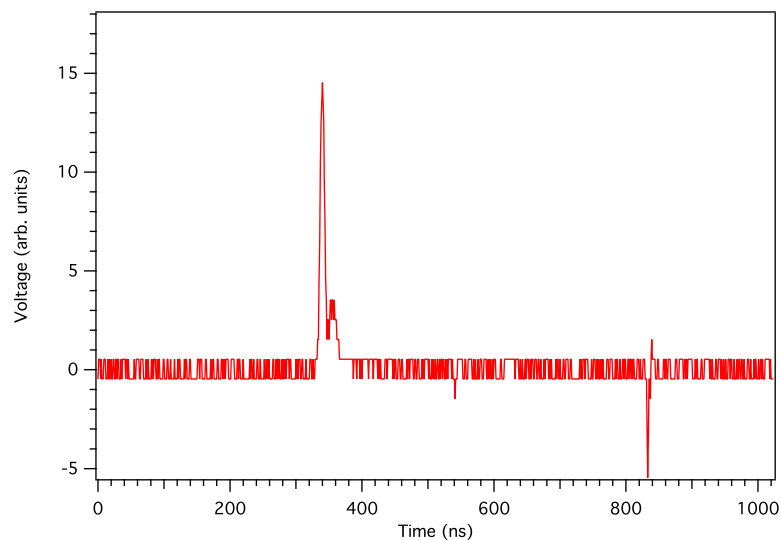


Figure 3.27: The digitized waveform of a typical PMT pulse.

One major function of the DAQ is the systematic collection of data. For this, a GaGe CompuScope 82G digitizing card has two channels with a sample rate of 1 gigasamples per second each. A trigger event occurs when a pulse is detected in both PMTs. This signals

two channels of the 8-bit waveform digitizer to generate digital waveforms from the input PMT signals. Each waveform will consist of a predetermined number of samples, somewhere between 128 and 1024, at a rate of one per nanosecond. Typical photoelectron pulses are 20-40 ns long, the remaining samples are used to establish a baseline. A typical waveform from the background run described in Section 3.6.4, is shown in Figure 3.27.

While the recorded waveforms can be used to help identify beta events, they will not provide a measure of the decay rate. For this the trigger is also sent to a counter, a part of a low-level digital I/O board<sup>28</sup> that generates the timestamp for the start of the digital waveform using an external 10 kHz clock. The timestamp resolution is 100  $\mu$ s. By adding an unknown scale factor to the timestamp, the data will be blinded for analysis.

The DAQ is also responsible for the recording of secondary data. This data is not a result of the neutron lifetime measurement, rather it is a monitor of the functions of the magnets and the cryostat. Specifically the DAQ monitors all of the sensors placed within the apparatus. This is mostly for diagnostic purposes, but can additionally be added as feedback for additional control structures. Silicon diode temperature sensors<sup>29</sup> which are sensitive in a range from 1.4-500 K are installed in various places of the apparatus, including both 77 K and 4 K locations near the neutron entrance windows, and light exit windows. They are placed along the copper bar under the 4 K section of the horizontal cryostat, and on the support feet at both stages. Diode sensors on the magnet leads allow monitoring of the resistive heating, as well as monitoring of the cell cool-down. Below 1.4 K the cell temperature is monitored using well calibrated RuO<sub>2</sub>, and Bi<sub>2</sub>Ru<sub>2</sub>O<sub>7</sub> resistors with a four-wire resistance bridge. While voltage taps on the magnets, and the current leads are primarily used as inputs in the quench detection circuitry. They may also be monitored for diagnostics, and additional feedback loops. For example monitoring the copper sections of the current leads could be used in a control loop for control of the liquid nitrogen flow to the leads improving consumption of this cryogen. A primary benefit to the automatic monitoring system is that it will be capable of notifying a worker of problems via text messaging, or a telephone call. This ensures an immediate response when critical temperature or pressure thresholds have been crossed.

---

<sup>28</sup>Measurement Computing PCI-DIO48H/Ctr15 digital I/O + counter

<sup>29</sup>Lake Shore Cryotronics, Inc., Models DT-470, and DT-670 were used.

### 3.5.2 Control Functions

The other major function of the DAQ is to control all of the operational parameters of a run. There will be adjustable ramp/soak type configuration for the magnets, controlling the level of the magnetic fields for each of the experimental periods and the ramp rates between these levels. Digital voltage levels control the positions of the slider table, the “inner”-shutter control, as well as the PMT bias voltages. An LED pulser used for phototube gain stabilization<sup>30</sup> is both controlled and synchronized with the data collection such that the resulting signal can be later removed from the data. Heaters on the top of the current leads dewar will also be controlled. These heaters are installed on the top flange to increase its temperature above the dew point. This reduces ice build-up on the flange and the current leads eliminating the potential for shorting the leads. Active control of these heaters is required because the current through the magnet leads modifies the heat load on this top flange.

The remote control of the power supplies for the trap magnets is a 0-5 V analog signal. This is calibrated to represent the actual current with feedback verification on the second time scale. The two power supplies<sup>31</sup> for the solenoids and four power supplies for the quadrupole are controlled in master-slave mode using two direct GPIB communication, and are independent of each other. The supply for the compensation magnets is controlled, using a 1-10 V analog signal, simultaneously with the solenoid power supplies in order to maintain compensation at all fields. Since the planned operation of the solenoids will provide a static field throughout the run cycle the current ratio,  $i_S/i_C$ , is set for optimal compensation of the trap fields for maximum solenoid operating current only, and ramped between zero and these values linearly.

In order to energize the quadrupole magnet each of the SCR's,  $S_{1-4}$  in Figure 3.5 of the quench protection circuit must be latched. Since they may be started in conducting mode only after the voltage across them surpasses a threshold, they are latched successively as the current is ramped up. TTL logic is used to switch a solid-state relay<sup>32</sup> (SSR) that controls the SCRs, as shown in Figure 3.28. The logic signal from the DAQ triggers a 2N3904 NPN pull-down transistor in a loop with a 9-volt battery to close the SSR switch. Thus the SSR applies the voltage from a 3.3 V power supply to the SCR gates, switching

---

<sup>30</sup>Further discussion of the gain stabilization can be found in Section 4.3.

<sup>31</sup>Agilent (Née Hewlett Packard) 6681A (solenoids), and 6680A (quadruple).

<sup>32</sup>Cryodrom DMO063

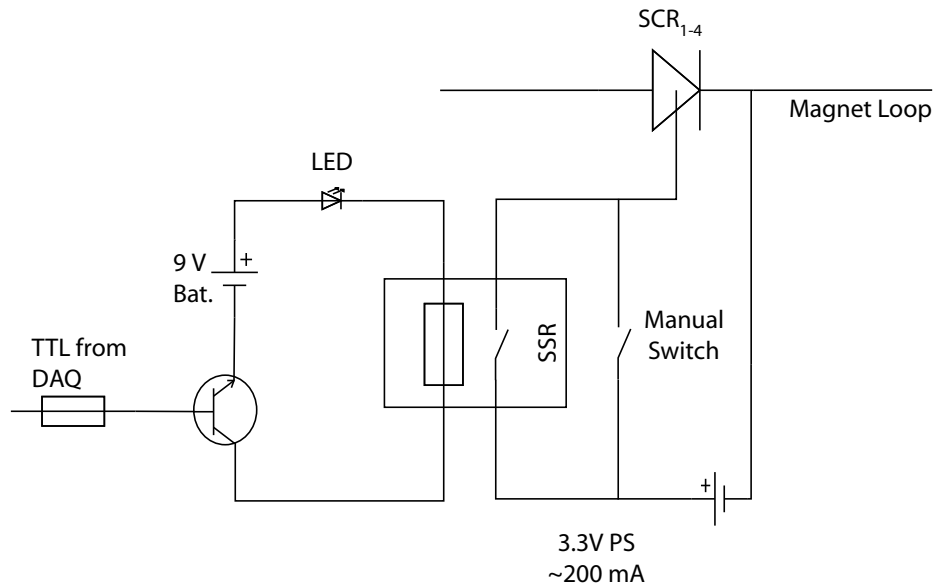


Figure 3.28: The DAQ interface with the SCRs to energize the magnets.

it into a conductive state. Fully energizing the magnets entails monitoring the voltages across the SCRs and latching each SCR in succession once the current is high enough to maintain conduction. After all SCRs are switched to a conducting state, but before the magnet is fully energized, the DAQ should simulate a quench signal, triggering the dump SCR to verify that the SCRs switch back to their non-conductive state. This is done at a fairly low current so that the transfer of stored energy in the magnets to the dump resistor does not cause a quench of the magnets. After passing this test the SCRs are once again run through the latching sequence, and the magnet is ramped to the specified current.

Additionally three prominently displayed push-buttons were installed to create manual controls for rapid safety related responses. A red push-button, removes the inhibit signal from the power supplies, starts a blue ‘magnets-energized’ strobe, and allows the DAQ control of the magnets. The magnets may be ramped down in a controlled manner by pressing a yellow push-button, and emergency stop which zeros and inhibits all power supplies is controlled by pressing a green push-button.

## 3.6 Apparatus Performance

The commissioning of the new apparatus has taken place in several stages. We received the new sections of the cryostat from the manufacturer in July of 2007. After assembling the dewars without modifications or installation of the magnet we performed an initial cooldown to check for cold leaks, and measure the cryogen boil-off.

Stage II consisted of making all of the necessary modifications to the dewars. This included modifications to the end flanges to allow for a beam entrance, and a light collection system. Inner vacuum chambers were added to either end of the horizontal 4 K helium vessel with a tube through the center of the magnet bore to connect these chambers and provide space for the experimental cell to be supported within the trapping field. Bellows on either end of the IVC tube allow for thermal contractions along the length of the 4 K vessel. This vacuum space was connected with the IVC in the fridge through a series of bellows. Also a task for this commissioning phase, the magnetic trap was inserted into the dewar. This was a procedure which required tipping the horizontal sections on end, and lowering the trap in vertically with a crane. Suspended by a spreader beam about rotating hoist points at its center of mass, the horizontal section of the cryostat can be rotated from horizontal to vertical for this operation. The magnet is rigidly supported by several points around the diameter of the 4 K bath volume. Once in place underneath the vertical sections, connections were made between the buffer cell of the dilution fridge and the experimental cell. This phase did not however include any of the cell insert materials or windows. Blank stainless steel flanges sealed the cell volume to remove any complications of these windows.

The cooldown of this stage occurred during August 2008. A first training of the magnets was attempted during this cooldown, in which we saw the first quench of the trap in a horizontal configuration. Subsequent quenches were not, however, possible as the helium exhaust from this quench broke a seal on the cryocooler in the vertical tower which supports the magnet leads. Without this element it is not possible to keep the HTS leads sufficiently cold, and further running of the magnets was not possible during this cooldown. Fixing of the seal required purging of the cryocooler to remove any contaminants in the gas which could freeze and cause a failure. This is accomplished by running the cryocooler to accumulate the impurities in the cold head, then after disconnecting the coldhead from the compressor it is allowed to warm back to room temperature. The impurities are then purged from the system. Before the cryostat was brought back to room temperature for

this operation, several liters of natural abundance helium was condensed into the cell to further test the functions of the experimental cell and dilution refrigerator.

Stage III of commissioning is the full buildup of the apparatus, with a goal of operating and taking data. The experimental cell was built with all of the insert materials. A Teflon window at the neutron entrance and the acrylic light collection window were installed. The neutron flight path into the apparatus was defined by the BN shielding material. Although the changes in Stage III were significantly less than those of Stage II, several system malfunctions impacted the schedule.

A leak between the magnet helium bath to the OVC opened up, however it exhibited diode like behavior. The leak was only present when the bath was at a higher pressure than the OVC. The typical method for finding leaks employs a mass spectroscopy measurement of the exhaust of a vacuum system. When a small concentration of helium gas is placed in front of the leak it can be measured in the exhaust. Since this leak was only opening from the inner helium volume to the outer vacuum chamber when that chamber was under vacuum, this leak was nearly impossible to pinpoint. Eventually, a finite element analysis of the dewars led us to believe the helium volume was designed with too few bolts on the sealing flange. Bolts made from A286, a special alloy of stainless steel with a high tensile strength allowed more pre-stress to be applied to this seal solving the problem.

Further, a failure of the IVC tube required the replacement of that component. A task which required the removal of the magnet. Since there are few options for sizes of stainless steel piping for this purpose, a pipe was purchased with an outer diameter slightly larger than the magnet bore. The outside of this pipe was turned down in a lathe to fit the bore. Not a perfectly straight section of piping, the first IVC tube had a very thin spot which eventually buckled inward making it impossible to support the cell without contacting the tube. Though the second tube was also not perfectly straight, the outer diameter was machined such that the material was taken from many parts of the cell, rather than from one place as it had in the previous attempt. In this way the thickness is not expected to be less than 1.59 mm (1/16"), in any place.

In October 2009 the apparatus was successfully brought down to 4 K. During this cooldown many important milestones were met. The compensation for the magnetic fields was optimized for the "Spin-Echo" spectrometer within a level of acceptability. The magnets were run and the quadrupole ramping was performed for the first time. During this testing an unexpected quench occurred which was successfully detected and protected

by the protection system. Also a modification to the helium exhaust redirecting it away from the cryocooler functioned properly, and the magnets were energized successfully after the quench occurred. A superfluid leak in the cell prevented the liquifaction of isotopically pure helium. Taking data is therefore contingent upon the solution for this.

### 3.6.1 Cryogenics

The performance of the cryostat is assessed by comparing cryogen boil-off rates with the values estimated when designing the cryostat. The calculation of heat loads gives an estimate of about 4.7 W heating of the 4 K vessel, this is equivalent heat load will cause helium to boil at a rate of 156 L/day[58]. The sources of heat input for this estimate are from blackbody radiation, eddy current heating in the solenoids, cryogenic post conduction, conduction to room temperature in the towers, operation of the fridge and input from the current leads. If the cryocoolers are used to their full potential, they provide 1.5 W of cooling power each at 4 K. With this additional cooling the boil-off rate can be reduced to about 60 L/day.

In the first cooldown with no modifications, and also no cryocoolers installed, a boil-off rate of 100 L/day was observed. This is consistent with the estimates, for which an additional 50 L/day is expected from the current leads, and 5 L/day from the light guides, and neutron entrance windows. In the subsequent cooldowns the boil-off rate was 60 L/day from the magnet bath with both cryocoolers running. During this measurement an additional a boil-off rate of 24 L/day was observed from the bath surrounding the dilution refrigerator. The operation of the magnets in the October 2009 cooldown did prove to increase the boil-off rate from the magnet bath to 100 L/day. Therefore the total boil-off rate while the magnets are energized is expected to be 124 L/day. To reduce the helium consumption, a reliquifier plant<sup>33</sup> was purchased that can recover an additional 30 L/day. This will reclaim the boil-off from the refrigerator bath, making that system effectively a closed system. Although the helium boiling rates are somewhat high, adding both cost and labor to the operations of the experiment. This is still a manageable rate as liquid helium is supplied in 100 L dewars, therefore the experiment can be run with only one liquid helium transfer required each day.

---

<sup>33</sup>Model LHeP18, purchased from Cryomech, Inc. Syracuse, NY

Table 3.3: Status of the magnets at initiation of each of the quenches.

	Quench 1	Quench 2	Quench 3	Quench 4
KEK magnet current (A)	2700	2950	2800	-19A/s
Percentage of design current	79%	87%	82%	80%→24%
Solenoid Current (A)	190	210	199	188
Percentage of design current	84%	93%	88%	80%
Quench Initiation	Not known	KEK		
Trap Orientation	Vertical	Vertical	Horizontal	Horizontal (Ramping down)

### 3.6.2 Magnets

When operating superconducting magnets, training exercises may be necessary after any operation which could cause a shift in the wires or in the fields they are exposed to. For example, this is expected when changing the configuration of the magnet, as the magnetic fields the conductors are exposed to will change orientations. However in some cases even just moving the magnet will modify the stresses on it requiring additional training. Furthermore, ramping the fields of the magnet will generate additional stress on the wires which may cause unexpected quenches.

The magnet trap, KEK quadrupole and two solenoids, has been fully energized twice in a vertical orientation, and twice more in the horizontal configuration of the newly constructed cryostat. There have been a total of three planned and one unplanned quench which have all been successfully protected. The KEK magnet has been trained in stand alone operation, however some training may be necessary since the configuration was changed when the solenoids were added to create a trapping field. The field was ramped up until the magnet quenched twice in a vertical test dewar before the final cryostat was built. One of the main purposes of stage II of the commissioning of the lifetime apparatus was to train the magnet trap. However due to the cryocooler malfunction, only one quench was initiated. As there is a risk associated with each quench of the magnets, it was decided that there would be more benefit from operating at a lower current to take initial data before a training the magnets to their full potential. For this reason the collaboration proceeded to the final stage of commissioning. The plan became to run at 80% of the design currents, a level at which no quenching had been observed.

During a cooldown in which we had planned to take initial data, the magnet

ramping was tested. The goal was to ramp the quadrupole magnets between 80% and 24% of the designed currents in 200 s. At this rate the magnets were well behaved, and it was seen that the inductance was not limiting the ramp rate at this level. Therefore the time for this ramp was reduced until it was performed in 100 s, a rate of 19 A/s at which point the magnets did quench. After a successful protection of the magnets, further optimization of the ramp rates were determined. The ramp up will be possible in an average time of 150 s, while ramping down can happen a little faster, with an average time of 125 s.

### 3.6.3 Shielding

Since the statistics are limiting the uncertainties of this experiment, the background signal plays an important role in the overall precision which is obtainable in this lifetime measurement method. Therefore it is important that we shield the apparatus very well from high energy gamma, and fast neutron events originating from the reactor, or from nearby instruments which tend to facilitate background producing reactions. These events may cause false signals in the detection region leading a constant rate of background events. Additionally, these along with the neutron beam which is within the apparatus may cause activation of the materials surrounding the apparatus, creating a background signal which is time dependent on the order of the measurement time scales, 0-8000 s. In Section 3.4 there is a discussion on the background subtraction technique utilized that will further suppress the effect of backgrounds on the measurement.

In Section 3.3.1 the shielding from the neutron beam within the apparatus is described. In order to shield from backgrounds originating outside of the experiment, a study was first conducted to assess the source of backgrounds[103]. A NaI detector was used to collect gamma spectra at three locations in the experimental hall. Directionality was found by building a small lead hutch around the detector with a 4.5 in by 6.5 in hole in one side. This side was aimed in each of the compass directions, as well as in the directions of each of the beam ports. The results relative to the maximum background are shown in Figure 3.29 for the number of counts collected in 10 minutes.

From this data it is clear that special attention should be focused on shielding the neutron entrance and the south side of the apparatus that faces the reactor. For this a wall was constructed on the south side of the apparatus, and a similar one is planned for the neutron entrance end of the apparatus. There are 10.16 cm (4") total of lead shielding in

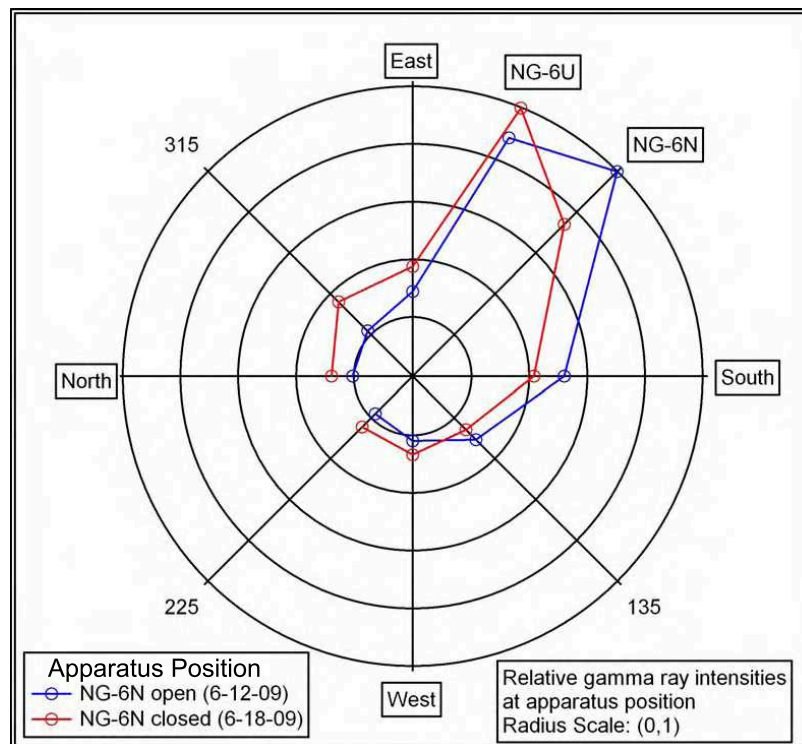


Figure 3.29: The relative directional dependence of the backgrounds, normalized to the maximum rates[103].

the wall, constructed from two 5.08 cm (2") thick layers which have been offset from one another such that there are no gaps between bricks that run the entire thickness of the wall. On the outer side of this wall is placed a layer of boroflex neutron shielding material, and a layer of polyethylene plastic to act as a moderator for fast neutrons. Therefore any fast neutrons incident on the apparatus from the direction of the reactor will first see a layer of moderator slowing them to the extent that they may then be captured on the boroflex shielding material. The  $^{10}\text{B} + n$  capture process will produce 480 keV gammas which are then absorbed in the lead wall with an extinction factor[104] of  $1.56 \times 10^{-9}$ .

### 3.6.4 Background Studies

During a cooldown attempt in March 2010, a full installation of the detectors implemented with a minimal DAQ allowed initial background measurements to be taken. The detectors had a view on the cell which had been cooled to 77 K. The shielding wall on

the south side of the apparatus had been constructed as described in the previous section. The additional wall which shields the east beamline facing side of the apparatus was not yet constructed. The reactor was operating, and while both NG-6U, and the NG-6 endstation remained closed the NG-6M beamline was being used. An LED pulser was installed to study gain differences in the PMTs and had a variable amplitude to study the full phase space of the detectors.

A single photoelectron (p.e.) event in a PMT tends to have the same pulse height, and multiple photoelectrons tend to produce pulse heights in multiples of this. Binning the pulse heights of PMT events, one will therefore observe peaks in the low height limit which correspond to these average p.e. peak heights. This can be seen in Figure 3.30. In this low energy limit however the peaks are often obscured by noise from thermal emissions, ground loops or from other background sources. The simplest background cut to make is a lower level threshold. It was shown in the previous apparatus[62] that the requirement of 3 or more p.e., in each PMT eliminates a large fraction of the background events. The

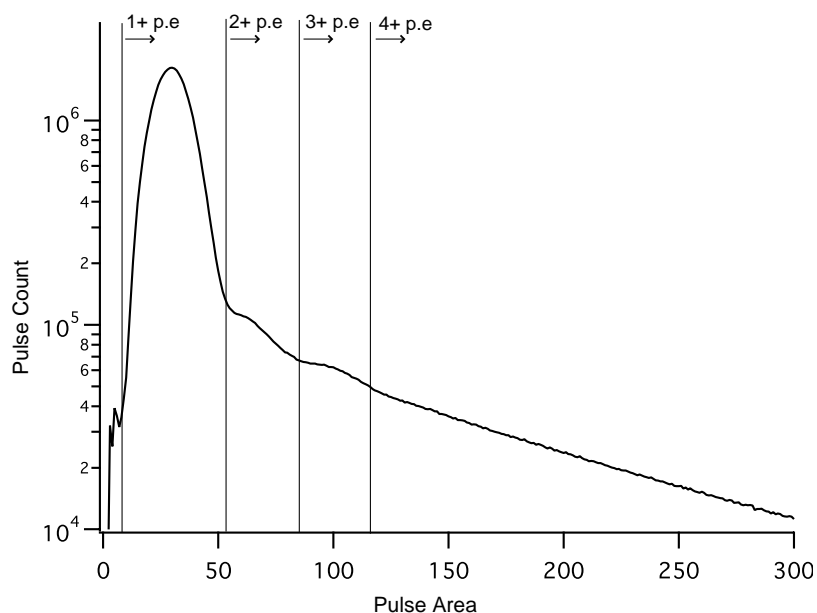


Figure 3.30: The pulse height spectrum from PMT  $\beta$  data in the MarkII apparatus. The pulse areas are calculated from 358 positive runs. The first 4 p.e. peaks, and thresholds are shown.

simulations of the light collection system suggest that events within the cell will have longer collection times, on the order of nanoseconds, than the background events in the acrylic.

This means that additional background subtraction might be possible using pulse shape discrimination in a post analysis of the data. Since the digitizing card used is faster than in the previous apparatus this possibility may be realized. While recording data from an LED pulser it was seen that events originating from the pulser could be easily identified when plotting pulse height versus rise time in the detector. These events were significantly slower than the background events which are most likely originating in the acrylic. Furthermore, the digitized waveforms allow for the final threshold and background subtraction cuts to be made in a methodical manner in a post process analysis.

An estimate of the effectiveness of the external shield wall comes from the background rate measured in the PMTs while the reactor was on and the cell was empty. A single p.e. peak was found in a background measured in the detectors for a duration of one hour. An estimate of the 3+ p.e. lower threshold cut suggests an average background event rate of 23-28 s<sup>-1</sup> with an empty cell. The uncertainties are estimated by scaling 10% of the peak width of the measured 1+ p.e. peak.

One source of background is expected from cosmic radiation producing muon showers that travel through the acrylic light guides in the apparatus. The light guides generate a false signal from the Čerenkov light produced as a muon passes through them. Using the cos<sup>2</sup> θ angular distribution of the intensity, and the cylindrical geometry of the acrylic, the muon flux can be shown to be[105],

$$\phi_{\mu} = \frac{A_{acryl}}{2} (J_1 + J_2). \quad (3.17)$$

Where the horizontal flux is represented by  $J_1 = \int I \cos \theta d\omega$ , and the integrated flux by  $J_2 = \int I d\omega$ . Values for these have been measured[106]:

$$J_1 = 0.0132 \text{ cm}^{-2} \text{ s}^{-1}, \text{ and } J_2 = 0.0174 \text{ cm}^{-2} \text{ s}^{-1}. \quad (3.18)$$

The cross sectional area of the acrylic in the detection system is  $A_{acryl} = 1536.5 \text{ cm}^2$ , from this calculation one can estimate a background rate of 23.5 hz from cosmic events in the acrylic. Since this is a large fraction of the measured rate at a threshold of 3 or more photoelectrons in each detector, it is likely that the addition of a muon veto system will significantly reduce the constant background rate in the new apparatus.

The new geometry of the cryostat is more conducive to placement of a veto system than the previous. With two vertical towers, the area directly above the experimental trapping region is open for placement of plastic scintillators. Two 100 cm square vetos

placed in an 'A-frame' type roof over this area will provide coverage from cosmic-rays passing directly through the cell. Two longer rectangles 146 cm by 32 cm of plastic scintillator will be placed beneath the apparatus to provide some coverage of the acrylic light collection system. This will be sufficient to veto a significant part of the predominantly vertical flux of cosmic radiation. Due to the background subtraction technique employed it won't be necessary to veto all of the background events as long as there is consistent background suppression from run to run.

## Chapter 4

# Systematic Studies

The experiment is expected to be statistics limited at the level of 2 – 3 s accuracy; systematic uncertainties must also be controlled below this level. The two largest systematic effects are expected to arise from neutron absorption by  $^3\text{He}$  and above threshold neutrons escaping from the trap. This chapter discusses in detail work performed in understanding and quantifying these two systematics along with a brief discussion of the gain stability of the photomultiplier tubes.

### 4.1 $^3\text{He}$ Contamination in the Isotopically Pure $^4\text{He}$

Though the neutron capture cross section on  $^4\text{He}$  is zero, the capture cross section for neutrons on  $^3\text{He}$  is large[82],  $\sigma_{th} = 5333(7)$  b. A sufficient isotopic impurity of  $^3\text{He}$  in the trapping region that is filled with  $^4\text{He}$  will provide a loss mechanism for neutrons and contribute to the systematic uncertainty.

The absorption rate for neutron capture on  $^3\text{He}$  is given by

$$\Gamma_{abs} = \int_v nR_{34}\sigma v\phi(v)dv. \quad (4.1)$$

The number density,  $n$ , of helium atoms is calculated using the density,  $\rho$ , of superfluid helium,  $n = \rho \times N_A/A = 2.17 \times 10^{22}$  cm $^{-3}$ . Since the absorption cross section is inversely proportional to the velocity of the neutron, one can express  $\sigma$  in terms of the thermal cross section and velocity,  $\sigma \equiv \sigma_{th}v_{th}/v$ , where the thermal velocity is  $v_{th} = 2224$  m/s. Eqn. (4.1) simplifies to

$$\Gamma_{abs} = nR_{34}\sigma_{th}v_{th} = 2.57 \times 10^7 R_{34} \text{ s}^{-1}, \quad (4.2)$$

independent of the velocity spectrum. Thus the uncertainty in the neutron lifetime is a function of the isotopic ratio,

$$\frac{\Delta\tau}{\tau_\beta} = \frac{\tau_\beta}{(\tau_\beta + \tau_{abs})} \sim \frac{\tau_\beta}{\tau_{abs}} = \frac{\Gamma_{abs}}{\Gamma_\beta} = 2.57 \times 10^7 R_{34} \tau_\beta. \quad (4.3)$$

For a lifetime measurement with a 0.1 % error, the isotopic purity must be less than  $R_{34} \leq 4.4 \times 10^{-14}$ .

The helium used in the experiment is purified using the heat flush technique developed by McClintock *et al.*[107] and was produced using his original apparatus. This isotopic purification method makes use of the fact that at low temperature helium has both a ‘normal’ and superfluid component. The superfluid component has zero entropy and the normal component has finite entropy. Since a change in entropy is thermodynamically required in a thermal transport process, this can be realized as a mass transfer of the normal fluid. For helium that is cooled below the  $\lambda$ -point but is still warmer than the  $^3\text{He}$  superfluid transition temperature,  $2.17 \text{ K} > T > 2.7 \text{ mK}$ , the superfluid component will be entirely  $^4\text{He}$ . When a thermal gradient is created across the helium, heat is transferred by a mass flow of the normal component. Since the  $^3\text{He}$  travels with the normal component, there will be an isotopic purity gradient created across this region of heat transfer. The  $^3\text{He}$  concentrate region can be discarded and the process may be repeated on the  $^3\text{He}$  dilute phase indefinitely until there is no  $^3\text{He}$  remaining.

The most precise direct mass spectroscopy measurements made on the isotopically pure helium produced by McClintock[107] set an upper limit of  $R_{34} < 2 \times 10^{-9}$ . The same measurement was performed on a sample that was purified a second time. In this second run, a sample was collected from the  $^3\text{He}$  concentrate end. The mass spectroscopy measurement on this sample set a similar upper limit of  $\lesssim 10^{-9}$ . Using this result, one can infer an indirect limit on the purity of the dilute phase of  $R_{34} < 2 \times 10^{-15}$ .

Mass spectroscopy measurements are made by ionizing the atoms and accelerating these ions through a magnetic field. A position sensitive detector is used to separate ions into groups according to their charge to momentum ratio ( $e/p$ ). Mass spectroscopy measurements of this type are limited by contamination of stable isobars. For example,  $\text{H}_3$  is a molecular isobar of  $^3\text{He}$  and not distinguishable in these measurements.

One way to remove this systematic is to use the technique of Accelerator Mass Spectroscopy (AMS). Here ions are first accelerated through an analyzer magnet selecting out a beam with a fixed  $e/p$ . This beam is further accelerated to energies on the order

of 1 MeV per nucleon. The beam then passes through a stripping foil to break molecular bonds and remove electrons from the nucleus. This technique separates groups of isobars. These particles are passed through a second analyzing magnet and into a position sensitive detector. The isotopic purity is determined from the measured rate of the particular isotope, a separately measured transmission through the accelerator, and the overall beam intensity prior to filtering.

A thorough discussion of the AMS measurements performed on an isotopically pure helium sample at the Argonne Tandem-Linac Accelerator System (ATLAS) facility can be found in Ref. [58]. From these measurements the  ${}^3\text{He}^{2+}$  ion was clearly separated from background ions, and a result of combining the data from multiple runs yields a value of  $R_{34} = (4.2 \pm 1.5) \times 10^{-12}$ . Since that work, one additional measurement was performed where notable discoveries were made. The isotopically pure helium was remeasured with  $R_{34} \approx \text{few} \times 10^{-12}$ , a value consistent with previous runs. However, a run with a sample of pure hydrogen gave results where both mass-4 isotopes and a clear  ${}^3\text{He}^{2+}$  ion peak were observed at a level of  $R_{34} \sim 10^{-8}$ . Since this ratio is consistent with the natural isotopic purity of helium, it is believed to be a background in the measurement. When this rate is scaled for the current of the helium beam used in the isotopically pure gas, the same backgrounds would produce a systemic effect at the level of  $R_{34} \sim 10^{-12}$ . Since the beam was originally tuned with a natural isotopic purity helium ion source in the volume surrounding the quartz cell used in these measurements, it is possible that some of this helium was diffusing through either the quartz or the rubber o-ring used to seal it.

A new source insert has been developed using “GE-180” alumina silicate glass, a material used in polarized helium cells because of its low diffusion rate for helium. This source insert is fused to the extractor electrodes using both intermediate glass and metal (kovar) sections. The source insert has been tested at the ATLAS facility. Beam time has been allocated to make a measurement of  $R_{34}$  with the new source configuration. A new manifold will be used to facilitate the clean changing of sample gasses by utilizing all metal seals.

From this upcoming run we hope to reduce the limits of the measurement another one to two orders of magnitude and ultimately make a measurement of the isotopic purity sufficient for the precision measurement of the neutron lifetime.

One can estimate the systematic uncertainty as a result of the measured limit of the isotopic purity using Eqn. (4.3). If  $R_{34} \leq 10^{-12}$ , this corresponds to a 9% systematic

uncertainty in the neutron lifetime measurement. The previous indirect measurement by McClintock, however, strongly suggests that this upper limit is due solely to background contaminants in the isotopic measurement. If one takes the value obtained by McClintock, the systematic shift is  $4.5 \times 10^{-3} \%$ , or 0.04 s. Almost two orders of magnitude lower than the anticipated statistical precision of the measurement.

In addition to the continuation of the direct measurements of the isotopic purity, there is the possibility for an *in-situ* heat flush in normal operation of the apparatus. Due to the heat load to the cell from blackbody radiation, primarily from the light collection side of the system, there will exist a thermal gradient between the light guide and mixing chamber of the dilution refrigerator of  $\Delta T \sim 10$  mK. Simulations of mass transfer in the geometry for the new apparatus imply that this is enough to reduce the  $^3\text{He}$  concentration in the cell by a factor of ten in steady state operation. By reducing the diameter of the fill line tubing one could get an additional factor of ten improvement with minimal effect on the experiment.

## 4.2 Above Threshold Neutrons

Simulations are also used to better understand the contribution to the systematic uncertainties from above threshold neutrons and the material bottling affects of these neutrons during the trap cleaning. By definition it is not possible to follow the individual trajectory of a particle through a series of interactions for which only stochastic properties are known[108]. It is however feasible to track the most likely properties of an ensemble of particles that obey the same stochastic interactions.

A Monte Carlo simulation has been created to estimate the fraction of marginally trapped neutrons that may escape the trap during the observation period[109]. The code uses a symplectic integration to track neutrons in the trap during the trap loading, the magnetic field ramp, and the observation period. When a neutron interacts with one of the cell wall surfaces, a probabilistic calculation is performed using the neutrons' energy and momentum to determine if the neutron is reflected or transmitted.

The physics that describes the neutrons' reflectivity, transmission and absorption in the material is modeled as a simple one-dimensional step potential. The actual surface deviates from the ideal scenario since it is composed of multiple layers of material with a surface roughness that modifies the neutron losses from this ideal case.

From this work we predict the difference in the trap lifetimes between runs with a magnetic field ramp procedure and those without.

#### 4.2.1 Simulations of Above Threshold Neutrons

The trap depth is defined as the minimum field at a surface where neutrons can interact with a material and be lost from the trap. Below this threshold, the trap lifetime is considerably longer than the neutron lifetime. Computer simulations are used to model the population of neutrons that have energies above the trap threshold and remain in the experimental cell during the observation period. This is accomplished using a Monte Carlo ray tracing code to track a population of individual particles through a realistic interpretation of the interactions they will experience.

A distribution of neutrons is generated with initial energies that fill the phase space available to UCN produced in the experimental cell. Each neutron is generated at a random position within the cell and assigned a kinetic energy  $T = p^2/2m$  using the density function  $f(T) \propto T^2$  in a low energy interval  $0 < T < T_{max} = 704$  neV. The total energy of the neutron is therefore  $E = T + V(\mathbf{x})$ , where  $V(\mathbf{x}) = \mu_n \cdot B(\mathbf{x})$  is the potential energy due to interaction with the magnetic field.

The magnetic field due to the current in the trap windings is calculated using the Radia[110] add-on package for Mathematica. The quadrupole is wound with a complex  $\cos 2\theta$  geometry, so each of the wires in this magnet are modeled independently, and the results combined. Figure 4.1 shows the cross section field maps taken along the center of the trap.

The field is calculated in three dimensions using a grid spacing of 5 mm along the axis and 1 mm in the plane normal to the axis. Given the neutron's position and velocity at time  $t$ , the field is approximated using a tensor spline method and used to determine a new position and momentum at time  $t + dt$  using a symplectic integration code [109]. If the radial distance of the neutron from the center,  $r$ , exceeds 5.6 cm, the neutron can interact with the wall of the experimental cell and either reflect back into the cell or become lost by transmission or absorption in the wall materials. When the  $z$ -coordinate along the axis of the trap exceeds 37.5 cm, the neutron can be either reflected from or absorbed by the acrylic light guide. Since there is no such constraint on the opposite side of the trap, a neutron is assumed to be lost once it has exceeded  $z = -42$  cm, as this is well beyond the

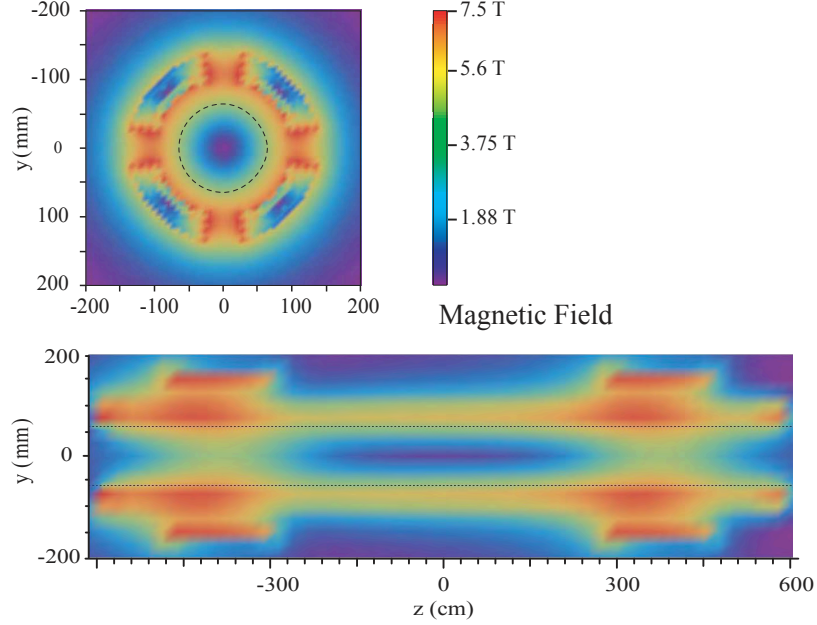


Figure 4.1: The two dimensional calculated field map for two cross sections of the trap, (a) a cross section through the plane normal to the trap axis and (b) the cross section of a vertical plane along the trap axis.

maximum potential of the upstream solenoid.

One can calculate the contamination fraction of above threshold neutrons,  $r_c$ , and the escape times to estimate the correction to the neutron lifetime that results from neutrons escaping the trap during the observation period. Additionally, by implementing ramping of the magnetic field from the quadrupole magnet, Figure 4.1c, one can optimize a ramping sequence to minimize  $r_c$ , and subsequent correction to the trap lifetime.

## Wall Interactions

As shown in Eqn. (2.1), when an ultracold neutron approaches a material surface, it interacts with that surface as a quantum mechanical one-dimensional step potential. Matching wavefunctions and their derivatives defines a solution that is smooth and continuous at the boundary,

$$\begin{aligned}
 A_{n-1}e^{i\mathbf{k}_{n-1}\cdot\mathbf{x}_n} + B_{n-1}e^{-i\mathbf{k}_{n-1}\cdot\mathbf{x}_n} &= A_n e^{i\mathbf{k}_n\cdot\mathbf{x}_n} + B_n e^{-i\mathbf{k}_n\cdot\mathbf{x}_n} \\
 k_{n-1}(A_{n-1}e^{i\mathbf{k}_{n-1}\cdot\mathbf{x}_n} - B_{n-1}e^{-i\mathbf{k}_{n-1}\cdot\mathbf{x}_n}) &= k_n(A_n e^{i\mathbf{k}_n\cdot\mathbf{x}_n} - B_n e^{-i\mathbf{k}_n\cdot\mathbf{x}_n}).
 \end{aligned} \tag{4.4}$$

Here, the neutron is incident from within a material,  $n - 1$ , with wavevector,  $k_{n-1} = \sqrt{2m(E_{\perp} - V_{n-1})/\hbar^2}$ , as defined by the component of the neutron's energy that is normal to the surface,  $E_{\perp}$ , and material's Fermi potential,  $V_{n-1}$ . When it meets another material  $n$  at a boundary  $x_n = 0$  the neutron's wavevector consequently becomes  $k_n = \sqrt{2m(E_{\perp} - V_n)/\hbar^2}$ . The matching of boundary conditions requires that the incident amplitude  $A_{n-1} \equiv 1$  is equivalent to the sum of the reflected and transmitted amplitudes,  $R = B_{n-1}$  and  $T = A_n$  respectively. There is no component of the wavefunction in the second material that is returning to the first, therefore the amplitude  $B_n = 0$  within the second medium. The second boundary condition allows the solution of

$$R = \frac{k_{n-1} - k_n}{k_{n-1} + k_n} = \frac{(E_{\perp} - V_{n-1})^{1/2} - (E_{\perp} - V_n)^{1/2}}{(E_{\perp} - V_{n-1})^{1/2} + (E_{\perp} - V_n)^{1/2}}, \quad (4.5)$$

and

$$T = \frac{k_{n-1}}{k_{n-1} + k_n} = \frac{(E_{\perp} - V_{n-1})^{1/2}}{(E_{\perp} - V_{n-1})^{1/2} + (E_{\perp} - V_n)^{1/2}}. \quad (4.6)$$

For the case where  $E_{\perp} > V_n$ , the corresponding  $k$ 's are real and the reflection probability  $|R|^2 < 1$ . When  $E_{\perp} < k_n$ , the wavevector becomes imaginary,

$$k_n = i\kappa_n = i\sqrt{\frac{2m}{\hbar^2}(V_n - E_{\perp})}, \quad (4.7)$$

for real  $V_n$ . A convenient way to parameterize neutron losses is to define a complex material potential,  $U = V - iW = 2\pi\hbar^2Na(1 - i\eta)/m$ . In such a case, the transmitted wave has the form,

$$Te^{ik_nx} = Te^{-\kappa_nx}, \quad (4.8)$$

where the wavefunction penetrates the medium with a characteristic length of  $1/\kappa$ . In the case where  $E_{\perp} < Re[V_n]$  the reflection probability is still  $|R|^2 = 1$  however the neutron then spends time within the medium  $n$ . If this medium has a complex material potential, where

$$W = \frac{\hbar}{2} \sum_i N_i \sigma_l^{(i)} v, \quad (4.9)$$

the neutron has a finite probability for being lost, either absorbed or up-scattered. The total loss cross section,  $\sigma_l$ , can be from absorption in the material, or from inelastic scattering.

The reflection coefficient can be calculated for a neutron in vacuum incident on an interface with a semi-infinite plane of complex material potential. One can replace  $V_n$

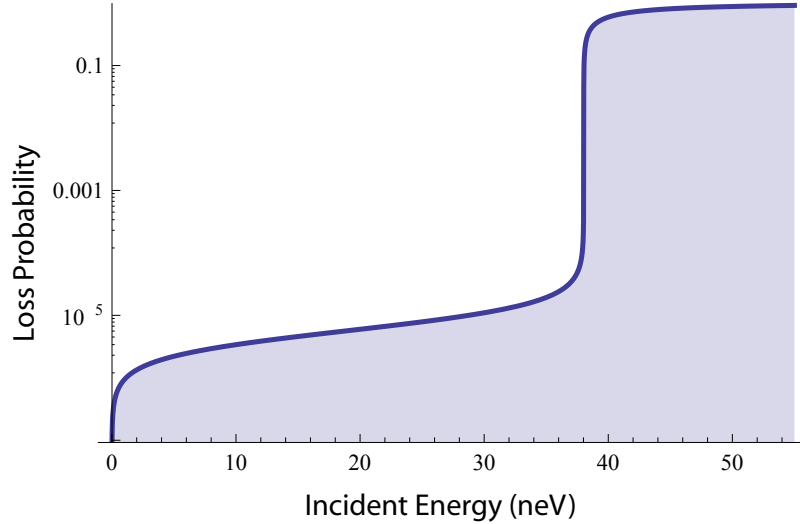


Figure 4.2: Loss probability for a neutron incident on a semi-infinite plane of Tetraphenyl Butadiene.

with the complex potential  $U$  and Taylor expand the square root terms of Eqn. (4.5). If  $W \ll V$  as is typically the case, keeping only first-order terms in  $W$  will result in,

$$|R|^2 = 1 - 2\frac{W}{V} \left( \frac{E_{\perp}}{V - E_{\perp}} \right)^{1/2} \equiv 1 - \mu(E, \theta) \quad (4.10)$$

where  $\mu(E, \theta)$  is defined as the loss probability per bounce. This has also been calculated in general for all  $W$ [111],

$$|R|^2 = \frac{E_{\perp} - \sqrt{E_{\perp}(2\alpha - 2(V - E_{\perp}))} + \alpha}{E_{\perp} + \sqrt{E_{\perp}(2\alpha - 2(V - E_{\perp}))} + \alpha}, \quad (4.11)$$

with,

$$\alpha = \sqrt{(V - E_{\perp})^2 + W^2}. \quad (4.12)$$

Figure 4.2 shows the loss probability for a neutron at normal incidence on an infinite boundary of TPB, whose properties are given in Table 4.1.

The assumption that the material is of infinite extent is not a valid approximation for materials with macroscopic thicknesses, even at the level of millimeters, since the UCN wavelengths can be quite long. From Eqn. (4.5) it is straightforward to create a matrix representation of the boundary conditions. Such a formulation provides a convenient method for dealing with a complex interface of multiple layers as if it were a single interface. An

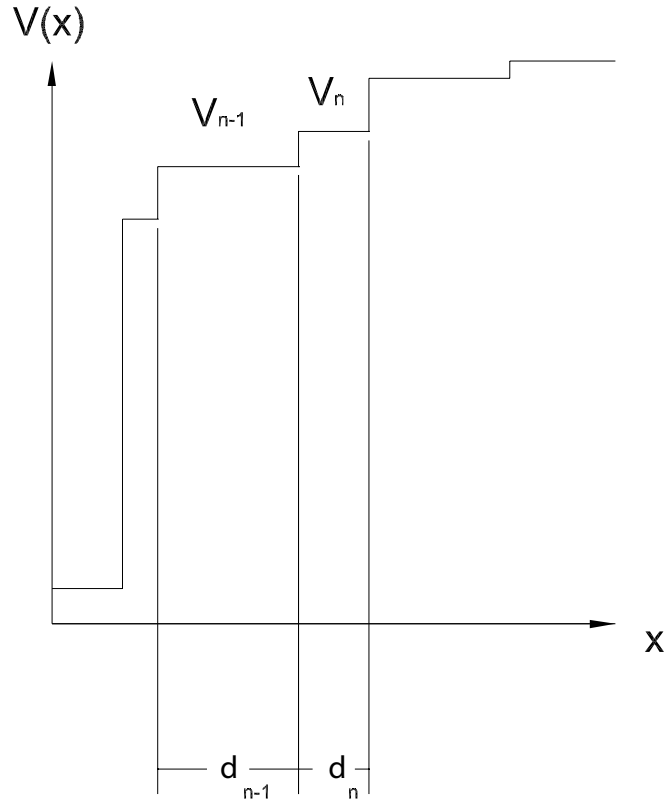


Figure 4.3: The transfer matrix provides a simple way of calculating reflection and transmission probabilities from a complex surface that may be represented as a series of step potentials,  $V_n$ , with thicknesses  $d_n$ . The details of the boundary conditions are contained in this matrix operator.

example of this shown in Figure 4.3. At the interface between two different materials, the boundary conditions can be represented as,

$$\begin{bmatrix} 1 & 1 \\ k_n & -k_n \end{bmatrix} \begin{pmatrix} A_n \\ B_n \end{pmatrix} = \begin{bmatrix} 1 & 1 \\ k_{n-1} & -k_{n-1} \end{bmatrix} \begin{pmatrix} A_{n-1} \\ B_{n-1} \end{pmatrix}. \quad (4.13)$$

The following result is obtained by applying the inverse of the first matrix to both sides,

$$\begin{pmatrix} A_n \\ B_n \end{pmatrix} = \frac{1}{2} \begin{bmatrix} 1 + k_{n-1}/k_n & 1 - k_{n-1}/k_n \\ 1 - k_{n-1}/k_n & 1 + k_{n-1}/k_n \end{bmatrix} \begin{pmatrix} A_{n-1} \\ B_{n-1} \end{pmatrix} \quad (4.14)$$

$$= [D]_{(n-1,n)} \begin{pmatrix} A_{n-1} \\ B_{n-1} \end{pmatrix}. \quad (4.15)$$

Relating the amplitudes by matching boundary conditions across a one-dimensional discontinuity, the expression can now be expressed as a single matrix operator,  $[D]_{(n-1,n)}$ . Considering a material that is layered, it is possible to account for multiple boundaries by applying this operation multiple times. However, it must be taken into consideration that the wavefunction, a function of position, will vary as one considers boundaries at different depths in a material,

$$\psi(x') = \psi(x + L) = A_n e^{ik_n(x+L)} + B_n e^{-ik_n(x+L)}. \quad (4.16)$$

In the matrix formulation however, it requires only the application of the propagating operator to relate the wavefunction at a position  $x' = x + L$  to that at position  $x$

$$\begin{pmatrix} A_n e^{ik_n x'} \\ B_n e^{-ik_n x'} \end{pmatrix} = \begin{bmatrix} e^{ik_n L} & 0 \\ 0 & e^{-ik_n L} \end{bmatrix} \begin{pmatrix} A_n e^{ik_n x} \\ B_n e^{-ik_n x} \end{pmatrix} \quad (4.17)$$

$$= [P]_n \begin{pmatrix} A_n e^{ik_n x} \\ B_n e^{-ik_n x} \end{pmatrix}. \quad (4.18)$$

Using the two matrix operators  $[D]_{(n-1,n)}$  and  $[P]_n$ , one can match the boundary conditions for a complex material of many layers using a single matrix element.

$$\begin{pmatrix} T \\ 0 \end{pmatrix} = [D]_{(n-1,n)} \cdot [P]_{(n-1)} \cdots [D]_{(2,3)} \cdot [P]_2 \cdot [D]_{(1,2)} \begin{pmatrix} 1 \\ R \end{pmatrix} = \begin{bmatrix} t_{11} & t_{12} \\ t_{21} & t_{22} \end{bmatrix} \begin{pmatrix} 1 \\ R \end{pmatrix} \quad (4.19)$$

This is known as the transfer matrix[112] and is a common method for applying the Fresnel equations to obtain transmission and reflection amplitudes through thin multi-layered materials in optics. Upon inversion of the transfer matrix, the reflection amplitude is

$$R = \frac{-t_{21}}{t_{22}}, \quad (4.20)$$

and the transmission amplitude is

$$T = \frac{k_{init}/k_{final}}{t_{22}}. \quad (4.21)$$

A simple verification of  $[D]_{(n-1,n)}$ , the discontinuity operation from Eqn. (4.15), can be immediately realized by applying Eqn. (4.20) and (4.21). The results are the expected amplitudes of Eqn. (4.5) and (4.6).

Applying this technique to the geometries and materials of the cell linings, one arrives at the calculation of loss probability for normally incident neutrons. The results

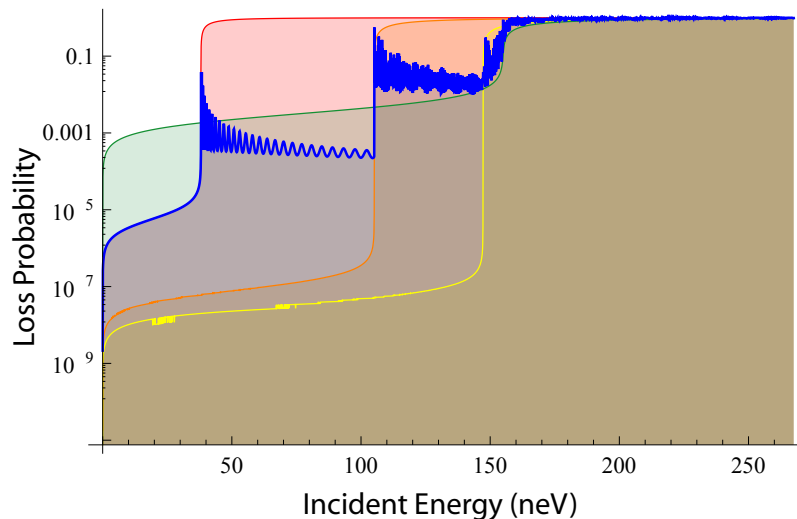


Figure 4.4: Loss probability for a neutron with normal incidence on the cell wall as calculated with the transfer matrix (blue), overlaid are losses for neutrons incident on an infinite thickness of each of the cell materials. The critical energy for each of the materials is greater than the last: TPB - red, Goretex - Orange, Graphite - Yellow, Boron Nitride - Green.

of this calculation are shown in Figure 4.4. The analytic solution for the loss probability contains the magnitude square of a matrix element, a calculation that results in a large number of matrix multiplications that are performed numerically. The materials and geometries for this calculation are given in Section 4.2.1 and the calculations for the single infinite interface from Eqn. (4.11) for each of the materials are overlaid to highlight how this geometry modifies the loss. Further verification is reached by varying the thicknesses of the materials. As one layer becomes thin, the loss probabilities approach the single interface result for the next layer in the stack.

### Diffuse Reflections

The probability of reflection, transmission, and absorption at an interface with different material potentials is only one component of an approximation to the full stochastic processes that must be taken into account in a simulation of the interactions a neutron can have with a material wall. It is also necessary to consider the surface roughness of the interface that provides for the possibility of diffuse scattering as described in the framework of optics in Section 3.3.3. In a Monte Carlo simulation of neutron-wall interactions, the

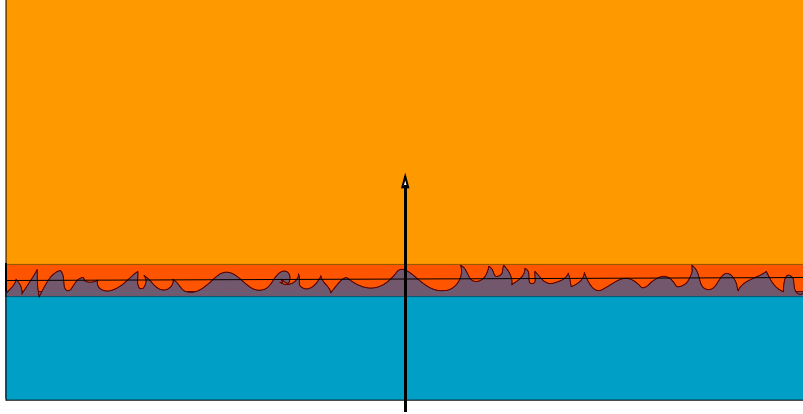


Figure 4.5: The boundary of a rough surface may be treated as a perturbation to the flat plane

surface roughness of the wall can be modeled as a probability for diffuse reflections. As was seen in the case of photon ray tracing, a diffusely reflecting surface has two implications for the model. First, the angular distribution of the reflected neutron no longer depends on the incident angle, rather it has a  $\cos \theta$  dependence with the normal to the surface. Second, surface roughness adds potential modes of neutron losses. The surface roughness increases the surface area for the neutron to interact with, while an increased angular distribution may also increase the wall interaction rate. Depending on the length scale of the roughness, there could be interference effects that generate an increase in the loss probability. The surface roughness can be modeled as a perturbation to the perfect plane. The deviation from a plane, as pictorially represented in Figure 4.5, can be represented as a height-height correlation function,

$$f(\delta) = \lim_{A \rightarrow \infty} \frac{1}{A} \int_A \xi(\rho) \xi(\rho + \delta) d\rho,$$

between the elevation  $\xi(\rho)$  at a point on the planar surface  $\rho(x, y)$  and at  $\rho(x + \Delta x, y + \Delta y)$ . This can be modeled with a Gaussian distribution as:

$$f_G(\delta) = b^2 \exp[-\delta^2/(2w^2)],$$

where  $b$  is the RMS elevation and  $w$  is the correlation length. Using Green's functions to calculate the perturbation, Steyerl *et al.*[113] have calculated the probability for diffuse reflections from rough surfaces,

$$p_D = p_{D0} - 2k^4 \cos \theta_i \int_{2\pi} d\Omega \cos^2 \theta [\mu_0(\theta_i) + \mu_0(\theta)] F(q), \quad (4.22)$$

up to order  $b^2$  and  $\eta$ , where  $p_{D0}$  is the diffusely scattered intensity for  $\eta = 0$ , and  $\mu_0$  is the unperturbed loss probability from Eqn. (4.10). Also calculated is the loss probability from rough surfaces,

$$\begin{aligned} \mu(\theta_i) &= \mu_0(\theta_i)(1 + k_{c0}^2 b^2) \\ &\quad - 2k^4 \cos \theta_i \int_{2\pi} d\Omega \cos^2 \theta [\mu_0(\theta_i) - \mu_0(\theta)F(q) - k^2 k_{c0}^2 \cos \theta_i \int_{2\pi} d\Omega \mu_0(\theta)F(q), \end{aligned} \quad (4.23)$$

where the critical wavevector for the material is  $k_{c0} = \sqrt{2mV/\hbar^2}$ . In both of these calculations, the Fourier transform of the height-height correlation function, Eqn. (4.22), is either

$$F(\mathbf{q}) = \frac{1}{(2\pi)^2} \int_A f(\delta) e^{-i\mathbf{q}\cdot\delta} d^2\delta, \quad (4.24)$$

or for the Gaussian model,

$$F(q) = \frac{b^2 w^2}{(2\pi)} e^{-q^2 w^2/2}. \quad (4.25)$$

Here  $\mathbf{q}$  is the momentum transfer parallel to the plane of the wall such that  $k^2 d\Omega \cos \theta = d^2\mathbf{q}$ .

In order to solve the indefinite integrals of Eqn. (4.22) and (4.24), the authors make a variable substitution that enables them to make the approximation that  $F(q) \ll 1$ , valid for  $kw \gg 1$ . They then expand the solution in a series of definite integrals of order  $q^0$ ,  $q^2$ , and  $q^4$  where they solve for  $p_{D0}$ , and  $\Delta\mu/\mu_0$ . Results were derived for smooth surfaces such as liquids or glasses that have small RMS slopes,  $\alpha \ll 1$ , and therefore are only valid in the regime where  $p_{D0} \ll 1$ , the highly specular case.

Another model, the so-called ‘‘dense-roughness’’ model[114], approximates the other extreme, diffuse scattering from a surface where  $w \rightarrow 0$ . While  $b$  remains large, this represents a surface with tall and narrow ‘furry’ surface features. The  $\Delta\mu/\mu_0$  for this model represents losses due to a smearing of the material potential

$$V(z) = \frac{V_0}{1 + e^{-z/h}}, \quad (4.26)$$

where  $h$  is the smearing parameter. Averaged over angles of incidence

$$\mu = \mu_0 [1 + f(h)\sqrt{V_0}], \quad f(x) = \begin{cases} \pi^2 x^2/3, & x \rightarrow 0, \\ 2x, & x \rightarrow \infty. \end{cases} \quad (4.27)$$

The cell materials for the neutron lifetime experiment, TPB powder evaporated onto a porous Gore-Tex substrate, were designed for highly diffuse optical reflections. They are thus not likely to meet the criteria of the first model. Additionally, the width of

the correlations is not significantly smaller than the height, so neither of these models is particularly appropriate for the materials of interest in the neutron lifetime experiment. In order to properly characterize roughness at the surface of the material used, one first must understand the roughness of the substrate, as this will be convolved with the surface of the TPB to give the overall roughness of the system.

Gore-Tex is a PTFE Teflon material that has been stretched and expanded to create a porous structure. The pores are micron sized and the material is hydrophobic, thus the common waterproof applications of the material. Since the coating of TPB is also micron sized, one must examine this porous nature of the material.

The pores allow a possibility of bound state resonance capture of the neutrons[114]. The resonance states have a finite width,  $\Gamma$ , a sum of the width due to the pore wall losses from UCN storage within the pores,  $\Gamma_1$ , and the width,  $\Gamma_t$ , that describes the probability of tunneling out of the pore. The width,  $\Gamma_1 = h/\tau_1$ , where  $\tau_1 = r/v\mu$  the storage time within the pore, is proportional to the rate of pore wall interactions  $v/r \sim(\text{MHz})$  and the loss probability per interaction  $\mu$ . When the incident energy of the neutron penetrating the pore wall is less than the material potential, there will be a non-zero tunneling probability amplitude as was seen in Eqn. (4.8). The tunneling width  $\Gamma_t = 1/\tau_t$  is described by the dwell time spent in the material,  $\tau_t = \int_{\Omega} |\psi(x)|^2 dx/v = |T|^2 \int_{\Omega} e^{-\kappa x} dx/v$ . The additional wall loss from the resonance states can be represented by the Breit-Wigner formula,

$$\Delta\mu = \frac{\Gamma_1\Gamma_t}{(E - E_r)^2 + (\Gamma_1 + \Gamma_t)^2}, \quad (4.28)$$

where  $E_r$  is the resonance energy for a given pore size  $r$  and depth  $x$  within the material. When the time spent in the pore is much longer then the dwell time spent between the material surface and the pore,  $\Gamma_t \gg \Gamma_1$ , then at the resonance,  $\Delta\mu = \Gamma_1/\Gamma_t$ . When Eqn. (4.28) is averaged over incidence angle and dimensions and distributions of pores, the result can be modeled simply using the volume fraction of the pores,  $V_p$ ,

$$\Delta\mu = -12V_p\mu_0 \ln \mu_0. \quad (4.29)$$

Taking the ratio of the densities of Gore-Tex and PTFE given in Table 4.1, one can determine the volume fraction that the pores occupy is 0.58. This modifies the loss probability as shown in Figure 4.6. In this figure, one can see that the modification to the behavior below  $\sim 100$  neV can be approximated by increasing the  $W$  by a scale factor of about 150. Just above  $\sim 100$  neV the behavior of the resonance is unphysical as it

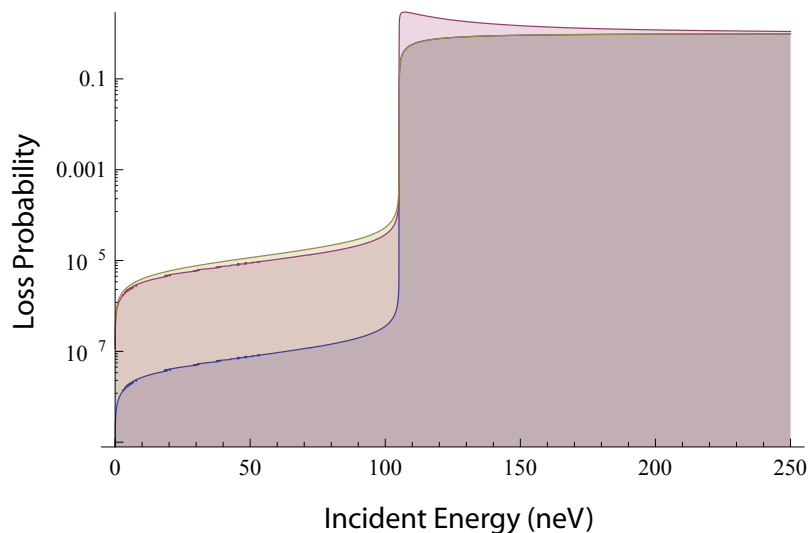


Figure 4.6: The loss probability for a neutron of normal incidence on an infinite thickness of PTFE (blue), the modifications for a porous Gore-Tex material (red) and PTFE with  $W$  increased by a factor of 150 (yellow).

approaches a factor of roughly 2. This might suggest that an inappropriate assumption has been made in the averaging when dealing with a surface with a large volume fraction of pores.

Even in the case of the dense-roughness model where the potential is smoothed by some factor, one characteristic expressed for all diffuse scattering models is that the loss probability has a transition from low to high and approaching one with a mean incident neutron energy that corresponds to the real part of the potential. The only model with an affect on the real part of the potential is the dense-roughness model. This model reduces the material density in the case were the correlation length for the roughness is shorter than the neutrons de Broglie wavelength. In all other cases the only parameter that is modified by the surface roughness model is the imaginary part of the potential.

### Cell Materials

The experimental cell is a 316L stainless steel tube that was designed to suspend the 9 L volume of isotopically pure superfluid  $^4\text{He}$  within the trapping region of the magnet. Because this is a metallic component, it will activate when exposed to the neutron beam. To capture both the beam of cold neutrons as they scatter into the cell wall and the UCN that

Table 4.1: At the cylindrical walls the neutron interacts with the series of layers from helium to boron nitride in the order shown. The bulk properties of Gore-Tex are shown, though on the length scales of the neutrons wavelength the material is the same as PTFE. On one end of the cell a neutron will see a boundary between the helium and acrylic.

Material	Stoichiometry	density (g/cc)	V (neV)	W (neV)	Thickness
Helium	${}^4\text{He}$	0.125	15.98	0	$\infty$
TPB	$\text{C}_{28}\text{H}_{22}$	1.2	54.5	$1.08 \times 10^{-3}$	$1.5 \mu\text{m}$
(PTFE)	$(\text{CF}_2)_n$	2.15	121.1	$4.26 \times 10^{-5}$	2 mm
Gore-Tex	$(\text{CF}_2)_n$	0.7	39.4	$1.39 \times 10^{-5}$	
Graphite	C	1.88	163.2	$2.39 \times 10^{-5}$	1 mm
Boron Nitride	BN	1.85	171.4	2.5	3 mm
Acrylic (PMMA)	$\text{C}_5\text{O}_2\text{H}_8$	1.19	27.8	$1.39 \times 10^{-3}$	$\infty$
Boron Oxide	$\text{B}_2\text{O}_3$	2.46	155.3	2.36	$\infty$

are produced above the trapping potential, a 3 mm thick layer of Boron Nitride (BN) lines the cell in the neutron trapping region. In order to block luminescence light, a 1 mm thick tube of graphite lines the inside of the BN. The detector insert is the innermost lining of the cell and consists of a 2 mm thick Gore-Tex gasket material coated with approximately  $1.5 \mu\text{m}$  of evaporated Tetraphenyl Butadiene (TPB).

The surface roughness of the TPB evaporation on Gore-Tex was characterized using contact profilometry<sup>1</sup>. The measurements were performed using a stylus with a  $12.5 \mu\text{m}$

<sup>1</sup>Using a Veeco Dektak6 Profilometer

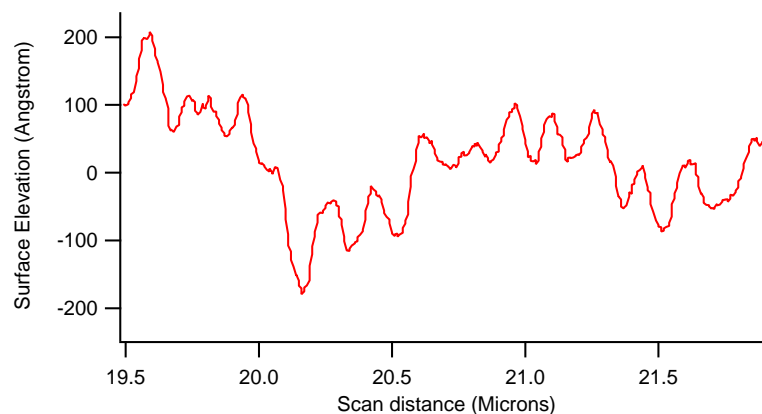


Figure 4.7: The surface roughness of TPB evaporated on a Gor-Tex substrate.

Table 4.2: Surface character of the detector insert materials.

Surface	Length Scale ( $\mu\text{m}$ )	RMS Elevation ( $\text{\AA}$ )
TPB Evap.	500	8000
	350	4300
	40	950
	35	350
	2	50
Bare Gore-Tex	500	6000
	350	5300
	40	6300
	35	360
	2	7

radius tip and 3 mg force. No surface deformations were observed during the measurements. To characterize different length scales while maximizing the spacial resolution, several scans of varied lengths and locations were performed. While the RMS elevations over longer length scales characterizes a waviness to the material, it is likely that the important length scales are those similar to the De Broglie wavelength of the neutrons, 55-173 nm. As shown in Figure 4.7, an almost periodic RMS roughness of 50  $\text{\AA}$  with an average length of 170 nm appears in the scans. As this behavior appears in samples taken with and without the TPB evaporation, this is most likely the pore size of the Gore-Tex substrate. This is consistent with the geometry of the measurement. The largest resolvable elevation change for a stylus with a radius of 12.5  $\mu\text{m}$  for a feature with a width of 2  $\mu\text{m}$  is 80 nm. The scan of the TPB evaporation on the substrate on these length scales was taken at a slower rate than the scan of bare goretex. If the regular feature seen on the 2  $\mu\text{m}$  length scales is indeed a pore structure of the material, it is likely that the RMS elevation is much greater than measured.

As was seen in the photon ray tracing code with the aid of experimental data in a well understood geometry, one can produce an effective model by adjusting a small number of parameters until the model agrees with the data. In this case, one has data from the previous apparatus, a magnetic trap having a very similar detector geometry; the primary differences are a larger volume, and a deeper trap in the new apparatus. By modeling the number of above threshold neutrons for runs where the magnetic field was both ramped and not ramped, the shift in the lifetimes from the escape of marginally trapped neutrons

can be extracted. In this way, one can predict the shift in the trap lifetimes between the different configurations. If the model is effective, the predicted shift in lifetimes will reproduce the measured ones, even if a population of above threshold neutrons remain in the trap after the ramping procedure. With only one measured parameter, the shift in lifetime with and without field ramping, one can fit only one varied parameter. In the future, one could consider varying additional operational parameters to increase the number of fit parameters. For now, only the imaginary parts of the Gore-Tex and TPB potentials will be varied together as these will have the largest affect on the loss probability. The probability of diffuse scattering is assumed to be similar to the photon simulations,  $\sim 0.93$ , as their characteristic wavelength is similar. From this model we then plan to generate a prediction of the shift in the trap lifetime due to ramping of the fields in the new KEK trap geometry.

Some UCN produced in the experimental cell may be marginally trapped by the trapping field. If their energies are just moderately higher than the trap threshold, they may stay on stationary trajectories for extended periods of time and escape the trapping region before they decay. This introduces a shift in the trap lifetime such that it is shorter than the neutron lifetime. It has been shown in Ref. [58] that these above threshold neutrons may be cleaned from the spectrum of UCN in our trap using a magnet ramping scheme (see Figure 2.7). When the field is ramped down there is an adiabatic expansion of the orbits of the neutron trajectories. If the field is ramped low enough, the probability of ejecting all above threshold neutrons becomes quite high. The probability of ejecting below threshold neutrons will increase as well. To fully understand this procedure, it is important to study the systematic shift in the trap lifetime as a function of the minimum field reached during the ramp procedure.

The study is performed using the ray tracing model described in Section 3.3.3. Since the solenoids have a high impedance, only the quadrupole magnet will be ramped in the experiment. The potential traversed by the neutron is modeled as

$$V(t) = -\mu_n(B_s + (1 - \beta(t))B_q), \quad (4.30)$$

where a ramp factor,  $(1 - \beta(t))$ , is introduced to reproduce the appropriate time dependence of the field. The ramping rate is varied such that the quadrupole field reaches different minimum values, as shown in Figure 4.8.

Tracked neutrons are also allowed to interact with the material walls of the experimental cell as discussed in Section 4.2.1. From the simulation, Monte Carlo estimates

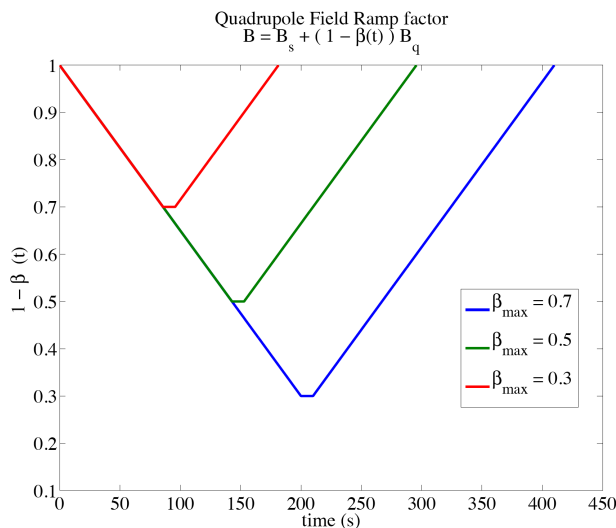


Figure 4.8: Ramping schedules used in studies of above threshold neutrons.

are made of the escape time distributions and the contamination ratio of above threshold neutrons[115]. The threshold is defined as the minimum field on the trap boundary,  $V_{thresh} = 0.67V_{max}$ , as can be see in Figure 4.9.

Like the experiment, the simulation is performed in two stages, a trap loading phase and an observational phase. Trap loading occurs between times  $t_0$  and  $t_L$ , during which a population of both above threshold and below threshold neutrons is produced, with production rates  $R_+$  and  $R_-$  respectively. The expectation values of the number of above

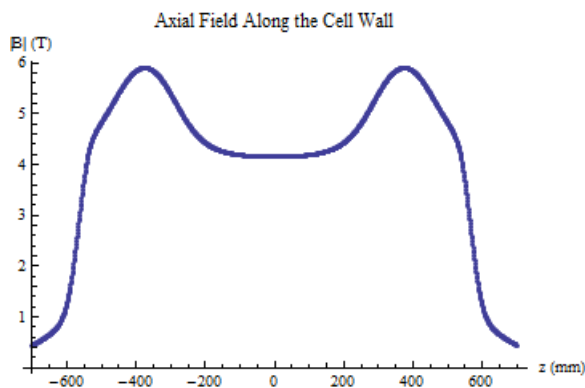


Figure 4.9: Magnetic field along the surface of the cylindrical cell wall

and below threshold neutrons produced are:

$$\langle N_+(t_L) \rangle = R_+ \int_x \int_p \int_{t_0}^{t_L} F(t - t_L, x, p) \exp\left(\frac{t - t_L}{\tau_n}\right) g(x, p) dx dp dt \quad (4.31)$$

and

$$\langle N_-(t_L) \rangle = R_- \tau_n \left(1 - \exp\left(\frac{t - t_L}{\tau_n}\right)\right). \quad (4.32)$$

The probability that a neutron produced at a position  $x$ , with momentum  $p$ , and escapes the trap at time  $t = t'$  is  $F(t - t_L, x, p)$ . Thus the cumulative probability density functional for the escape time distribution of above threshold neutrons is defined as,  $P_e = F_{esc}(t_{obs} - t_L)$ . From this, the contamination ratio is defined

$$r_c = \frac{\langle N_+(t_L) \rangle P_e}{\langle N_-(t_L) \rangle + \langle N_+(t_L) \rangle (1 - P_e)} \quad (4.33)$$

and an escape rate of non-decayed UCN can be calculated for the duration of the observation period,  $t_{obs} - t_L$ . The utility of this is twofold. First the geometry and fields of the Mark II trap is modeled for a static field,  $\beta_{max} = 0$ , and a ramped field,  $\beta_{max} = 0.7$ . The difference in cumulative escape rates for these simulations gives a calculation for the expected shift in the trap lifetimes. This provides a benchmark for the modeling of wall interactions. We may then use the same function to predict the shift of trap lifetime in the case of static fields due to above threshold neutrons. Optimization of the field ramp parameter,  $\beta_{max}$ , allows us to minimize the contamination ratio below the planned level of precision,  $< 0.1$  s.

### 4.3 Gain Stability of the Detectors

It was understood in the previous apparatus that detector gain drifts, one of the largest contributions to the uncertainty budget, was a solvable problem. Exposure to intense light can result in saturation of the PMTs that can lower their gain. To avoid damaging the detectors, the high voltage bias is turned off during the time the neutron beam is on as significantly larger amounts of light are produced in neutron capture reactions. The gain can also shift during the warm-up period after the PMT bias is turned back on.

Gain shifts as large as 2% were observed in the previous apparatus. An LED was used to send quantified pulses of light into each photomultiplier tube in order to monitor the gain shift so that the data could be properly corrected. Although the components were chosen for stability, the possibility exists that the LED pulse could drift in amplitude as a

result of temperature changes. The facility where the experiment resides is not temperature stabilized and experiences temperature drifts of 1 – 2%. Our group has designed and are in the process of implementing a system to monitor the gain shifts more precisely by observing the LED pulser spectra in a separate isolated system operating in coincidence with a radioactive calibration source. Light from the LED is divided into multiple optical fibers, each going to a separate PMT. The calibration source provides a reference for the LED pulser peak that can be used to normalize the intensity of the LED pulses. One can thus determine the absolute scale for the shifts in gain.

The pulser events into the primary PMTs can be removed from the data in post processing using either the event time stamp and possibly pulse shape analysis. With this absolute reference, the uncertainty in the neutron lifetime from PMT gain drifts can be reduced to  $< 0.01$  s.

## Chapter 5

# Conclusions

This thesis presents work toward a precision measurement of the neutron lifetime using magnetically trapped ultracold neutrons. Using the knowledge gained from two preceding experiments, the resulting apparatus described here has been constructed, tested, and is poised to take initial neutron trapping data. Significant improvements in the accuracy of the neutron lifetime should be realized since the new apparatus has a significantly larger and deeper magnetic trap. Furthermore, the optimization of the light collection system, based on calibration data taken with the previous apparatus, will enhance the improvements in statistical accuracy. The design of more robust shielding both within and external to the apparatus additionally improves the statistical figure of merit,  $signal^2/background$ . Work to improve the systematic effects in the measurement has been twofold. First, improvements were made in the AMS technique for measuring the isotopic purity of the helium. Secondly, the physical model for wall interactions has been much improved in the simulation of above threshold neutrons. By properly accounting for the wall interactions, a simulation of the previous apparatus will provide a calculation for the shift in neutron lifetime expected in that apparatus. This will enable one to both directly calculate the expected shift in the neutron lifetime due to above threshold neutrons in the new apparatus, as well as to optimize the field ramping procedure to minimize this shift.

The measurement of the neutron lifetime using the new apparatus is expected to ultimately achieve a precision of 0.2-0.3% at its present location and could reach the 0.1% level or lower with upgrades to the NCNR facility. These estimates are based on the performance of the previous apparatus and a careful scaling of the signal and of the backgrounds for the new trap geometry.

Table 5.1: Parameters of the former and current traps used for scaling the signal and background.

	Trap Volume (L)	Trap Depth (T)	Helium Volume (L)	Acrylic Volume (L)
Mark II Trap	2.5	1.1	7	7.8
KEK Trap	8.5	3.1	15	14

In the former work, a short trap lifetime of  $621 \pm 18$  s was observed with static fields. While using the magnet ramping technique for ejecting above threshold neutrons the trap lifetime was modified to  $831 \pm 58_{stat} \pm 88_{syst}$  s. The significant parameters for the performance of both the Mark II trap and the new trap are highlighted in Table 5.1. Where the number of trapped neutrons, and thus the signal, scales as  $N \propto B^{3/2}V$ . From the integrated decay rate it is known that there are initially about 1650 trapped neutrons in the Mark II apparatus. One can therefore expect to trap on the order of 40,000 neutrons for each run in the new apparatus. Additionally, due to the improvements in the light collection system an average factor of 1.64 increase in mean peak height over the entire experimental cell region was demonstrated through Monte Carlo simulation. The constant backgrounds are from the flux of external radiations depositing energy in the cell, or in the acrylic. This component of backgrounds will therefore scale with the volume of the helium and acrylic. However, preliminary background measurements suggest an improvement over the constant background rate of the previous apparatus. This is most likely due to improved shielding of the apparatus. The time dependent background is more difficult to estimate because the source is harder to identify. It likely arises from activation of impurity materials that interact with the 0.89 nm neutron beam. To this date neutrons still have not been allowed into the apparatus. This is because it will be desirable to take background measurements with a pristine cell that has been filled with helium. Since the cell has not been filled in its final configuration, this data has not yet been taken. Introducing neutrons to the cell before this measurement could change the results due to secondary activation.

A calculation of the statistical uncertainties and the projected run times required follows from a Monte Carlo calculation using these signal and background factors, shown in Table 5.2 assuming a central value of the world average for neutron beta decay. If the statistics and backgrounds do scale as expected, it is reasonable to believe a measurement with a statistical uncertainty of 2 s is achievable with the apparatus in its current configu-

Table 5.2: Scaling of signals and backgrounds for statistical uncertainty estimates.

Setup	Number Trapped	Detection Efficiency (%)	Constant Background ( $s^{-1}$ )	Time Varying Background ( $s^{-1}$ )	40 Day Cycle $\sigma$ (s)
Mark II	1650	48	11	2.9	36
KEK Trap	40,000	54	22	2.9	2.0

ration. As was seen in Chapter 4, it will be possible to demonstrate that the systematics can easily be controlled on the level of  $< 1$  s. Therefore as it stands, the apparatus is poised to make a measurement with a total uncertainty of  $< 3$  s. Although the world average value is  $885.7 \pm 0.8$  s, the measurements are of two types only and in light of the recent measurements that are highly discrepant from this value, it is conceivable that there exist blinded systematics that plague these measurements. For this reason this measurement is a critical measurement to be made with its proposed precision as the potential systematics are of an entirely different nature than in previous measurements.

# Bibliography

- [1] A. H. Bequerel. On the rays emitted by phosphorescence. *Comptes Rendus*, 122:420, 1896.
- [2] R. Reid. *Marie Curie*. Signet, 1978.
- [3] J. J. Thomson. XL. Cathode Rays. *Philos. Mag. Ser. 5*, 44(269):293–316, 1897.
- [4] E. Rutherford. VIII. Uranium radiation and the electrical conduction produced by it. *Philos. Mag. Ser. 5*, 47(284):109–163, 1899.
- [5] H. Geiger and E. Marsden. On a diffuse reflection of the  $\alpha$ -particles. *Proc. R. Soc. Lond., Ser. A*, 82(557):495–500, 1909.
- [6] E. Rutherford. LVII. The structure of the atom. *Philos. Mag. Ser. 6*, 27(159):488–498, 1914.
- [7] E. Rutherford. LIV. Collision of  $\alpha$  particles with light atoms. IV. An anomalous effect in nitrogen. *Philos. Mag. Ser. 6*, 37(222):581–587, 1919.
- [8] R. L. Sime. *Lise Meitner: a life in physics*. University of California Press, 1996.
- [9] J. Chadwick. Possible existence of a neutron. *Nature*, 129:312, 1932.
- [10] E. Fermi. An attempt of a theory of beta radiation. *Z. Phys.*, 88:161, 1934.
- [11] W. Heisenberg. Über den Bau der Atomkerne. I. *Z. Phys. A*, 77(1):1–11, 1932.
- [12] E. Fermi and W. H. Zinn. *Phys. Rev.*, 70:103, 1946.
- [13] E. Fermi and L. Marshall. Interference phenomena of slow neutrons. *Phys. Rev.*, 71(10):666–677, 1947.

- [14] Yu. B. Zeldovich. *Sov Phys JETP*, 9:1389, 1959.
- [15] L. V. Groshev, V. N. Dvoretzky, A. M. Demidov, Yu. N. Panin, V. I. Lushchikov, Yu. N. Pokotilovsky, A. V. Strelkov, and F. L. Shapiro. Experiments with ultracold neutrons. *Phys. Lett. B*, 34(4):293 – 295, 1971.
- [16] H. Abele, E. Barberio, D. Dubbers, F. Glueck, J. C. Hardy, W. J. Marciano, A. Serebrov, and N. Severijns. Quark mixing, CKM unitarity. *Eur. Phys. J. C*, 33:1, 2004.
- [17] R. E. Lopez and M. S. Turner. Precision prediction for the big-bang abundance of primordial  $^4\text{He}$ . *Phys. Rev. D*, 59:103502/14, 1999.
- [18] C. Amsler, *et al.* (Particle Data Group). The review of particle physics. *Phys. Lett.*, B667:1, 2008. and 2009 partial update for the 2010 edition.
- [19] K. Grotz and H. V. Klapdor. *The Weak Interaction in Nuclear, Particle and Astrophysics*. Adam Hilger, Bristol, Philadelphia and New York, 2nd edition, 1990.
- [20] E. D. Commins and P. H. Bucksbaum. *Weak interactions of leptons and quarks*. Cambridge University Press, 1983.
- [21] M. E. Peskin and D. V. Schroeder. *An Introduction to Quantum Field Theory*. Westview Press, 1995.
- [22] Povh, Rith, Scholz, and Zetsche. *Particles and Nuclei: An Introduction to the Physical Concepts*. Springer-Verlag, 6th edition, 2008.
- [23] Rupert Millard. Mexican hat potential polar. Web page. [http://en.wikipedia.org/wiki/Spontaneous\\_symmetry\\_breaking](http://en.wikipedia.org/wiki/Spontaneous_symmetry_breaking), 2009.
- [24] C. S. Wu, E. Ambler, R. W. Hayward, D. D. Hoppes, and R. P. Hudson. Experimental test of parity conservation in beta decay. *Phys. Rev.*, 105(4):1413–1415, 1957.
- [25] E. C. G. Sudarshan and R. E. Marshak. Chirality invariance and the universal fermi interaction. *Phys. Rev.*, 109(5):1860–1862, 1958.
- [26] R. P. Feynman and M. Gell-Mann. Theory of the fermi interaction. *Phys. Rev.*, 109(1):193–198, 1958.

- [27] Joel Holdsworth. Beta\_negative\_decay.  
Web page. [http://en.wikipedia.org/wiki/Beta\\_decay](http://en.wikipedia.org/wiki/Beta_decay), 2007.
- [28] J. D. Jackson, M. Treiman, and H. W. Wyld Jr. New limit on the D coefficient in polarized neutron decay. *Nucl. Phys.*, 4:206, 1957.
- [29] I. S. Towner and J. C. Hardy. Superaligned  $0^+ \rightarrow 0^+$  nuclear  $\beta$ -decays. *Nucl. Phys. A*, 205(1):33 – 55, 1973.
- [30] W. J. Marciano and A. Sirlin. Improved calculation of electroweak radiative corrections and the value of  $V_{ud}$ . *Phys. Rev. Lett.*, 96(3):032002, 2006.
- [31] K. Krane. *Introductory Nuclear Physics*. John Wiley and Sons, 1988.
- [32] J. C. Hardy and I. S. Towner. Superaligned  $0^+ \rightarrow 0^+$  nuclear  $\beta$ -decays: A new survey with precision tests of the conserved vector current hypothesis and the standard model. *Phys. Rev. C*, 79(5):055502, 2009.
- [33] D. Počanić, E. Frlež, V. A. Baranov, W. Bertl, Ch. Brönnimann, M. Bychkov, J. F. Crawford, M. Daum, N. V. Khomutov, A. S. Korenchenko, S. M. Korenchenko, T. Kozłowski, N. P. Kravchuk, N. A. Kuchinsky, W. Li, R. C. Minehart, D. Mzhavia, B. G. Ritchie, S. Ritt, A. M. Rozhdestvensky, V. V. Sidorkin, L. C. Smith, I. Supek, Z. Tsamalaidze, B. A. VanDevender, Y. Wang, and H.-P. Wirtz. Precise measurement of the  $\pi^+ \rightarrow \pi^0 e^+ \nu$  branching ratio. *Phys. Rev. Lett.*, 93(18):181803, 2004.
- [34] E. W. Kolb and M. S. Turner. *The Early Universe*. Perseus Publishing, 1990.
- [35] G. J. Mathews, T. Kajino, and T. Shima. Big bang nucleosynthesis with a new neutron lifetime. *Phys. Rev. D*, 71(2):021302, 2005.
- [36] Web page, <http://www-thphys.physics.ox.ac.uk/people/subirsarkar/bbn.html>.
- [37] G. Fiorentini, E. Lisi, S. Sarkar, and F. L. Villante. Quantifying uncertainties in primordial nucleosynthesis without monte carlo simulations. *Phys. Rev. D*, 58(6):063506, 1998.
- [38] K. Jedamzik. Non-standard big bang nucleosynthesis scenarios. *arXiv:9805156[astro-ph]*, 1998.

- [39] E. Lisi, S. Sarkar, and F. L. Villante. Big bang nucleosynthesis limit on  $N_\nu$ . *Phys. Rev. D*, 59(12):123520, 1999.
- [40] G. Steigman. Primordial nucleosynthesis: Successes and challenges. *Int. J. Mod. Phys. E*, 15:1, 2006.
- [41] R. Golub, D. Richardson, and S. K. Lamoreaux. *Ultra-Cold Neutrons*. Adam Hilger, 1991.
- [42] K Schreckenbach and W Mampe. The lifetime of the free neutron. *Journal of Physics G: Nuclear and Particle Physics*, 18(1):1, 1992.
- [43] J. S. Nico. Personal communication. 2009.
- [44] A. Serebrov et al. Measurement of the neutron lifetime using a gravitational trap and a low-temperature fomblin coating. *Phys. Lett. B*, 605:72–78, 2005.
- [45] J. Reich, H. Abele, M. Astruc Hoffmann, S. Baeßler, P. v. Bülow, D. Dubbers, V. Nesvizhevsky, U. Peschke, and O. Zimmer. A measurement of the beta asymmetry in neutron decay with PERKEO II. *Nucl. Instr. Meth. Phys. Res., Sect. A*, 440(3):535 – 538, 2000.
- [46] N. Severijns, M. Beck, and O. Naviliat-Cuncic. Tests of the standard electroweak model in nuclear beta decay. *Rev. Mod. Phys.*, 78(3):991, 2006.
- [47] Nathal Severijns. private communication. 2009.
- [48] M. S. Dewey, D. M. Gilliam, J. S. Nico, F. E. Wietfeldt, X. Fei, W. M. Snow, G. L. Greene, J. Pauwels, R. Eykens, A. Lamberty, and J. Van Gestel. Measurement of the neutron lifetime using a proton trap. *Phys. Rev. Lett.*, 91:152302/1–4, 2003.
- [49] M. Dewey, K. Coakley, D. Gilliam, G. Greene, A. Laptev, J. Nico, W. Snow, F. Wietfeldt, and A. Yue. Prospects for a new cold neutron beam measurement of the neutron lifetime. *Nucl. Instr. Meth. A*, 611(2-3):189–192, December 2009.
- [50] V. V. Nesvizhevskii, A. P. Serebrov, R. R. Tal'daev, A. G. Kharitonov, V. P. Alifmenkov, A. V. Streikov, and V. N. Shvetsov. Measurement of the neutron lifetime in a gravitational trap and analysis of experimental errors. *Soviet Physics JETP*, 75:405–412, 1992.

- [51] S. Arzumanov, L. Bondarenko, S. Chernyavsky, W. Drexel, A. Fomin, P. Geltenbort, V. Morozov, Yu. Panin, J. Pendlebury, and K. Schreckenbach. Neutron lifetime value measured by storing ultracold neutrons with detection of inelastically scattered neutrons. *Phys. Lett. B*, 483:15–22, 2000.
- [52] Yu. G. Abov, S. P. Borovlev, V. V. Vasil'ev, V. V. Vladimirkii, and E. N. Mospan. Measurement of the time of storage of ultracold neutrons in a magnetic trap. *Sov. J. Nucl. Phys.*, 38:122–128, 1960.
- [53] V. V. Vladimirkii. Magnetic mirrors, channels and bottles for cold neutrons. *Sov Phys JETP*, 12:740–746, 1961.
- [54] K.-J. Kügler, K. Moritz, W. Paul, and U. Trinks. Nestor: A magnetic storage ring for slow neutrons. *Nucl. Instr. Meth. A*, 228:240–258, 1985.
- [55] N. Niehues. *Untersuchungen an einer magnetischen flasche zur speicherung von neutronen*. PhD thesis, Friedrich Wilhelm University of Bonn, 1983.
- [56] V. F. Ezhov, V. F. Andreev, A. A. Glushkov, A. G. Glushkov, M. N. Groshev, V. A. Knyazkov, G. B. Krygin, V. L. Ryabov, and A. P. Serebrov. First ever storage of ultracold neutrons in a magnetic trap made of permanent magnets. *J. Res. Natl. Inst. Stand. Technol.*, 110:345–350, 2005.
- [57] J. D. Bowman and S. I. Pentilla. On the measurement of the neutron lifetime using ultracold neutrons in a vacuum quadrupole trap. *J. Res. Natl. Inst. Stand. Technol.*, 110(4), 2005.
- [58] L. Yang. *Towards Precision Measurement of the Neutron Lifetime using Magnetically Trapped Neutrons*. PhD thesis, Harvard University, 2006.
- [59] R. Golub and J. M. Pendlebury. Super-thermal sources of ultra-cold neutrons. *Phys. Lett.*, 53A:133–135, 1975.
- [60] D. N. McKinsey, C. R. Brome, J. S. Butterworth, S. N. Dzhosyuk, P. R. Huffman, C. E. H. Mattoni, J. M. Doyle, R. Golub, and K. Habicht. Radiative decay of the metastable  $\text{He}_2(a^3\sigma_u^+)$  molecule in liquid helium. *Phys. Rev. A*, 59:200–204, 1999.

- [61] D. N. McKinsey, C. R. Brome, J. S. Butterworth, R. Golub, K. Habicht, P. R. Huffman, S. K. Lamoreaux, C. E. H. Mattoni, and J. M. Doyle. Fluorescence efficiencies of thin scintillating films in the extreme ultraviolet spectral region. *Nucl. Instr. Meth. B*, 132:351, 1997.
- [62] S. N. Dzhosyuk. *Magnetic Trapping of Neutrons for Measurement of the Neutron Lifetime*. PhD thesis, Harvard University, 2004.
- [63] R. E. Williams and J. M. Rowe. Developments in neutron beam devices and an advanced cold source for the nist research reactor. *Physica B*, 311:117–122, 2002.
- [64] L. Landau. Theory of the superfluidity of helium II. *Phys. Rev.*, 60:356–358, 1941.
- [65] J. L. Yarnell, G. P. Arnold, P. J. Bendt, and E. C. Kerr. Excitations in liquid helium: Neutron scattering measurements. *Phys. Rev.*, 113(6):1379–1386, Mar 1959.
- [66] P. J. Bendt, R. D. Cowan, and J. L. Yarnell. Excitations in liquid helium: Thermodynamic calculations. *Phys. Rev.*, 113(6):1386–1395, 1959.
- [67] C. E. H. Mattoni. *Magnetic trapping of ultracold neutrons produced from a monochromatic cold neutron beam*. PhD thesis, Harvard University, 2002.
- [68] L. Yang, C. R. Brome, J. S. Butterworth, S. N. Dzhosyuk, C. E. H. Mattoni, D. N. McKinsey, R. A. Michniak, J. M. Doyle, R. Golub, E. Korobkina, C. M. O’Shaughnessy, G. R. Palmquist, P.-N. Seo, P. R. Huffman, K. J. Coakley, H. P. Mumm, A. K. Thompson, G. L. Yang, and S. K. Lamoreaux. Invited article: Development of high-field superconducting ioffe magnetic traps. *Rev. Sci. Instrum.*, 79:031301, 2008.
- [69] K. Tsuchiya, K. Egawa, K. Endo, Y. Morita, and N. Ohuchi. Performance of the eight superconducting quadrupole magnets for the tristan low-beta insertions. *IEEE Trans. Magn.*, 27(2):1940, 1991.
- [70] Web page, <http://www.matweb.com>.
- [71] F. Pobell. *Matter and Methods at Low Temperatures*. Springer-Verlag, Berlin, 2nd edition, 1996.

- [72] C. R. Brome. *Magnetic Trapping of Ultracold Neutrons*. PhD thesis, Harvard University, 2000.
- [73] R. P. Reed and A. F. Clark, editors. *Materials at Low Temperature*. American Society for Metals, Metals Park, OH, 1983.
- [74] G. Citver, S. Feher, P. J. Limon, D. Orris, T. Peterson, S. Sylvester, M. A. Tartaglia, and J. C. Tompkins. HTS power leads test results. *Proc. of the 1999 Particle Accelerator Conf.*, pages 1420–22, 1999.
- [75] G. Citver, S. Feher, T. J. Peterson, and C. D. Sylvester. Thermal tests of 6kA HTS current leads for the tevatron. *Proc. of the 1999 Cryogenic Engineering Conf.*, 1999.
- [76] J.L.H. Lindenhovius, E.M. Hornsveld, A. den Ouden, W.A.J. Wessel, and H.H.J. ten Kate. Powder-in-tube (PIT) Nb3Sn conductors for high-field magnets. *IEEE Trans. Appl. Supercond.*, 10(1):975–978, 2000.
- [77] J. S. Butterworth, C. R. Brome, P. R. Huffman, C. E. H. Mattoni, D. N. McKinsey, and J. M. Doyle. A removable cryogenic window for transmission of light and neutrons. *Rev. Sci. Inst.*, 69:3998, 1998.
- [78] Hiroyuki Fujishiro, Manabu Ikebe, Toshihiro Kashima, and Atsuhiko Yamanaka. Thermal conductivity and diffusivity of high-strength polymer fibers. *Japanese Journal of Applied Physics*, 36(Part 1, No. 9A):5633–5637, 1997.
- [79] G. Ventura, M. Barucci, E. Gottardi, and I. Peroni. Low temperature thermal conductivity of Kevlar. *Cryogenics*, 40(7):489–491, 2000.
- [80] P. Wikus, E. Figueroa-Feliciano, S. A. Hertel, S. W. Leman, K. A. McCarthy, and J. M. Rutherford. The thermal conductivity of high modulus Zylon fibers between 400mK and 4K. *Cryogenics*, 48(11-12):515–517, 2008.
- [81] E. W. Washburn. The dynamics of capillary flow. *Phys. Rev.*, 17(3):273–283, 1921.
- [82] V. F. Sears. Neutron scattering lengths and cross sections. *Neutron News*, 3(3):26–37, 1992.
- [83] S. N. Dzhosyuk, C. E. H. Mattoni, D. N. McKinsey, A. K. Thompson, L. Yang, J. M. Doyle, and P. R. Huffman. Neutron-induced luminescence and activation in neutron

- shielding and scintillation detection materials at cryogenic temperatures. *Nucl. Instr. Meth. B*, 217:457–470, 2004.
- [84] Parker o-ring handbook, web page <http://www.parker.com>.
- [85] T. Massam. Guide 7, a general program for evaluating the properties of scintillation and cherenkov counter optical systems. Technical report, CERN, 1976.
- [86] R. Winston, J. C. Miano, W. T. Welford, and P. Bentez. *Nonimaging Optics*. Elsevier Academic Press, 2005.
- [87] Inductiveload. Lambert’s cosine law.  
Web page. <http://en.wikipedia.org/wiki/Lambert2008>.
- [88] D. N. McKinsey. *Detecting magnetically trapped neutrons: Liquid helium as a scintillator*. PhD thesis, Harvard University, 2002.
- [89] D. N. McKinsey, C. R. Brome, J. S. Butterworth, S. N. Dzhosyuk, R. Golub, K. Habicht, P. R. Huffman, C. E. H. Mattoni, L. Yang, and J. M. Doyle. Detecting ionizing radiation in liquid helium using wavelength shifting light collection. *Nucl. Instr. Meth. A*, 516:475–485, 2004.
- [90] M. H. Edwards. The index of refraction of liquid helium. *Canadian Journal of Physics*, 34:898–900, 1956.
- [91] Burle 8854 specifications sheet. Technical report, Burle Technologies.
- [92] T. A. Osswald and D. W. Green. *Materials Science of Polymers for Engineers*. Hanser Gardner Publications, 2003.
- [93] W. Frati, M. Lowry, and P. Skensved. Comparison of input parameters used for photon transport in the UCI and Queens Monte Carlos and the output of their algorithms. Technical report, SNO-STR-91-024, 1991.
- [94] N. Phan. Acrylic attenuation measurements for the miniclean dark matter detector, April 2009. University of New Mexico, Honors Thesis.
- [95] Web page. <http://www.melleroptics.com>.
- [96] Web page. <http://www.cvilaser.com>.

- [97] Web page. <http://www.mellesgriot.com>.
- [98] R. H. Perry and D. W. Green. *Perry's Chemical Engineering Handbook*. McGraw-Hill, 7th edition, 1997.
- [99] Web page. <http://www.thermionics.com>.
- [100] E. W. Washburn. *International Critical Tables of Numerical Data, Physics, Chemistry, and Technology*. Knovel, National Research Council (U.S), International Research Council, National Academy of Sciences (U.S.), 1st edition, 2003.
- [101] Prager J. C. *Environmental Containment Reference Databook*. Van Nostrand Reinhold, 1997.
- [102] J. Hoste D. DeSoete, R. Gijbels. *Neutron Activation Analysis*. Wiley-Interscience, 1972.
- [103] P. Hughes. Gamma survey write up. 2009.
- [104] J. H. Hubbell and S. M. Seltzer. Tables of x-ray mass attenuation coefficients and mass energy-absorption coefficients (version 1.4). Available: <http://physics.nist.gov/xaamdi> [2010, April 8], 2004.
- [105] D. Marley and H. P. Mumm. Design and development of a muon veto system for an ultra-cold neutron lifetime experiment. Technical report, NIST Summer Undergraduate Research Fellowship, 2009.
- [106] B. Rossi. Interpretation of cosmic-ray phenomena. *Rev. Mod. Phys.*, 20(3):537–583, Jul 1948.
- [107] P. V. E. McClintock. An apparatus for preparing isotopically pure  $^4\text{He}$ . *Cryogenics*, 18:201–208, 1978.
- [108] N. Metropolis and S. Ulam. The monte carlo method. *J. Am. Stat. Assn.*, 44(247):335–341, 1949.
- [109] K. J. Coakley, J. M. Doyle, S. N. Dzhosyuk, P. R. Huffman, and L. Yang. Chaotic scattering and escape times of marginally trapped ultracold neutrons. *J. Res. Natl. Inst. Stand. Techol.*, 110:367–376, 2005.

- [110] Web page. <http://www.esrf.eu/accelerators/groups/insertiondevices/software/radia>.
- [111] A. V. Antonov, A. I. Isakov, M. V. Kazarnovskii, and U. E. Solidov. *Sov. Phys. JETP*, 10:241, 1969.
- [112] J. S. Walker and J. Gathright. Exploring one-dimensional quantum mechanics with transfer matrices. *Am. J. Phys.*, 62(5):408–422, 1994.
- [113] A. Steyerl, S. S. Malik, A. M. Desai, and C. Kaufman. Surface roughness effect on ultracold neutron interaction with a wall and implications for computer simulations. *arXiv:0911.4115v2[cond-mat.other]*, 2009.
- [114] V. K. Ignatovich. *The physics of Ultracold Neutrons*, volume 5 of *Oxford series on neutron scattering in condensed matter*. Oxford University Press, 1990.
- [115] K. J. Coakley. Personal communication. 2010.

# Appendix

## Appendix A

# GuideIt Input

The following is an input file for 'filecm', part of a suite of programs in generating and interpreting the monte carlo predictions of the optics ray tracing program GuideIt. This file would be input to 'filecm' which then generates the geometry of the light collection system for the UCN Lifetime apparatus in a properly formatted input file for GuideIt. From this file a program called 'scriptit' will generate an AutoCAD script file for visualizing the geometry. When an option called diagnostic-tracking is turned on, the text output from guideit will include the coordinate traces for all of the photons tracked. A program called 'rayplot' writes an AutoCAD script for visualizing the tracked photons. If there are problems with the geometry these additional programs give the capability of locating the errors.

```
; This is an input file for FileCm which defines GuideIt geometry, histograms,
; and running conditions for the optical elements of the neutron lifetime
; apparatus. The 430 nm photons are generated with the proper distribution in
; the TPB using the proper generation file GUIDEGEO.INC The distribution is
; generated by spectator photons originating at the source location.
;
; The following externally defined "set" variables are recognized (and must
; be set before this is run):
; \O          The output file name (extension is .in)
; \Z          The distance of the source in the cell from the beam stop
;
; Print the current values of the set variables.
SET
;
; Define material parameters (N => index of refraction, A => attenuation length,
; R => surface roughness)
; Vacuum
CALC VACN = 1
CALC VACA = 100000
```

```
; Liquid Helium: for now assume that it is just like vacuum.
CALC LHEN = VACN
CALC LHEA = VACA
; Lucite (UVT acrylic): Index of refraction is interpolated to 430 nm from
; a plot in Materials Science of Polymers for Engineers (Tim A. Osswald and
; Georg Menges). Bulk attenuation can vary from 150 to 500 cm.
; Surface roughness is the approximately that of a polished surface (not
; a cast surface).
CALC LUCITEN = 1.5085
CALC LUCITEA = 260
; 11/27/06 attanuation was 150, changed such that MarkII sim matches data
CALC LUCITER = .99
; Glass: The Burle 8854 photomultiplier has a window made of UV Transmitting
; glass (Corning #9741 or equivalent). The following index of refraction
; is from the PMT data sheet at 404.7 nm. The attenuation is an
; approximate value. Surface roughness is the recommended value for a
; cast surface.
CALC GLASSN = 1.48
CALC GLASSA = 300
CALC GLASSR = .999
; Sapphire: Index of refraction is interpolated for 430 nm from a
; table of the "ordinary" index of refraction on the Meller Optics, Inc.
; web page at www.melleroptics.com. This agrees to 5 places with
; indices of refraction from (fitted?) dispersion relations found
; on the Mells Griot and CVI Laser web sites. Surface roughness assumed to
; be like that of glass. The bulk attenuation is also assumed to be like glass.
; Since the material in the model is quite thin, this probably doesn't matter
; much.
CALC SAPPHN = 1.7820
CALC SAPPHA = GLASSA
CALC SAPPHR = GLASSR
; Single crystal quartz: Index of refraction from the Meller Optics, Inc. web
; page at www.melleroptics.com. The number is very close to the value
; interpolated to 430 nm from a plot in Materials Science of Polymers for
; Engineers (Tim A. Osswald and Georg Menges) (i.e. 1.5537). The
; (fitted?) dispersion relation found on the CVI Laser website gives 1.5544
; Surface roughness assumed to be like that of glass. Similarly, we assume
; bulk attenuation is the same as glass.
CALC QUARTZN = 1.5538
CALC QUARTZA = GLASSA
CALC QUARTZR = GLASSR
; Boron Oxide (B2O3): Various values of index of refraction are quoted in
; references (but at what wavelength?): 1.459 (Perry's Chemical Engineering
; Handbook, 7th Ed.), 1.462 (Thermionics web site), 1.464 (International
; Critical Tables of Numerical Data, Physics, Chemistry, and Technology, 1st
; Electronic Ed.), 1.485 (Environmental Contaminant Reference Databook).
; Well use an intermediate value. The surface roughness and attenuation
; are assumed to be the same as glass.
CALC B2O3N = 1.464
CALC B2O3A = GLASSA
```

```

CALC B203R = GLASSR
;
; Metal parameters
; The following is the default
; METAL-CRUMPLE-ANGLE 5
; METAL-SURFACE 0.8
; The following is for a smooth surface (mylar?)
METAL-CRUMPLE-ANGLE 0
METAL-SURFACE 1
; The following is for a dull smooth surface (mylar?)
; METAL-CRUMPLE-ANGLE 0
; METAL-SURFACE 0.8
;
; Define some variables having to do with the geometry.
; This small distance is used to shift two surfaces which
; normally would lie on top of eachother. Using such slightly
; shifted surfaces, one can effectively create donut shaped
; surfaces. This distance must be insignificantly small compared
; to other distances in the problem but not so small that guideit
; doesn't see it.
CALC EPS = 0.02
;
CALC ZPOS = \Z
CALC CELL_THICK = 75
CALC CELL_RADIUS = 11.43/2
; B203 beam stop thickness in cm
CALC B203_THICK = 1.2
; B203 beam stop radius in cm
CALC B203_RADIUS = 11.43/2
; Cell guide length in cm
CALC CELLGUIDE_THICK = 69.815
; Cell guide radius in cm
CALC CELLGUIDE_RADIUS = B203_RADIUS
; Distance between the end of the cell guide and the snout window
CALC CELLSNOUT_GAP = 0.01
; Thickness of the acrylic snout window
CALC SNOUT_THICK = 0.48
; Radius of the acrylic snout window
CALC SNOUT_RADIUS = 12.15/2
; Distance between the snout window and the 4 K acrylic window
CALC SNOUTFOURK_GAP = 0.1
; 4 K acrylic window thickness in cm
CALC FOURK_THICK = 0.635
; 4 K acrylic window radius in cm (MarkII was 19)
CALC FOURK_RADIUS = 20.32/2
; Quartz window thickness in cm
CALC QUARTZ_THICK = 0.15
; Quartz window radius in cm (MarkII was 15.2)
CALC QUARTZ_RADIUS = 23/2
; Distance between the quartz window and the sapphire window was 1.2

```

```

CALC QUARTZSAPPHIRE_GAP = 0.1
; Offset positioning for the 77 K guide
CALC OFFSET_POS = 1
; Sapphire window thickness in cm
CALC SAPPHIRE_THICK = 0.05
; Sapphire window radius in cm(MarkII was 10, probably don't need for markIII)
CALC SAPPHIRE_RADIUS = 15/2
; Epoxy spot radius
CALC EPOXY_RADIUS = 0.59/2
; Distace to O-Ring (MarkII was 20)
CALC ORING_DIS = 47
; Thickness of the O-Ring
CALC ORING_THICK = 0.5
; 77 K light guide length in cm
CALC SEVENTY7K_THICK = 38.1
; 77 K light guide radius in cm
CALC SEVENTY7K_RADIUS = 11.43/2
; Distance from WCS origin to the center of the PMT end of the 77 K light guide
CALC SEVENTY7K_Z = EPS+B203_THICK+EPS+CELLGUIDE_THICK+CELLSNOUT_GAP+SNOUT_THICK
CALC SEVENTY7K_Z = SEVENTY7K_Z+SNOUTFOURK_GAP+FOURK_THICK+QUARTZ_THICK
CALC SEVENTY7K_Z = SEVENTY7K_Z+QUARTZSAPPHIRE_GAP+SAPPHIRE_THICK+SEVENTY7K_THICK
CALC SEVENTY7K_Z
; Splitter cylinder radius in cm(MarkII was 11.5)
CALC SPLIT_RADIUS = 11.43/2
; Splitter cylinder length in cm
CALC SPLIT_THICK = 2*SPLIT_RADIUS+1.25
; Angle of splitter axis from Z axis (deg)
CALC SPLIT_ANGLE = 45
; Half of long axis of elliptical face of the splitter where
; it attaches to the 77 K light guide
CALC SPLIT_LONG = SPLIT_RADIUS/COSD(SPLIT_ANGLE)
; Thickness of coupler at the edge (the thickest part) in cm
CALC COUPLER_THICK = 1.9936
; Radius of the coupler spherical surface in cm
CALC COUPLER_RADIUS = 12.8799
; Distance from splitter to center of curvature of the spherical coupler surface
CALC COUPLER_CENTER = COUPLER_THICK+SQRT(COUPLER_RADIUS^2-SPLIT_RADIUS^2)
CALC COUPLER_CENTER
; Thickness of the coupler in the center (the thinnest part) in cm
CALC COUPLER_THIN = COUPLER_CENTER-COUPLER_RADIUS
CALC COUPLER_THIN
;
; The number of sequences is calculated as we go. This
; allows additional sequences to be added without having to re-generate
; all the sequence numbers. The first sequence is the one farthest from
; the PMTs.
CALC NSEQ = 0
;
; We define the WCS to be centered in the middle of the surface furthest
; from the PMTs. The Z axis is assumed to be the axis of (most of)

```

```

; the cylindrical parts. +Z points toward the PMTs. The PMTs are assumed
; to be centered on the X-Z plane.
;
; +-----+
; | The active cell region |
; +-----+
CALC NSEQ = NSEQ+1
NUMBER-OF-SEQ NSEQ
D-SURFACE-SEQ NSEQ
CALC SOURCE_SEQ = NSEQ
;
; Make the circular surface away from the PMTs.
D-GATE-TYPE BOTGATE
D-SURFACE-GATE 1
D-SURFACE-DETAIL NONE
D-SURFACE-ROUGHNESS 1
D-INTERNAL-INDEX LHEN
D-ATTENUATION-LEN LHEA
D-EXTERNAL-INDEX LHEN
D-REALM OUTSIDE
WCS
CIRCULAR CELL_RADIUS
;
; Create the edge of the cell in the first region
; The gortex is dealt as a completely diffusely
; reflecting surface with a reflectivity of 0.95
D-GATE-TYPE NONE
D-SURFACE-DETAIL PAPER
D-SPECULARITY -0.93
D-ABSORPTION 0.90
D-REALM INSIDE
CYLINDER CELL_RADIUS,CELL_THICK
;
; Create the circular surface nearest the PMTs, a gate into the
; next sequence.
D-GATE-TYPE TOPGATE
D-SURFACE-GATE 2
D-SURFACE-DETAIL NONE
D-SURFACE-ROUGHNESS LUCITER
UCS 0,0,CELL_THICK
CIRCULAR CELL_RADIUS
;
; +-----+
; | The B203 beam stop |
; +-----+
; CALC NSEQ = NSEQ+1
; NUMBER-OF-SEQ NSEQ
; D-SURFACE-SEQ NSEQ
;
; Make the circular surface away from the PMTs.

```

```

; D-GATE-TYPE BOTGATE
; D-SURFACE-GATE 1
; D-INTERNAL-INDEX B203N
; D-ATTENUATION-LEN B203A
; D-EXTERNAL-INDEX LHEN
; D-REALM OUTSIDE
; CIRCULAR B203_RADIUS
;
; Create the edge of the beam stop. I think this was wrapped
; with Tyvek (randomly oriented high density polyethylene). This
; is a diffuse white surface -- Assume D-specularity 1 and
; the absorbtion 0.90 this is from data that KAMland took at TUNL
; The specularity remains defined as 0.93 as that has been shown to
; be consistent with the data that was taken at NCSU.
; D-GATE-TYPE NONE
; D-SURFACE-DETAIL PAPER
; D-REALM INSIDE
; CYLINDER B203_RADIUS,B203_THICK
;
; Create the circular surface nearest the PMTs, a gate into the
; next sequence.
; D-SURFACE-DETAIL NONE
; D-GATE-TYPE TOPGATE
; D-SURFACE-GATE 2
; UCS 0,0,B203_THICK
; CIRCULAR B203_RADIUS
;
; +-----+
; | LHe volume after the beam stop |
; +-----+
; CALC NSEQ = NSEQ+1
; NUMBER-OF-SEQ NSEQ
; D-SURFACE-SEQ NSEQ
;
; Make the circular surface away from the PMTs.
; D-GATE-TYPE BOTGATE
; D-SURFACE-GATE 1
; D-INTERNAL-INDEX LHEN
; D-ATTENUATION-LEN LHEA
; D-EXTERNAL-INDEX B203N
; D-REALM OUTSIDE
; CIRCULAR B203_RADIUS
;
; Create the edge of post-beam-stop LHe volume
; D-GATE-TYPE NONE
; D-SURFACE-DETAIL PAPER
; D-EXTERNAL-INDEX LHEN
; D-REALM INSIDE
; CYLINDER B203_RADIUS,EPS
;

```

```

; Create the circular surface nearest the PMTs, a gate into the
; next sequence.
; D-SURFACE-DETAIL NONE
; D-GATE-TYPE TOPGATE
; D-SURFACE-GATE 2
; D-SURFACE-ROUGHNESS LUCITER
; D-EXTERNAL-INDEX LUCITEN
; UCS 0,0,EPS
; CIRCULAR B203_RADIUS
;
; +-----+
; | The cell light guide |
; +-----+
CALC NSEQ = NSEQ+1
NUMBER-OF-SEQ NSEQ
D-SURFACE-SEQ NSEQ
;
; Make the circular surface away from the PMTs.
D-GATE-TYPE BOTGATE
D-SURFACE-GATE 1
D-INTERNAL-INDEX LUCITEN
D-ATTENUATION-LEN LUCITEA
D-EXTERNAL-INDEX LHEN
D-REALM OUTSIDE
CIRCULAR CELLGUIDE_RADIUS
;
; Create the edge of the cell light guide. This was wrapped
; with Tyvek (randomly oriented high density polyethylene). This
; is a diffuse white surface
D-SURFACE-DETAIL PAPER
D-GATE-TYPE NONE
D-REALM INSIDE
CYLINDER CELLGUIDE_RADIUS,CELLGUIDE_THICK
;
; Create the circular surface nearest the PMTs, a gate into the
; next sequence.
D-SURFACE-DETAIL NONE
D-GATE-TYPE TOPGATE
D-SURFACE-GATE 2
UCS 0,0,CELLGUIDE_THICK
CIRCULAR CELLGUIDE_RADIUS
;
; +-----+
; | The gap between the cell light guide and snout window |
; +-----+
CALC NSEQ = NSEQ+1
NUMBER-OF-SEQ NSEQ
D-SURFACE-SEQ NSEQ
;
; Make the circular surface away from the PMTs.

```

```

D-GATE-TYPE BOTGATE
D-SURFACE-GATE 1
D-SURFACE-ROUGHNESS LUCITER
D-INTERNAL-INDEX LHEN
D-EXTERNAL-INDEX LUCITEN
D-ATTENUATION-LEN LHEA
D-REALM OUTSIDE
CIRCULAR CELLGUIDE_RADIUS
;
; Create an edge for the gap. We use a truncated cone surface to
; go from the cell guide radius to the acrylic window radius. Since
; the surface has both internal and external indices of refraction
; equal, impinging photons are lost through the surface. In reality,
; they would probably hit the inside of the aluminum snout or possibly
; part of the cylindrical acrylic ring on the snout. This could probably
; be fixed up with a bit more work.
D-GATE-TYPE NONE
D-EXTERNAL-INDEX LHEN
D-REALM INSIDE
CONE CELLGUIDE_RADIUS,SNOUT_RADIUS,CELLSNOUT_GAP
;
; Create the circular surface nearest the PMTs, a gate into the
; next sequence.
D-GATE-TYPE TOPGATE
D-SURFACE-GATE 2
D-EXTERNAL-INDEX LUCITEN
UCS 0,0,CELLSNOUT_GAP
CIRCULAR SNOUT_RADIUS
;
; +-----+
; | The acrylic snout window |
; +-----+
CALC NSEQ = NSEQ+1
NUMBER-OF-SEQ NSEQ
D-SURFACE-SEQ NSEQ
;
; Make the circular surface away from the PMTs.
D-GATE-TYPE BOTGATE
D-SURFACE-GATE 1
D-SURFACE-ROUGHNESS LUCITER
D-EXTERNAL-INDEX LHEN
D-INTERNAL-INDEX LUCITEN
D-ATTENUATION-LEN LUCITEA
D-REALM OUTSIDE
CIRCULAR SNOUT_RADIUS
;
; Create the edge of the snout window.
D-GATE-TYPE NONE
D-EXTERNAL-INDEX VACN
D-REALM INSIDE

```

```

CYLINDER SNOUT_RADIUS,SNOUT_THICK
;
; Create the circular surface nearest the PMTs, a gate into the
; next sequence.
D-GATE-TYPE TOPGATE
D-SURFACE-GATE 2
UCS 0,0,SNOUT_THICK
CIRCULAR SNOUT_RADIUS
;
; +-----+
; | The gap between the snout window and the 4 K acrylic window |
; +-----+
CALC NSEQ = NSEQ+1
NUMBER-OF-SEQ NSEQ
D-SURFACE-SEQ NSEQ
;
; Make the circular surface away from the PMTs.
D-GATE-TYPE BOTGATE
D-SURFACE-GATE 1
D-SURFACE-ROUGHNESS LUCITER
D-INTERNAL-INDEX VACN
D-EXTERNAL-INDEX LUCITEN
D-ATTENUATION-LEN VACA
D-REALM OUTSIDE
CIRCULAR SNOUT_RADIUS
;
; Create an edge for the gap. We use a truncated cone surface to
; go from the cell guide radius to the acrylic window radius. Since
; the surface has both internal and external indices of refraction
; equal, impinging photons are lost through the surface. In reality,
; they would probably hit parts of the 4 K window clamping assembly
; or the inside of the internal vacuum chamber (IVC). This could
; probably be fixed up with a bit more work.
D-GATE-TYPE NONE
D-EXTERNAL-INDEX VACN
D-REALM INSIDE
CONE SNOUT_RADIUS,FOURK_RADIUS,SNOUTFOURK_GAP
;
; Create the circular surface nearest the PMTs, a gate into the
; next sequence. In reality, this surface is partially obscured
; by the 4 K window clamping assembly
D-GATE-TYPE TOPGATE
D-SURFACE-GATE 2
D-EXTERNAL-INDEX LUCITEN
UCS 0,0,SNOUTFOURK_GAP
CIRCULAR FOURK_RADIUS
;
; +-----+
; | The acrylic 4 K window |
; +-----+

```

```

CALC NSEQ = NSEQ+1
NUMBER-OF-SEQ NSEQ
D-SURFACE-SEQ NSEQ
;
; Make the circular surface away from the PMTs.
D-GATE-TYPE BOTGATE
D-SURFACE-GATE 1
D-SURFACE-ROUGHNESS LUCITER
D-EXTERNAL-INDEX VACN
D-INTERNAL-INDEX LUCITEN
D-ATTENUATION-LEN LUCITEA
D-REALM OUTSIDE
CIRCULAR FOURK_RADIUS
;
; Create the edge of the 4 K window. This is surrounded by
; the window clamping assembly, probably a dull metal surface.
; Since only one type of "metal" can be defined and we need
; a shiny surface for the splitter, we will treat this surface
; as having no surface detail. The length is slightly extended
; to allow a donut shape for the obscured part of the near-PMT
; face
D-GATE-TYPE NONE
D-REALM INSIDE
CYLINDER FOURK_RADIUS,FOURK_THICK+EPS
;
; Create the circular surface which is a gate into the
; quartz window. We assume perfect contact between the acrylic
; 4 K window and the and quartz window. In reality there is probably
; vacuum. This could be fixed up.
D-GATE-TYPE TOPGATE
D-SURFACE-GATE 2
D-EXTERNAL-INDEX QUARTZN
UCS 0,0,FOURK_THICK
CIRCULAR QUARTZ_RADIUS
;
; Also create a little anulus, another gate into the quartz,
; to make the donut-shaped region that doesn't pass photons
; into the quartz
D-SURFACE-GATE 3
CYLINDER QUARTZ_RADIUS,EPS
;
; Make a surface shifted slightly toward the PMTs from the surfaces
; that pass photons into the quartz to account for the fact that
; the 4K window is larger in radius than the quartz. This effectively
; creates a donut-shaped surface because photons will always hit
; the quartz gate first if they are at small radius.
D-GATE-TYPE NONE
D-EXTERNAL-INDEX VACN
UCS 0,0,EPS
CIRCULAR FOURK_RADIUS

```

```

UCS 0,0,-EPS
;
; +-----+
; | The quartz window |
; +-----+
; CALC NSEQ = NSEQ+1
; NUMBER-OF-SEQ NSEQ
; D-SURFACE-SEQ NSEQ
;
; Make the circular surface away from the PMTs. We assume perfect
; contact between the acrylic 4 K window and the quartz window.
; In reality there is probably vacuum. This could be fixed up.
; D-GATE-TYPE BOTGATE
; D-SURFACE-GATE 1
; D-SURFACE-ROUGHNESS QUARTZR
; D-EXTERNAL-INDEX LUCITEN
; D-INTERNAL-INDEX QUARTZN
; D-ATTENUATION-LEN QUARTZA
; D-REALM OUTSIDE
; CIRCULAR QUARTZ_RADIUS
;
; Create the edge of the quartz window.
; D-GATE-TYPE NONE
; D-EXTERNAL-INDEX VACN
; D-REALM INSIDE
; CYLINDER QUARTZ_RADIUS,QUARTZ_THICK
;
; Create the circular surface nearest the PMTs, a gate into the
; next sequence.
; D-GATE-TYPE TOPGATE
; D-SURFACE-GATE 2
; UCS 0,0,QUARTZ_THICK
; CIRCULAR QUARTZ_RADIUS
;
; +-----+
; | The gap between the quartz window and the sapphire window |
; +-----+
CALC NSEQ = NSEQ+1
NUMBER-OF-SEQ NSEQ
D-SURFACE-SEQ NSEQ
;
; Make the circular surface away from the PMTs.
D-GATE-TYPE BOTGATE
D-SURFACE-GATE 1
D-SURFACE-ROUGHNESS QUARTZR
D-INTERNAL-INDEX VACN
D-EXTERNAL-INDEX QUARTZN
D-ATTENUATION-LEN VACA
D-REALM OUTSIDE
CIRCULAR FOURK_RADIUS

```

```

;
; To offset the 77 K guide from the cell we instead of a cone use a
; cylinder large enough to cover both surfaces.
;
D-GATE-TYPE NONE
D-EXTERNAL-INDEX VACN
D-REALM INSIDE
CYLINDER FOURK_RADIUS,QUARTZSAPPHIRE_GAP+EPS
;
D-GATE-TYPE TOPGATE
D-SURFACE-GATE 2
D-SURFACE-ROUGHNESS LUCITER
D-INTERNAL-INDEX VACN
D-EXTERNAL-INDEX LUCITEN
UCS 0,0,QUARTZSAPPHIRE_GAP
CIRCULAR SEVENTY7K_RADIUS
;
; D-REALM OUTSIDE
D-SURFACE-GATE 3
CYLINDER SEVENTY7K_RADIUS,EPS
UCS 0,0,EPS
;
D-GATE-TYPE GATE
D-SURFACE-GATE 4
D-EXTERNAL-INDEX VACN
CIRCULAR FOURK_RADIUS
UCS 0,0,-EPS
;
; Create the circular surface nearest the PMTs, a gate into the
; next sequence. In reality, this surface is partially obscured
; by the sapphire window clamping assembly
; D-REALM INSIDE
; D-GATE-TYPE TOPGATE
; D-SURFACE-GATE 4
; D-SURFACE-ROUGHNESS SAPPHR
; D-INTERNAL-INDEX VACN
; D-EXTERNAL-INDEX SAPPHN
; CIRCULAR SAPPHIRE_RADIUS
;
; 1/19/05 run with no Sapphire Window
; +-----+
; | The sapphire window |
; +-----+
; CALC NSEQ = NSEQ+1
; NUMBER-OF-SEQ NSEQ
; D-SURFACE-SEQ NSEQ
;
; Make the circular surface away from the PMTs.
; D-GATE-TYPE BOTGATE
; D-SURFACE-GATE 1

```

```

; D-SURFACE-ROUGHNESS SAPPHIRER
; D-EXTERNAL-INDEX VACN
; D-INTERNAL-INDEX SAPPHN
; D-ATTENUATION-LEN SAPPHA
; D-REALM OUTSIDE
; CIRCULAR SAPPHIRE_RADIUS
;
; Create the edge of the sapphire window. We ignore the little
; clamps that hold the sapphire to the 77 K guide.
; D-GATE-TYPE NONE
; D-REALM INSIDE
; CYLINDER SAPPHIRE_RADIUS,SAPPHIRE_THICK
;
; Create the circular surface which is a gate into the
; 77 K guide. We assume perfect contact between the lucite guide
; and sapphire window. In reality there is a drop of stycast and
; probably vacuum. This could be fixed up.
; D-GATE-TYPE TOPGATE
; D-SURFACE-GATE 2
; D-EXTERNAL-INDEX VACN
; UCS 0,0,SAPPHIRE_THICK
; CIRCULAR SAPPHIRE_RADIUS
;
; D-GATE-TYPE TOPGATE
; D-SURFACE-GATE 3
; CYLINDER EPOXY_RADIUS,2*EPS
;
; D-REALM INSIDE
; D-EXTERNAL-INDEX LUCITEN
; D-GATE-TYPE UP-SEQUENCE-2
; D-SURFACE-GATE 4
; UCS 0,0,2*EPS
; CIRCULAR EPOXY_RADIUS
;
;
; +-----+
; | Vacuum Gap |
; +-----+
;
; CALC NSEQ = NSEQ+1
; NUMBER-OF-SEQ NSEQ
; D-SURFACE-SEQ NSEQ
;
; D-GATE-TYPE BOTGATE
; D-SURFACE-GATE 1
; D-EXTERNAL-INDEX SAPPHN
; D-INTERNAL-INDEX VACN
; D-ATTENUATION-LEN VACA
; D-REALM OUTSIDE
; UCS 0,0,-2*EPS

```

```

; CIRCULAR SAPPHIRE_RADIUS
;
; D-GATE-TYPE BOTGATE
; D-SURFACE-GATE 2
; CYLINDER EPOXY_RADIUS,2*EPS
;
; D-GATE-TYPE NONE
; D-REALM INSIDE
; D-EXTERNAL-INDEX VACN
; CONE SAPPHIRE_RADIUS,SEVENTY7K_RADIUS,2*EPS
; UCS 0,0,2*EPS
;
; D-GATE-TYPE TOPGATE
; D-SURFACE-GATE 3
; D-EXTERNAL-INDEX LUCITEN
; CIRCULAR SEVENTY7K_RADIUS
;
; +-----+
; | The 77 K light guide |
; +-----+
CALC NSEQ = NSEQ+1
NUMBER-OF-SEQ NSEQ
D-SURFACE-SEQ NSEQ
CALC SEQ_77K = NSEQ
;
; Make the circular surface away from the PMTs. We assume perfect
; contact between the lucite guide and sapphire window. In reality
; there is a drop of stycast and probably vacuum. This could be
; fixed up.
D-GATE-TYPE DOWN-SEQUENCE-1
D-SURFACE-GATE 1
D-SURFACE-ROUGHNESS LUCITER
D-EXTERNAL-INDEX VACN
D-INTERNAL-INDEX LUCITEN
D-ATTENUATION-LEN LUCITEA
D-REALM OUTSIDE
CIRCULAR SEVENTY7K_RADIUS
;
; The edge of the 77K guide including an absorptive oring section.
D-GATE-TYPE NONE
D-REALM INSIDE
CYLINDER SEVENTY7K_RADIUS,SEVENTY7K_THICK
;
; Create the circular surface which is a gate into the
; splitter window.
D-GATE-TYPE TOPGATE
D-SURFACE-GATE 2
D-EXTERNAL-INDEX LUCITEN
D-SURFACE-DETAIL NONE
UCS 0,-SEVENTY7K_RADIUS,SEVENTY7K_THICK

```

```

PLANE-CORNER SEVENTY7K_RADIUS,2*SEVENTY7K_RADIUS
;
D-GATE-TYPE UP-SEQUENCE-2
D-SURFACE-GATE 3
UCS -SEVENTY7K_RADIUS,0,0
PLANE-CORNER SEVENTY7K_RADIUS,2*SEVENTY7K_RADIUS
UCS SEVENTY7K_RADIUS,SEVENTY7K_RADIUS,0
;
; +-----+
; | +X Part of the Splitter |
; +-----+
CALC NSEQ = NSEQ+1
NUMBER-OF-SEQ NSEQ
D-SURFACE-SEQ NSEQ
CALC SPLIT_PLUSX = NSEQ
;
D-EXTERNAL-INDEX LUCITEN
D-INTERNAL-INDEX LHEN
D-ATTENUATION-LEN LUCITEA
D-GATE-TYPE BOTGATE
D-SURFACE-GATE 1
D-REALM OUTSIDE
CIRCULAR SEVENTY7K_RADIUS
;
D-GATE-TYPE GATE
D-EXTERNAL-INDEX LHEN
D-INTERNAL-INDEX LUCITEN
D-SURFACE-GATE 2
D-REALM OUTSIDE
UCS 0,0,-EPS
CYLINDER SEVENTY7K_RADIUS,EPS
;
D-GATE-TYPE NONE
D-INTERNAL-INDEX VACN
D-EXTERNAL-INDEX LUCITEN
D-REALM OUTSIDE
CIRCULAR SPLIT_LONG
;
D-REALM INSIDE
D-EXTERNAL-INDEX VACN
D-INTERNAL-INDEX LUCITEN
D-SURFACE-DETAIL METAL
UCS 0,0,EPS
ROTATE Y SPLIT_ANGLE
CYLINDER SPLIT_RADIUS,SPLIT_THICK
;
D-SURFACE-DETAIL NONE
UCS 0,0,SPLIT_THICK
CYLINDER SPLIT_RADIUS,COUPLER_THICK
;

```

```

D-GATE-TYPE GATE
D-SURFACE-GATE 3
; D-EXTERNAL-INDEX GLASSN
UCS 0,0,COUPLER_THIN
CONSEC 0.0,COUPLER_RADIUS
;
D-EXTERNAL-INDEX LUCITEN
D-GATE-TYPE TOPGATE
D-SURFACE-GATE 4
UCS 0,0,-(SPLIT_THICK+COUPLER_THIN)
ROTATE Y -SPLIT_ANGLE-90
UCS -EPS,-SPLIT_RADIUS,0
PLANE-CORNER SPLIT_LONG+EPS,2*SPLIT_RADIUS
;
; +-----+
; | -X Part of the Splitter |
; +-----+
CALC NSEQ = NSEQ+1
NUMBER-OF-SEQ NSEQ
D-SURFACE-SEQ NSEQ
CALC SPLIT_MINUSX = NSEQ
;
D-GATE-TYPE BOTGATE
D-SURFACE-GATE 1
D-REALM OUTSIDE
PLANE-CORNER SPLIT_LONG+EPS,2*SPLIT_RADIUS
;
ROTATE Y 90
UCS 0,SPLIT_RADIUS,0
D-GATE-TYPE NONE
D-INTERNAL-INDEX VACN
D-REALM OUTSIDE
CIRCULAR SPLIT_LONG
;
D-INTERNAL-INDEX LUCITEN
D-EXTERNAL-INDEX LHEN
D-GATE-TYPE GATE
D-SURFACE-GATE 2
D-REALM OUTSIDE
CYLINDER SEVENTY7K_RADIUS,EPS
;
D-INTERNAL-INDEX LHEN
D-EXTERNAL-INDEX LUCITEN
UCS 0,0,EPS
D-GATE-TYPE DOWN-SEQUENCE-2
D-SURFACE-GATE 3
D-REALM OUTSIDE
CIRCULAR SEVENTY7K_RADIUS
;
D-INTERNAL-INDEX LUCITEN

```

```

D-EXTERNAL-INDEX VACN
D-GATE-TYPE NONE
D-SURFACE-DETAIL METAL
D-REALM INSIDE
ROTATE Y -SPLIT_ANGLE
CYLINDER SPLIT_RADIUS,SPLIT_THICK
;
D-SURFACE-DETAIL NONE
UCS 0,0,SPLIT_THICK
CYLINDER SPLIT_RADIUS,COUPLER_THICK
;
UCS 0,0,COUPLER_THIN
D-GATE-TYPE GATE
D-SURFACE-GATE 4
; D-EXTERNAL-INDEX GLASSN
CONSEC 0.0,COUPLER_RADIUS
;
; +-----+
; | Define Histograms |
; +-----+
; Define histograms for light entering
; the cell lightguide from the cell.
D-HISTOGRAM-SEQ SOURCE_SEQ
D-HISTOGRAM-GATE 2
D-NUMBER-OF-XBINS 50
D-NUMBER-OF-YBINS 50
D-MINIMUM-X -CELL_RADIUS
D-MAXIMUM-X CELL_RADIUS
D-MINIMUM-Y -CELL_RADIUS
D-MAXIMUM-Y CELL_RADIUS
BOOK X-HIT-POS,Y-HIT-POS,Position at Cell Light Guide
;
D-NUMBER-OF-XBINS 200
D-MINIMUM-X 0
D-MAXIMUM-X 20
BOOK TIME,,Time to Cell Light Guide (ns)
;
D-MAXIMUM-X 200
BOOK BOUNCES,,Number of bounces to Cell Light Guide
;
D-MAXIMUM-X 1.57
BOOK HIT-THETA,,Angle from normal (rad)
;
;Define Histograms for the end of the 77K guide
D-HISTOGRAM-SEQ SEQ_77K
D-HISTOGRAM-GATE 2
D-NUMBER-OF-XBINS 50
D-NUMBER-OF-YBINS 50
D-MINIMUM-X -SEVENTY7K_RADIUS
D-MAXIMUM-X SEVENTY7K_RADIUS

```

```

D-MINIMUM-Y -SEVENTY7K_RADIUS
D-MAXIMUM-Y SEVENTY7K_RADIUS
BOOK X-HIT-POS,Y-HIT-POS,Position at 77Kguide 2
;
D-NUMBER-OF-XBINS 200
D-MINIMUM-X 0
D-MAXIMUM-X 1.57
BOOK HIT-THETA,,Angle from normal guide2
;
D-HISTOGRAM-GATE 3
D-NUMBER-OF-XBINS 50
D-MINIMUM-X -SEVENTY7K_RADIUS
D-MAXIMUM-X SEVENTY7K_RADIUS
D-MINIMUM-Y -SEVENTY7K_RADIUS
D-MAXIMUM-Y SEVENTY7K_RADIUS
BOOK X-HIT-POS,Y-HIT-POS,Position at 77Kguide 3
;
D-NUMBER-OF-XBINS 200
D-MINIMUM-X 0
D-MAXIMUM-X 1.57
BOOK HIT-THETA,,Angle from normal 3
;
; Define histograms for PMT gate at +X
D-HISTOGRAM-SEQ SPLIT_PLUSX
D-HISTOGRAM-GATE 3
D-NUMBER-OF-XBINS 50
D-NUMBER-OF-YBINS 50
CALC MIDDLE = (SPLIT_THICK+COUPLER_THICK)*SIND(SPLIT_ANGLE)
CALC DELTA = SPLIT_RADIUS*COSD(SPLIT_ANGLE)
D-MINIMUM-X MIDDLE-DELTA
D-MAXIMUM-X MIDDLE+DELTA
D-MINIMUM-Y -SPLIT_RADIUS
D-MAXIMUM-Y SPLIT_RADIUS
BOOK X-HIT-POS,Y-HIT-POS,Position at PMT (+X)

D-NUMBER-OF-XBINS 200
D-MINIMUM-X 0
D-MAXIMUM-X 20
BOOK TIME,,Time to PMT (ns) (+X)
;
D-MAXIMUM-X 200
BOOK BOUNCES,,Number of bounces to PMT (+X)
;
D-MAXIMUM-X 1.57
BOOK HIT-THETA,,Angle from normal (rad) (+X)
;
; Define histograms for PMT gate at -X
D-HISTOGRAM-SEQ SPLIT_MINUSX
D-HISTOGRAM-GATE 4
D-NUMBER-OF-XBINS 50

```

```

D-NUMBER-OF-YBINS 50
CALC MIDDLE = -(SPLIT_THICK+COUPLER_THICK)*SIND(SPLIT_ANGLE)
CALC DELTA = SPLIT_RADIUS*COSD(SPLIT_ANGLE)
D-MINIMUM-X MIDDLE-DELTA
D-MAXIMUM-X MIDDLE+DELTA
D-MINIMUM-Y -SPLIT_RADIUS
D-MAXIMUM-Y SPLIT_RADIUS
BOOK X-HIT-POS,Y-HIT-POS,Position at PMT (-X)

D-NUMBER-OF-XBINS 200
D-MINIMUM-X 0
D-MAXIMUM-X 20
BOOK TIME,,Time to PMT (ns) (-X)
;
D-MAXIMUM-X 200
BOOK BOUNCES,,Number of bounces to PMT (-X)
;
D-MAXIMUM-X 1.57
BOOK HIT-THETA,,Angle from normal (degrees) (-X)
;
; +-----+
; | Source and other information |
; +-----+
SOURCE-SEQUENCE SOURCE_SEQ
START-POSITION 0,0,ZPOS
MINIMUM-THETA 0
MAXIMUM-THETA 180
RANDOM-SEED 295002484
PHOTONS-PER-SOURCE 1000000
; With the following definition, distance units are cm
SPEED-OF-LIGHT 2.99792458E10
MAXIMUM-BOUNCES 5000
DIAGNOSTIC-TRACKING NO
OUTPUT-FILE \0.in
EXIT

```